Engineered carbon nanomaterials by light-matter interaction

by

Pingping Chen

B.S., Minzu University, 2011
M.S., University of Chinese Academy of Sciences, 2015

AN ABSTRACT OF A DISSERTATION

submitted in partial fulfillment of the requirements for the degree

DOCTOR OF PHILOSOPHY

Department of Industrial and Manufacturing System Engineering
Carl R. Ice College of Engineering

KANSAS STATE UNIVERSITY
Manhattan, Kansas

2023

Abstract

Synthesis of unique nanomaterials and advancement of their transformative properties play key roles to meet the application in future nanoelectronics, nanophotonics, plasmonics, and reconfigurable electronics. Graphene, the first two-dimensional and atomically thin film arranged in hexagonal honeycomb lattice of carbon atoms, exhibits excellent electronic, photonic, mechanical, and thermal properties, and was early predicted to be an excellent candidate to replace traditional semiconductor, i.e., silicon. However, with the realization of its zero-energy bandgap, it spurred further research to open a band gap in graphene. The fabrication of graphene nanoribbons with narrow physical width of ribbons appeared to be a promising approach to achieve the above goal. However, fabricating ultrathin (sub-20 nanometer) graphene nanoribbons (GNRs) is extremely challenging even with the help of a state-of-the art electron beam lithography facility. In contrast, the growth and development of ultranarrow carbon nanotubes (CNTs) (diameter ~ few nanometers to 1.5 nm) are an established technology that may suitably be leveraged to innovate the synthesis of GNRs, and possibly new carbon nanomaterials. The research in this dissertation work seeks to study CNT characteristics and provides an approach to create and fundamentally understand GNR synthesis. By employing an ultrafast laser irradiation to CNTs to alter the shape and transform the metallic electronic phase of CNTs to semiconducting/semi-insulating phases of GNRs and hybrid GNR/nanocrystals, an important milestone for future electronics and photonics is demonstrated.

An ultrafast laser-based approach is developed to explore experimental light-matter interaction conditions to fabricate GNRs from multi-walled carbon nanotubes (MWCNTs). By using a high-intensity electromagnetic field to interact with the CNTs, this study successfully demonstrates the nanomachining of carbon nanotubes and their transformation to graphene

nanoribbons and carbon nanocrystal hybrids. The ribbons are narrow (typically, less than 15 or 20 nm in width but could be further scaled down by choosing tubes of smaller diameters), while the nanocrystals showing well-defined crystalline structures are embedded along the length of the ribbons with ~ 15 nm to down to ~ 3 nm in size. It is found that the transformation from the MWCNTs to GNRs is more sensitive to the overall laser intensity and less sensitive to laser spot sizes and radiation time. To understand the transformation from MWCNTs to GNRs, a thermal response of MWCNTs under exposure to intense femtosecond pulses is investigated, by developing a heat-transfer Multiphysics model based on the finite element analysis method. Further experiments are achieved in this work to obtain sub-10 nanometer ribbons that are promising for future applications.

One big challenge to exploit the extraordinary properties of GNRs in nanophotonics and nanoelectronics is to fabricate aligned GNR arrays. Compared to a single GNR, GNR arrays have higher response signal intensity (current or light intensity) and hence better performance. This work proposes a mechanism to fabricate aligned GNR arrays by first aligning CNTs. By combining an inkjet printing technique and the dielectrophoretic technique a proof-of-concept of fabrication of CNT arrays are demonstrated. Furthermore, the inkjet printing method is a fast, controllable, and low-cost method. Electrodes are designed and printed for dielectrophoretic (DEP) to achieve individual carbon nanotube alignment. This DEP alignment approach also has the advantage of eliminating chemicals from the patterned structures and the flexibility in adoption, compared to other expensive methods that involve lithographic processes.

The concluding part of the study is to investigate the optical responses, specifically the plasmonic properties of individual and aligned GNRs, especially aiming to manipulate the optical responses of GNRs to the near-infrared wavelength range. A Multiphysics model is developed to

study the plasmonic properties of the individual and GNR arrays based on the finite element analysis method. It is found that when the width of GNR becomes smaller, the surface plasmon resonant wavelength can be tuned from the mid-infrared (9 μm) to the near-infrared (2.5 μm) range. Further research can be pursued, including experimental fabrication and demonstration of these devices, by doping the GNRs to increase the Fermi energy of the electrons and thereby tuning the resonant wavelength to the visible light range.

Engineered carbon nanomaterials by light-matter interaction

by

Pingping Chen

B.S., Minzu University, 2011
M.S., University of Chinese Academy of Sciences, 2015

A DISSERTATION

submitted in partial fulfillment of the requirements for the degree

DOCTOR OF PHILOSOPHY

Department of Industrial and Manufacturing System Engineering
Carl R. Ice College of Engineering

KANSAS STATE UNIVERSITY
Manhattan, Kansas

2023

Approved by:

Co-Major Professor
Suprem Das

Approved by:

Co-Major Professor
Shuting Lei

Copyright

Abstract

Synthesis of unique nanomaterials and advancement of their transformative properties play key roles to meet the application in future nanoelectronics, nanophotonics, plasmonics, and reconfigurable electronics. Graphene, the first two-dimensional and atomically thin film arranged in hexagonal honeycomb lattice of carbon atoms, exhibits excellent electronic, photonic, mechanical, and thermal properties, and was early predicted to be an excellent candidate to replace traditional semiconductor, i.e., silicon. However, with the realization of its zero-energy bandgap, it spurred further research to open a band gap in graphene. The fabrication of graphene nanoribbons with narrow physical width of ribbons appeared to be a promising approach to achieve the above goal. However, fabricating ultrathin (sub-20 nanometer) graphene nanoribbons (GNRs) is extremely challenging even with the help of a state-of-the art electron beam lithography facility. In contrast, the growth and development of ultranarrow carbon nanotubes (CNTs) (diameter ~ few nanometers to 1.5 nm) are an established technology that may suitably be leveraged to innovate the synthesis of GNRs, and possibly new carbon nanomaterials. The research in this dissertation work seeks to study CNT characteristics and provides an approach to create and fundamentally understand GNR synthesis. By employing an ultrafast laser irradiation to CNTs to alter the shape and transform the metallic electronic phase of CNTs to semiconducting/semi-insulating phases of GNRs and hybrid GNR/nanocrystals, an important milestone for future electronics and photonics is demonstrated.

An ultrafast laser-based approach is developed to explore experimental light-matter interaction conditions to fabricate GNRs from multi-walled carbon nanotubes (MWCNTs). By using a high-intensity electromagnetic field to interact with the CNTs, this study successfully demonstrates the nanomachining of carbon nanotubes and their transformation to graphene

nanoribbons and carbon nanocrystal hybrids. The ribbons are narrow (typically, less than 15 or 20 nm in width but could be further scaled down by choosing tubes of smaller diameters), while the nanocrystals showing well-defined crystalline structures are embedded along the length of the ribbons with ~ 15 nm to down to ~ 3 nm in size. It is found that the transformation from the MWCNTs to GNRs is more sensitive to the overall laser intensity and less sensitive to laser spot sizes and radiation time. To understand the transformation from MWCNTs to GNRs, a thermal response of MWCNTs under exposure to intense femtosecond pulses is investigated, by developing a heat-transfer Multiphysics model based on the finite element analysis method. Further experiments are achieved in this work to obtain sub-10 nanometer ribbons that are promising for future applications.

One big challenge to exploit the extraordinary properties of GNRs in nanophotonics and nanoelectronics is to fabricate aligned GNR arrays. Compared to a single GNR, GNR arrays have higher response signal intensity (current or light intensity) and hence better performance. This work proposes a mechanism to fabricate aligned GNR arrays by first aligning CNTs. By combining an inkjet printing technique and the dielectrophoretic technique a proof-of-concept of fabrication of CNT arrays are demonstrated. Furthermore, the inkjet printing method is a fast, controllable, and low-cost method. Electrodes are designed and printed for dielectrophoretic (DEP) to achieve individual carbon nanotube alignment. This DEP alignment approach also has the advantage of eliminating chemicals from the patterned structures and the flexibility in adoption, compared to other expensive methods that involve lithographic processes.

The concluding part of the study is to investigate the optical responses, specifically the plasmonic properties of individual and aligned GNRs, especially aiming to manipulate the optical responses of GNRs to the near-infrared wavelength range. A Multiphysics model is developed to

study the plasmonic properties of the individual and GNR arrays based on the finite element analysis method. It is found that when the width of GNR becomes smaller, the surface plasmon resonant wavelength can be tuned from the mid-infrared (9 μm) to the near-infrared (2.5 μm) range. Further research can be pursued, including experimental fabrication and demonstration of these devices, by doping the GNRs to increase the Fermi energy of the electrons and thereby tuning the resonant wavelength to the visible light range.

Table of Contents

List of Figures

List of Tables

Table of Abbreviations

- GNR: graphene nanoribbon
- AGNR: armchair graphene nanoribbon
- ZGNR: zig-zag graphene nanoribbon
- CNT: carbon nanotube
- MWCNT: multi-walled carbon nanotube
- SWCNT: single-walled carbon nanotube
- DWCNT: double-walled carbon nanotube
- DMF: N-dimethylformamide
- CVD: chemical vapor deposition
- AFM: atomic force microscopy
- SEM: scanning electron microscopy
- STM: scanning tunneling microscopy
- TEM: transmission electronic microscopy
- HRTEM: high-resolution transmission electron microscopy
- EDX: energy-dispersive X-ray spectroscopy
- TERs: tip-enhanced Raman spectroscopy (TERs).
- XPS: X-ray photoelectron spectroscopy (XPS)
- SPM: scanning probe microscopy
- BSE: backscattered electrons
- SE: secondary electrons
- RGB: radical breathing mode
- UFLs: ultrafast lasers
- FWHM: full width at half maximum
- VHs: van Hove singularities (VHs)
- DOS: density of states
- LINM (laser induced nanomachining)
- DEP: dielectrophoresis

Acknowledgments

"LIFE IS A TRAGEDY WHEN SEEN CLOSE-UP, BUT A COMEDY IN LONG-SHORT."

–BY CHARLIE CHAPLIN

Pursuing my Ph.D. has been a journey throughout which I have learned to smile and keep smiling at failures. At the end of the day, I found out I still have the enthusiasm to pursue knowledge, and I consider this as a considerable success, out of the degree. My deepest gratitude to all those who have supported, encouraged, occasionally cajoled, and stood by me.

To my daughter, who always believes in me, has been my biggest fan, and pushed me to reach my fullest potential not just as a scientist but also as a person.

To Tom Harris, who lifts me at the end of this journey and gives me hope for new life.

To my advisor, Suprem Das, for showing me what I need to have to be a better scientist. To my advisor, Shuting Lei, for all the discussions and encouragement.

To Xinya Wang, Aroop Behera, Wenjun Xiang, Thiba Nagaraja, and Anand Gaur, my lab partners and more importantly friends. You have made graduate school not just endurable but enjoyable.

To Cosmin Blaga and members of his group, Eric Mullins and Sajed Hosseini-Zavareh, I always enjoyed working alongside you and learning from you.

To Covid-19 and HITs laser, for it made this journey more tragic and funnier than it was supposed to be.

I also thank Brice LaCroix and Shih-Kang Fan, for their support and kind collaboration in providing their Raman spectroscopy and Dielectrophoresis lab facilities, respectively, available to me. To Takashi Ito, for letting me use his instruments for free and trusting me.

Finally, to all the members of the Ph.D. committee: Shuting Lei, Cosmin Blaga, Shing Chang, and Dong Lin. You all are my teachers and mentors.

Dedication

I dedicate this thesis to my daughter and God. They are the sources of my strengths to keep my head above water, they are the lights leading me through this endless tunnel of darkness.

Chapter 1 - Introduction

1.1 Background

On December 29, 1959, Physics Nobel Prize laureate Richard Feynman presented a lecture titled “There’s Plenty of Room at the Bottom” in which he introduced the concept of nanotechnology (Feynman, 1959). Since then, nanotechnology has been a topic of high interest although experimental efforts started later in the 1980’s. By now, scientists have developed numerous experimental methods for the synthesis of nanostructures. In 1965, Gordon Moore, the co-founder of leading chip manufacturer, Intel Inc., published an article in Electronics Magazine in which he stated that the number of transistors on an affordable CPU would double approximately every 18 months (Moore, 1965). This became known as the famous ‘Moore’s Law’. A few years later, the first microprocessor “Intel 4004” was born in Intel in 1971; the chip was 12 square millimeters, had 2300 transistors, and had a technology node with a 10-μm lithography feature (Faggin et al., 1974,715). Moore’s Law then predicted the rate of technological advancements in the field of solid-state devices for the following 50 years. In 2018, when Intel turned 50 years old, Moore’s Law began to fail; delaying its 10 nm chip release date by one year, and subsequently changing its continued chip update making period to three years as opposed to two. In 2022, Bob Colwell, Intel’s former chief architect, claimed that Moore’s law was obsolete claiming the 5 nm chip didn’t hold many advantages over a 7 nm chip. This not only indicates the extreme difficulty in obtaining further downscaling of materials and their precision control but the need for new science for future technological developments.

One of the potential pathways to achieve breakthroughs beyond Moore’s Law is to develop novel nanomaterials that transcend the limits of silicon electronics. When graphene was first isolated from graphite via micromechanical exfoliation using magic tape/scotch tape (Novoselov

et al., 2004), their method was believed to provide potential to replace silicon in computer chips. However, it soon became evident that graphene is not an ideal building block for transistors due to the lack of a bandgap (Kostya S. Novoselov et al., 2005). Since then there has been numerous attempts to identify methods of opening sizable bandgap in graphene, such as (1) adding hydrogen to graphene's carbon atoms to change their hybridization from sp^2 into sp^3 (Elias et al., 2009); (2) physically patterning graphene to form ribbon-like structure, that is, graphene nanoribbons (GNRs) (Nakada et al., 1996).; (3) doping graphene with elements and functional groups, etc. (Oostinga et al., 2008). Hydrogen can help remove the conducting π band and open an energy gap; however, the hydrogen atoms cannot be controlled easily in graphene lattice, making it difficult to create a bandgap. Doping graphene nanoribbons (GNRs) have been shown to effectively tune electronic properties and can achieve bandgaps from 0.1 eV to 3 eV. Electrostatically, applying top and bottom gate voltages on a bilayer graphene has been shown to break the inversion symmetry of the two layers of graphene and thus lead to the opening of a tunable band gap between valence and conduction bands (Oostinga et al., 2008). However, with this approach, only a small bandgap of 250 meV can be achieved even when the applied voltage is 100 V, a high gate voltage value that limits the device applications (Zhang et al., 2009). Therefore, the strategy to breakdown 2D symmetry of graphene to turn it 1D to create a narrow strip of graphene is believed to be an effective strategy to create GNRs to harness bandgap in 2D graphene. Breaking the symmetry of graphene, soon realized, create the new boundary conditions that opens up a bandgap (Nakada et al., 1996).

GNRs are quasi-one-dimensional (between the 1D structure of carbon nanotubes and the 2D structure of graphene) graphene strips with a parallel armchair or zigzag edges on both sides and widths less than 50 nm (Nakada et al., 1996; Wakabayashi et al., 1999). The first theoretical

study of GNR, performed in 1996, before the peeling of graphene, investigated the spatial confinement using a tight binding model. Soon after the exfoliation of graphene, GNRs gained significant interest both theoretically and experimentally. GNRs were shown to preserve the superior electronic and magnetic properties of graphene (Rafiee et al., 2010; Zhang et al., 2005). Furthermore, unlike large-area graphene sheets which have zero bandgap and are semi-metallic (Kostya S Novoselov et al., 2005; Rousse et al., 2001), GNRs with widths less than 20 nm display a finite and tunable bandgap ((Son et al., 2006); (Han et al., 2007) as well as high mobility, making them a potential alternative candidate to silicon in the manufacturing of semiconductor devices (Liang et al., 2007). Furthermore, since GNRs have a large surface area with edge states they provide a platform for accessible sites for various functionalization and catalysis (Zhu et al., 2016); as such, GNR-based nanomaterials are suitable for applications in the electrochemical sensing and biosensing (Zhang et al., 2005) (Govindasamy et al., 2017). Many challenges exist regarding the potential applications of GNRs in nanotechnology and even more recent emerging areas like quantum technology, including scalable production, atomic-scale precision, high-throughput characterization, and device integration.

1.2 Motivation and Goal of the Research in this Dissertation

Various approaches have been developed for GNR synthesis, including top-down lithographic approaches (by patterning and selectively etching graphene), bottom-up methods (utilizing restructured sites, molecular precursor method), and unzipping carbon nanotubes. While all these techniques can be used to produce nanoribbons, they risk exposing the entire sample, including the support materials (such as silicon and oxide that are often used for making an electronic device) to a reactive and/or corrosive environment. Laser-based unzipping of nanotubes along their longitudinal direction to form GNRs was reported (Kosynkin et al., 2009), but the study

is preliminary and lacks clarity, making it hard to control (Han et al., 2019; Kumar et al., 2011). Therefore, a systematic mechanism to understand the process is needed.

Still today achieving large-scale production of narrow GNRs has been a primary challenge for more than a decade. The fabrication of GNRs with sub-20 and sub-10 nanometer width is a promising approach to overcome the barrier caused by current approach of making GNRs and thus paving the path to "more Moore" direction. The goal of this research is to understand the interaction between a laser-induced ultrafast electromagnetic field and carbon nanotubes to study new low-dimensional nanomaterials (one-dimensional and hybrid one/zero-dimensional) and evaluate their relevance to nanotechnology by developing approaches to create aligned GNR arrays, thus enabling novel optical and electronic devices. Aligned CNTs and GNRs could further provide a platform to explore tube-to-tube and ribbon-to-ribbon interactions. They are also ideal candidates to develop devices with high response signals in practical electronic and photonic devices. Well-aligned CNT structures offer improved electron mobility, strain sensitivity, reproducibility, and mechanical properties. Similarly, applications based on GNRs depend on the orientation of the ribbons, such as transistors and on-chip connectors. Another important application is to modify the optical resonance of graphene plasmonics. Therefore, aligning CNTs is a prerequisite for achieving controlled and aligned GNRs and GNR electronics, photonics and plasmonics.

Various techniques have been developed to create aligned graphene ribbons, such as patterning CVD-grown monolayer graphene films using electron-beam lithography (EBL) and reactive ion etching (RIE) (Klimenko et al., 2021) as well as polymer-protected plasma etching CNT arrays (Jiao et al., 2010). However, these methods are either expensive or utilize chemicals, which largely limits the applications of the obtained graphene ribbons. Traditional lithographic

techniques are also challenging to produce sub-20 nanometer wide GNRs. These limitations necessitate an alternative manufacturing technique for creating aligned graphene ribbons with high yield, flexible to adopt, capable of operating at room temperature, low-cost, and high controllability. The fabrication approach developed in this work meets these requirements; in addition, the manufacturing process could be used to control the width, the layer numbers and potentially the edge states of the GNRs. These advantages make the application of the technique to other nanomaterials attractive to accelerate the field of nanotechnology. The primary advantages of the CNT and GNR alignment technique developed in this work is further accelerated by combining 2D inkjet printing and the dielectrophoretic methods that are low cost and highly suitable for scale-up and automation; thereby having potential to be adopted by industry for large scale production.

The main objective of this research is to fundamentally understand light-matter interactions and electric field-nanotube interactions to co-develop a promising and effective way to create GNRs and GNR arrays in a chip/wafer scale and overcome the current barrier in lithographic and chemical methods in producing GNRs. Specifically, this is accomplished by utilizing a dielectrophoretic method of aligning the CNTs and employing subsequently a laser-induced ultrafast electromagnetic field to tailor carbon nanotubes to study new low-dimensional nanomaterials (one-dimensional and hybrid one/zero-dimensional) and evaluates their relevance to nanotechnology applications. The specific goals of this research include the following:

1.2.1 CNT growth principles and single nanotube characterization at nanoscale- Since the GNRs are synthesized from the CNTs, study of CNTs is important. As such, the relevance between physical properties of individual multi-walled CNTs and growth temperature will be investigated.

This will involve the characterization of CNTs via tip-enhanced-Raman spectroscopy combined with atomic force microscopy.

1.2.2 An experimental approach to setup and understand the conditions to study light-matter interactions and its effect to fabricate GNRs using multi-walled CNTs will be developed. This will involve developing a comprehensive heat transfer model of light-matter interaction based on the finite element analysis method. Various processes such as the thermal response under exposure to intense, femtosecond pulses are discussed in this chapter.

1.2.3 An alternative approach to achieve aligned GNR arrays by first developing techniques to align CNTs will be presented. This approach will eliminate chemicals from patterned structures with a flexible design that can be easily adopted.

1.2.4 Understanding GNR physical parameters on their light-field manipulation: Different approaches to manipulate GNRs' optical responses to push the resonances to the near-infrared wavelength range will be explored. A model to simulate the plasmonic properties of individual GNRs and GNR arrays will be developed and presented.

1.3 The rest of dissertation is organized as follows:

Chapter 2 provides an overview of the fundamental knowledge of carbon CNTs and GNRs, including their growth/synthesis, structure and properties, and applications. After introducing various GNR synthesis methods, the unzipping CNT method of fabricating GNRs is discussed in detail.

Chapter 3 introduces various analytical techniques for characterizing the morphology and nanoscale structure of CNTs and GNRs. After providing an overview of the working principles of each characterization method, their limitations are discussed. In the last section of the chapter, an investigation of the relevance between the properties of individual MCNTs and their nucleation

temperatures during the growth is presented, as characterized by a tip-enhanced Raman spectroscopy (TERS) technique.

In Chapter 4, an overview of the processes and mechanisms of an ultrafast laser interaction with a solid is presented, followed by experimental details of the ultrafast laser unzipping method to engineer CNTs into GNRs. This is supported by a structural characterization of the ribbons with the aid of atomic force microscopy, electron microscopy, Raman spectroscopy, and SNOM based infrared imaging respectively. In addition to this experiment, a detailed finite element model to simulate the heat transfer to the CNTs by the ultrafast laser is presented.

In Chapter 5, applications-orientated research of GNRs and GNR arrays is presented. To develop better-performance nanodevices based on GNRs, two elements are essential: alignment of GNRs and signal enhancement. In the first part of this chapter, the fabrication of GNR arrays by aligning CNTs is explained, and details of our experimental method to align carbon nanotubes are presented. The second part of the chapter focuses on the simulation of GNR array for plasmonics, with specific emphasis on identifying the parameters of GNRs that will produce optical responses in the visible light wavelength range.

Finally, Chapter 6 provides a summary of the results and recommendations for future work.

Chapter 2 - Overview of Carbon Nanotubes and Graphene Nanoribbons

This chapter provides an overview of CNTs (Carbon Nanotubes) and GNRs (Graphene Nanoribbons). The chapter begins by briefly reviewing the basic structure and notation used to describe single-wall carbon nanotubes (SWCNTs) and multi-wall carbon nanotubes (MWCNTs) (in Section 2.1), followed by a description of the unique electronic structures and properties of carbon nanotubes (in Section 2.2). With this background, the synthesis methods of CNTs and GNRs are reviewed (in Section 2.3). Finally, Section 2.4 reviews the synthesis of GNRs.

2.1 Overview of CNTs and GNRs

Graphene, the latest allotrope of carbon nanomaterial and an atomically thin sheet of carbon atoms with a thickness of a single atom, approximately 0.35 nm, with a two-dimensional honeycomb lattice structure is considered as the building block of wide variety of carbon nanomaterials, such as one-dimensional CNTs, one-dimensional GNRs, and zero-dimensional fullerene (bucky ball). The structural relationships between these carbon nanomaterials are summarized in Figure 2.1. The one-dimensional structure, i.e., CNTs, are obtained by rolling a single layer, several layers, or dozens of layers of two-dimensional graphene. As such, the carbon atoms in CNTs are sp^2 hybridized. The hexagonal grid structure has a certain degree of bending, forming a spatial topology structure. CNTs were first reported in 1991 by Sumio Iijima, as shown in Figure 2.3 (a). Since the diameter is of the order of nanometers and the length can be hundreds of microns, the axial (longitudinal) dimension is much larger than the lateral dimension; therefore, carbon nanotubes are treated as one-dimensional carbon nanomaterials.

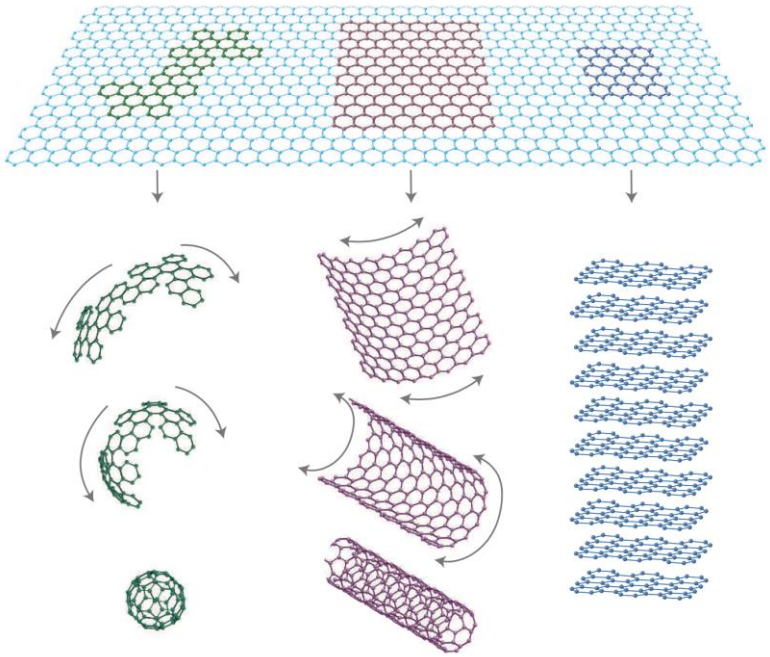

Figure 2.1. Illustration of the relations between graphene and other carbon nanomaterials (Geim & Novoselov, 2007).

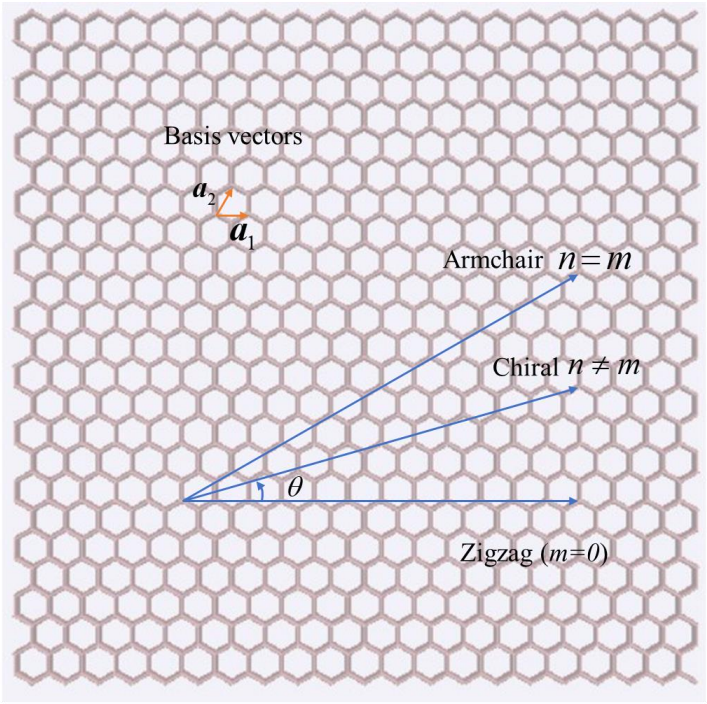

Figure 2.2. Classification of single-walled CNTs by their chiral indices (n, m), and chiral angle (θ).

Compared with the size of the most advanced silicon-based semiconductor devices obtained to date, the nanotube diameter is still much smaller. In addition to the small size of CNTs, their electronic properties, photonic properties, chemical properties, mechanical properties, and thermal properties have a significant impact on a wide variety of technologies. Due to the number of possible helical geometries, CNTs provide a family of structures with different diameters and chirality. Figure 2.3 (b) shows different chirality for CNTs: (1) armchair, (2) zigzag, and (3) chiral conformations.

The chiral factor of CNTs is represented by $C_{\mathrm{h}} = na_1 + ma_2 \equiv (n, m)$, where a_1 and a_2 are basis vectors, and n and m are chiral index numbers, as shown in Figure 2.2. The chiral indices (n, m) define the chiral vectors (blue arrows) that connect two equivalent carbon atoms in a graphene plane. If (n, m) satisfies 2n + m = 3q, where q is an integer, then the CNT is metallic. For semiconducting CNTs, (n, m) meets the relation of n – m = 3q, and n ≠ m, q is an integer. All armchair (n, n) CNTs are metallic. Whereas zigzag CNTs (n, 0) are either semiconductors or metallic. The chiral angle (θ) is defined as the angle between the zigzag direction and circumference (θ = 0°~30°). Achiral nanotubes, in which θ = 0 and 30°, are referred to as zigzag and armchair nanotubes, respectively.

Finite termination of graphene resulting in quasi-one-dimensional (which is between the 1D structure of carbon nanotubes and 2D structure of graphene) ribbon-like structures, are known as graphene nanoribbons (GNRs). GNRs are quasi-one-dimensional graphene strips with two different possible edge geometries, namely zigzag and armchair, with widths less than 50 nm (Nakada et al., 1996); (Wakabayashi et al., 1999). The two geometries, termed as armchair graphene nanoribbons (AGNRs) and zigzag graphene nanoribbons (ZGNRs), are shown in Figure

2.3 (c) and (d), respectively, and have different electronic properties arising from their contrasting boundary conditions.

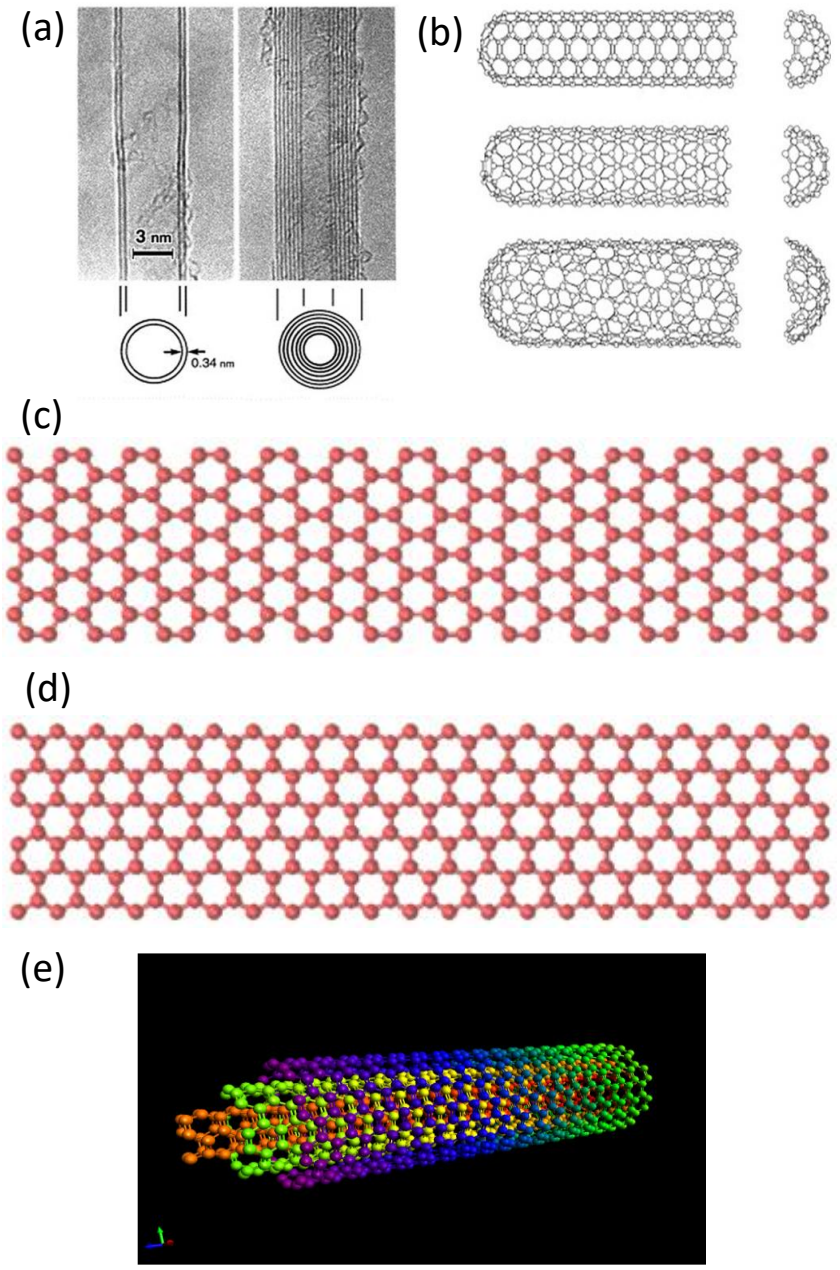

Figure 2.3. (a) CNTs were first discovered in 1991 (Iijima, 2002); (b) schematic representation of CNTs in different chiralities: (upper) armchair, (middle) zigzag, and (lower) chiral conformations (Ma et al., 2010); (c) and (d) schematic representation of armchair and zigzag GNRs, respectively; (e) schematic representation of a multiwalled CNT (designed by the author).

Note that the atoms along a zigzag edge are from the same sublattice, whereas the atoms from two different sublattices create bonds along the armchair edges. Depending on chirality and width of the ribbons, the properties of the GNRs can be very different. For AGNRs, we use the width Na to represent the number of carbon dimers in the transverse direction of the nanoribbon. For ZGNRs, the width Nz is used to represent the number of zigzag-shaped carbon chains in the transverse direction.

2.2 Properties of CNTs and GNRs

As one-dimensional nanomaterials, CNTs have a very high aspect ratio. Their lightweight and small thickness result in a high specific surface area. This special structure of CNTs provides high electrical, mechanical, and chemical properties. The electrical properties of CNTs can vary based on many factors, including the degree of crystallinity, radius size, degree of defects, and chirality coefficient. One of the most significant physical properties of CNTs and GNRs is their electronic structure that depends only on their geometry and is unique to solid-state physics. Specifically, for single-wall CNTs without doping, their electronic structure will be either metallic or semiconducting, depending on their diameter and chirality. Before GNRs were discovered, Nakada et al. calculated their electronic structure at two boundaries using simple tight-binding calculations. AGNRs are found to behave as a metallic when $Na = 3p + 2$ (p is an integer), and in other cases, the nanoribbons will open a certain energy gap (Nakada et al., 1996). For nanoribbons with band gaps, the band gap energy decreases with increasing nanoribbon width with the energy gap approaching zero as the width becomes large (~ several hundred nanometers). ZGNRs at the zigzag boundary are all metallic with the bottom of the conduction band and the top of the valence band overlapping at $k = \pi$. When the nanoribbons are wider ($Nz = 30$), in the range of $2\pi/3 < |k| <$

π near the Fermi surface, a flat band appears, and the corresponding wave function is localized on the zigzag boundary (Nakada et al., 1996).

2.2.1 Electronic properties

As previously shown, CNTs are defined by their chiral indices (n, m) constructed from graphene sheets, and GNRs can be represented by Na and Nz for AGNRs and ZGNRs, respectively. Thus, a natural approach is to begin by describing the band structure of graphene to understand the electronic structure of CNTs and GNRs. Like graphene, CNTs and GNRs are characterized by two types of bonds, arranged in the well-known sp^2 planar hybridization. The carbon atom possesses four valence orbitals: 2s, $2p_x$, $2p_y$, and $2p_z$, and the z-axis is defined as perpendicular to the graphene sheet. In-plane covalent bounds σ (bonding) and σ* (anti-bonding) are formed by orbitals (s, p_x, p_y) which determine the binding energy and elastic properties of graphene. Out-of-plane orbitals p_z orbitals of the carbon atoms interact with each other and create delocalized π (bonding) and π* (anti-bonding) orbitals. In CNTs, these π states are influenced by the curvature of the tube which impacts the band structure. They are also responsible for the weak interaction between nanotubes in a bundle as well as the interaction with substrates. Since CNTs are one-dimensional systems, their density of states associated with each energy band varies as $\sqrt{E}$ and presents characteristic diverging values called Van-Hove singularities. Depending on whether the K-lines cross exactly the Dirac point of graphene, the nanotube can be metallic or semiconducting.

Based on the theoretical work discussed above, researchers successfully exfoliated graphene, which led to subsequent theoretical work on GNRs. Son et al. performed first-principle calculations using a local (spin) density approximation on two nanoribbon boundaries and showed that both AGNRs and ZGNRs would open an energy gap with semiconducting properties, in

contrast with the results of the tight-binding model (Son et al., 2006). According to their results, AGNRs are categorized into three families: Na = 3p (medium band gap), 3p + 1 (large band gap), and 3p + 2 (small band gap), where p is an integer. In each family of AGNRs, the size of the band gap decreases monotonically with increasing nanoribbon width. Furthermore, the appearance of band gaps in AGNRs originates from the quantum confinement effects and edge effects of nanoribbons. Similarly, the band structures of ZGNRs are direct band gaps, and the band gap decreases with increasing nanoribbon width. Their results show that the flat band at E_F will produce a large density of states near the Fermi level. When the effect of spin degrees of freedom is considered in the local density approximation, small site repulsion causes the ZGNRs to magnetize, leading the nanoribbons to exhibit ferromagnetic ordering of spins on the same side of the zigzag boundary. The opposite sides of the nanoribbons exhibit antiferromagnetic coupling. The opposite spin states of the nanoribbons are in different sublattices, and these magnetic orders cause a certain energy dislocation of the sublattice potential, resulting in a nanoribbon band gap (Son et al., 2006). Figure 2.4 shows band structures and density of states of CNTs and GNRs with a similar number of carbon atoms, calculated using the tight-binding method (Kan, 2013). The wave vector $\boldsymbol{k}$ is along the length direction and the density of states is plotted along the horizontal direction. $\boldsymbol{k}$ is in the first Brillouin zone in all the plots. From Figure 2.4 (a) - (d), we can see that both the armchair and zigzag CNT with N = 6 are metallic. Armchair CNTs and zigzag CNTs are metallic when n = 3m, and m is an integer. GNRs have similar electronic properties to CNTs because a zigzag and armchair GNR can be produced by unzipping an armchair and a zigzag CNT, respectively. In addition, ZGNRs are metallic, like armchair CNTs. From Figure 2.4. (i) we can see that AGNRs are similar to zigzag CNTs and can be divided into three families: Na = 3p (medium band gap), 3p + 1 (large band gap), and 3p + 2 (small band gap). Additionally, the band gap of AGNRs decreases monotonically as the number of carbon atoms increases.

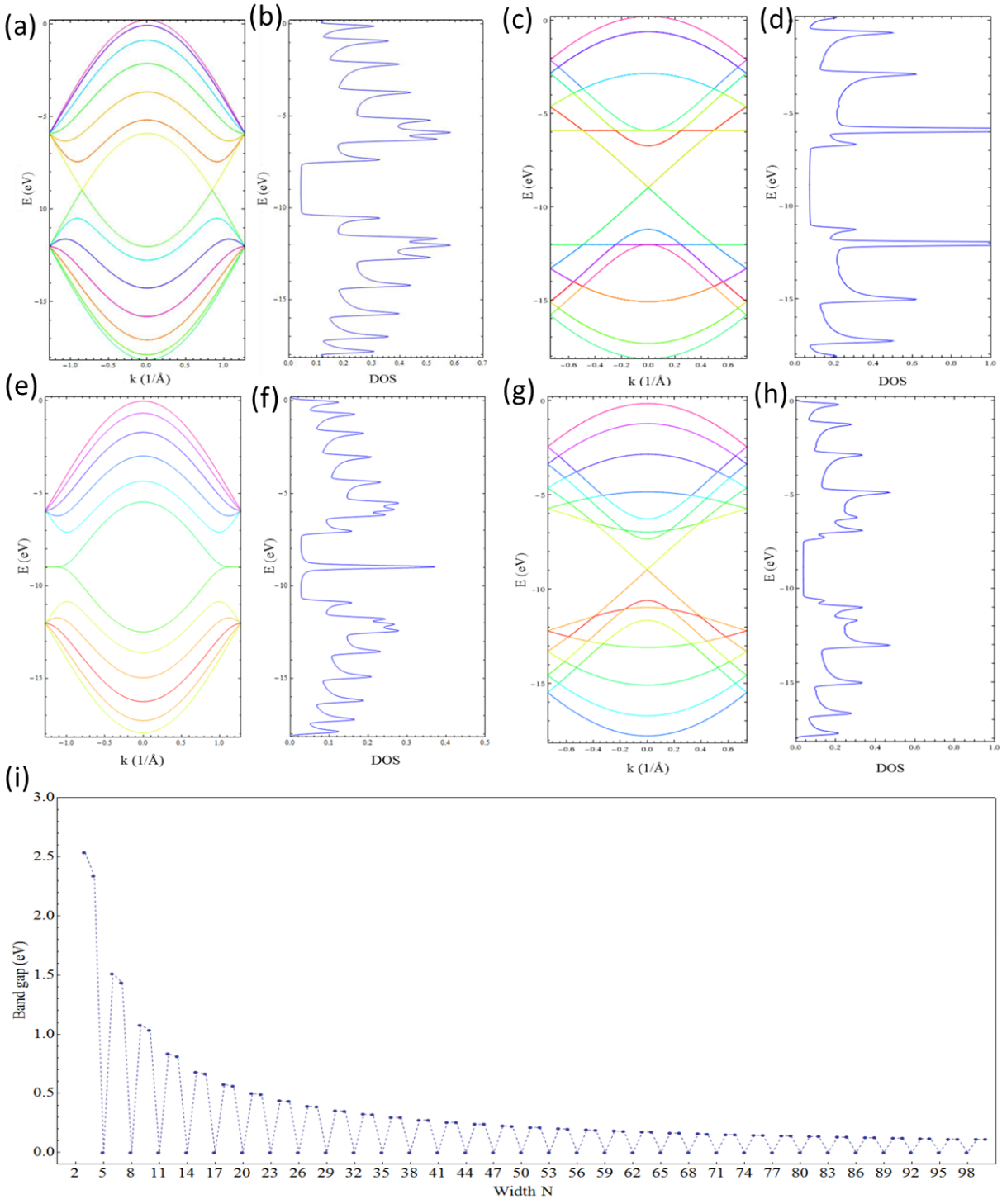

Figure 2.4. (a) Armchair CNT (6, 6) band structure and (b) DOS; (c) Zigzag CNT (6, 0) band structure and (d) DOS; (e) ZGNR N = 6 band structure and (f) DOS; (g) AGNR N = 8 band structure and (h) DOS; (i) AGNR band gap versus width N (Kan, 2013).

2.2.2 Optical properties

Some of the optical properties of materials of interest include optical absorption, photoluminescence, and scattering. This section focuses on optical absorption properties. Furthermore, the optical properties are closely related to the electronic band structures of materials; as such, CNTs and GNRs as they can absorb photons' energy ranging from terahertz to visible (Balarastaghi et al., 2016). For GNRs, their optical properties are dependent on the edge status and width, meaning that it is possible to modify their optical behavior by tuning the edge states (Berahman et al., 2015; Cardoso et al., 2018). For GNR arrays, the distance between GNR stripes also plays a significant role in modifying their optical responses. Due to the enhanced density of states (DOS) at van Hove singularities (VHs), strong optical absorption occurs when the incident photons' energy corresponds to the energy differences of the sub-bands. Each VH belongs to a special sub-band with sub-band number n assigned as an integer number denoting the magnitude of the sub-band state. ZGNRs and AGNRs have different edge-dependent absorption selection rules regarding optical properties (Chung et al., 2016; Lin & Shyu, 2000). For ZGNRs, $|\Delta J|$ = odd, where J is the sub-band index and ΔJ is the difference between the valence band index and conductance band index, meaning that optical transitions occur only between two sub-bands with a difference in index with an odd number, as shown in Figure 2.5 (a). For AGNRs, $|\Delta J| = 0$, meaning that optical transitions occur only from the valence to conduction sub-bands with the same index number, as shown in Figure 2.5 (b). As a geometrical parameter, since the curvature of CNTs can affect boundary conditions while calculating the spatial distribution of wave functions, it further affects the transition selection rules. Also, since CNTs are cylindrical in geometry, the optical absorption of CNTs is significantly different from GNRs; CNTs have no

open edges, thus the selection rules are not edge dependent as they are for GNRs. Additional details about the optical properties of CNTs are provided by Chung et. al. (Chung et al., 2016).

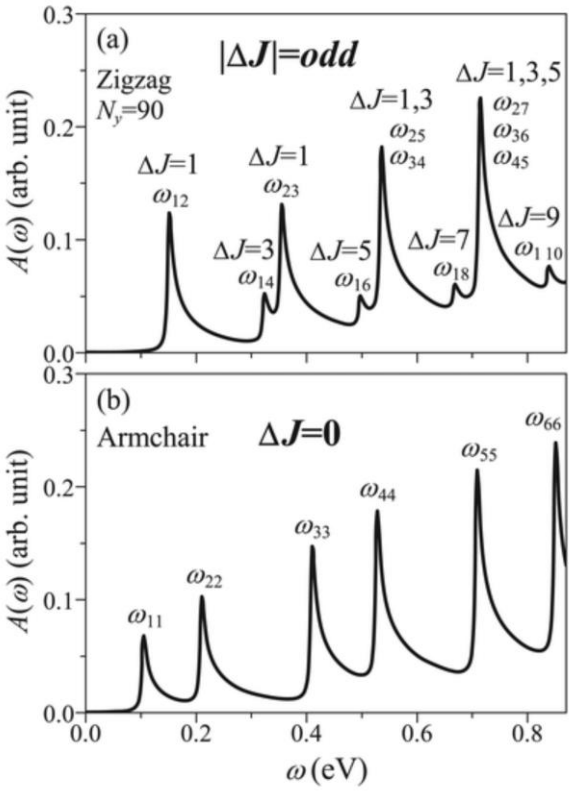

Figure 2.5. Low-energy absorption spectra for Ny = 90, where Ny stands for the number of armchair or zigzag line along the length of the ribbon (a) ZGNR and (b) AGNR (Chung et al., 2016).

2.2.3 Thermal properties

Both CNTs and GNRs have been shown to demonstrate exceptional thermal transport properties (Guo et al., 2009; Kwon & Kim, 2006). Guo et. al. utilized the nonequilibrium molecular dynamics method to investigate the thermal conductivity of AGNRs and ZGNR; The thermal conductivity was found to be strongly depending on length. For ZGNRs, the thermal conductivity increases initially and then decreases with increasing N, while for AGNRs, the thermal conductivity monotonously increases with N, as shown in Figure 2.6 (Guo et al., 2009).

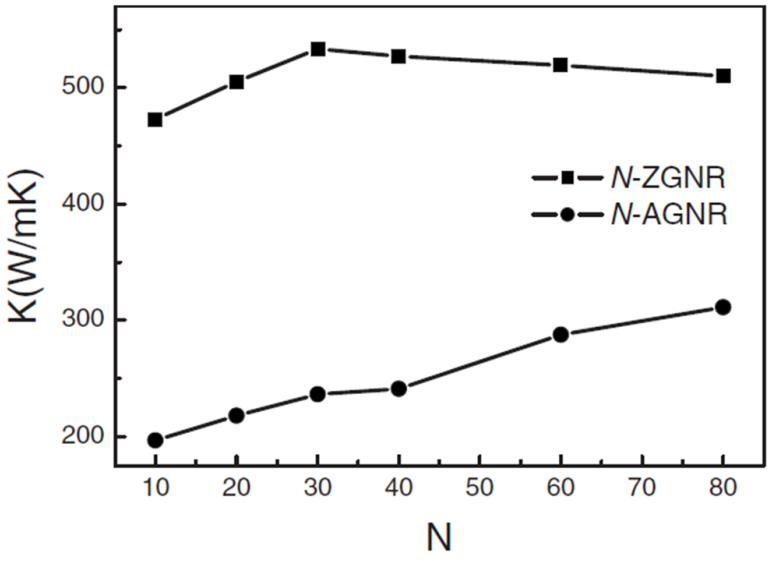

Figure 2.6. Thermal conductivity of an AGNR and ZGNR. The length of GNRs is fixed at 11 nm, and N varies. The ZGNR's thermal conductivity increases first and then decreases with *N* increasing, while the AGNR's thermal conductivity monotonously increases with *N*. (Guo et al., 2009)

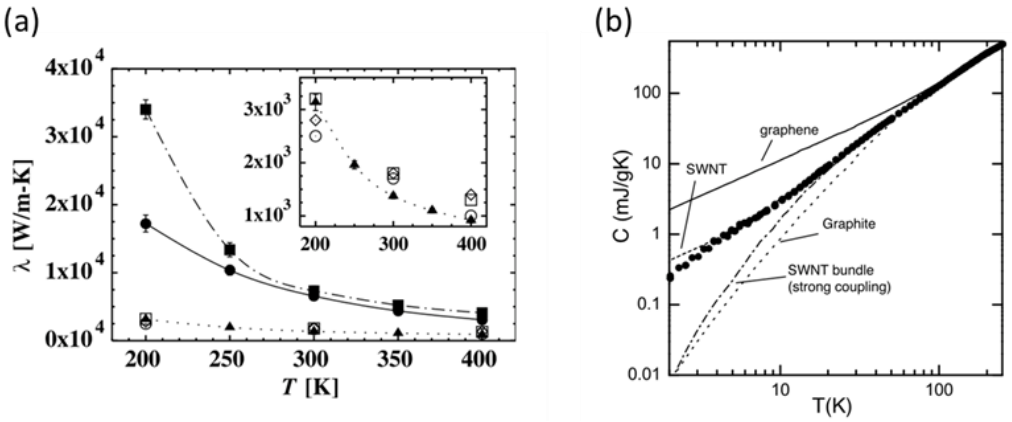

Figure 2.7. (a) Thermal conductivity of a (10, 10) CNT (solid line) and constrained graphite monolayer (dash-dotted line) (Kwon & Kim, 2006); (b) Specific heats versus temperature of members in the carbon family (Hone et al., 2000).

Figure 2.7 (a) shows the thermal conductivity of an isolated nanotube (10, 10), which is similar to the thermal conductivity of an isolated graphene monolayer. Figure 2.7 (b) shows the specific heat of the members of the carbon family. Phonons are the dominant thermal excitations in graphite, graphene, and nanotubes, and the phonon-specific heat C_{ph} dominates specific heat for most temperatures. C_{ph} depends on the phonon density of states and can be obtained by integrating

together with a temperature-dependent convolution factor that considers the temperature-dependent occupation of each phonon state (Hone et al., 2000). Further details on this topic are provided by (Kwon & Kim, 2006).

2.3 Synthesis of CNT

Laser vaporization and carbon arc synthesis are two relatively efficient methods to synthesize single-wall CNTs, both of which require catalysts. Another commonly used synthesis technique is the chemical vapor deposition (CVD) method. The arc discharge method (shown in Figure 2.8(a) below) utilizes high-purity graphite rods as the anode and cathode; a direct-current arc voltage is applied across two graphite electrodes immersed in an inert gas such as a helium atmosphere, resulting in a stable arc voltage of 12–25 V (Journet et al., 1997). Fullerenes are deposited as soot inside the chamber, and multi-walled CNTs are deposited on the cathode. Single-walled CNTs are generated when a graphite anode contains a metal catalyst (iron or cobalt; also alloys are being studied). An arc is produced across a 1 mm gap which causes the nanotubes to deposit on to the cathode as the anode is being consumed during the process. This process can produce both MWCNTs and SWCNTs. If the electrodes are doped with metallic catalysts, SWCNTs will be obtained, whereas if unmodified electrodes are used, MWCNTs will be produced (Bethune et al., 1993). The laser ablation method (Figure 2.8 (b) below) also utilizes the graphite target. In an inert atmosphere of 500 Torr of Ar or He, the graphite is vaporized by a laser. Specifically, carbon is vaporized from the surface of a solid disk of graphite into a high-density helium (or argon) flow, using a focused pulsed laser. Figure 2.8 (c) shows the CVD technique which utilizes a gaseous carbon feedstock, such as ethanol, methane, benzene, naphthalene, camphor, alcohol, carbon monoxide, hexane, cyclohexane, or anthracene, which is passed through transition metal (Fe, Ni, and Co) nanoparticles, which act as catalysts at elevated temperatures

(550–800°C) in a furnace. The CVD method is the most common method currently to synthesize CNTs. Whether the output is SWCNTs or MWCNTs will depend on the growth parameters, such as the catalyst and growth temperature, size, and density of catalysts, etc. CVD has more flexible control over the shape and size of CNTs than the other two methods.

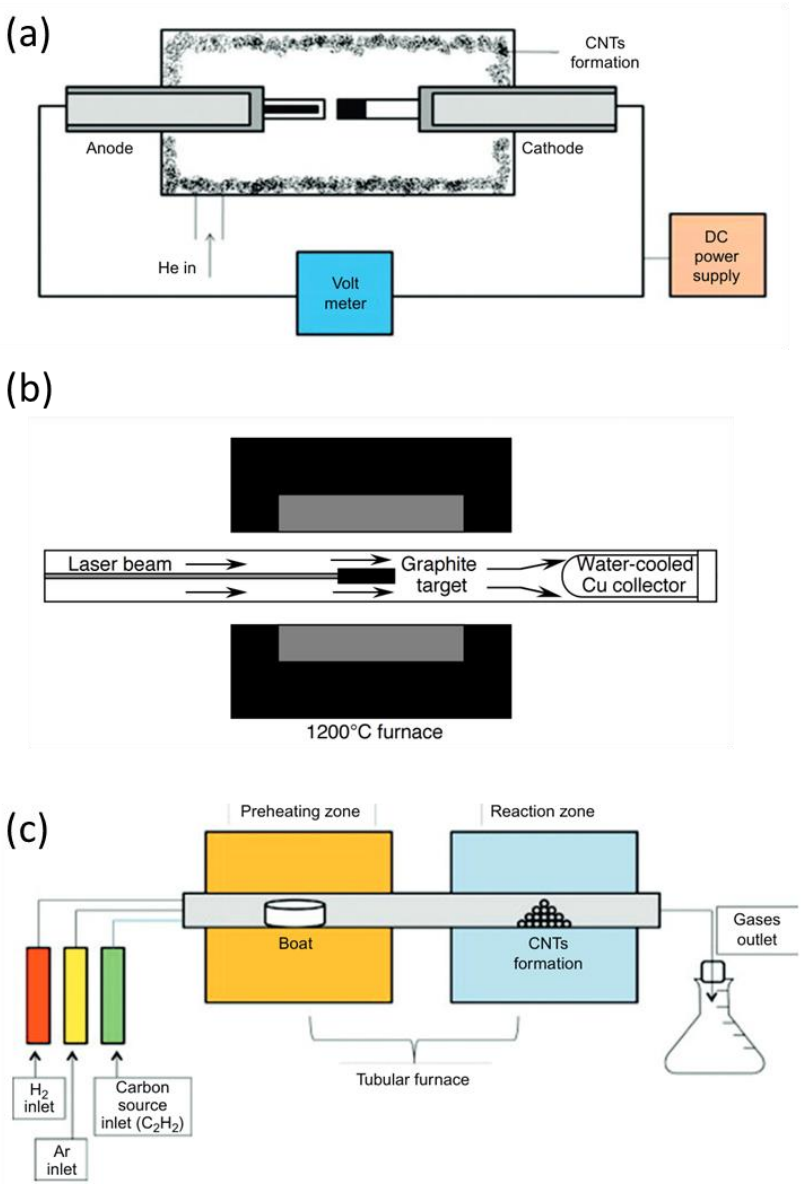

Figure 2.8. Different methods to synthesize CNTs. (a) Arc discharge method (Journet et al., 1997); (b) laser ablation method (Journet & Bernier, 1998), where the particles flow into an inert gas environment; (c) chemical vapor deposition (Mubarak et al., 2014).

2.4 Synthesis of GNRs

Multiple methods have been explored and developed to obtain GNRs. Using a chemical synthesis route, effective control of molecular species was recently demonstrated to form herringbone GNRs; however, post-processing techniques, as well as methods for precise placement on the whole wafer, are still needed for large-scale applications (Kimouche et al., 2015; Rizzo et al., 2018). Xu et al. reviewed some common techniques to produce GNRs including top-down lithographic approaches (by cutting graphene), bottom-up growth methods (utilizing restructured sites), and unzipping CNTs; they also discussed challenges associated with these methods including defects, rough edges, and high costs (Xu & Lee, 2016). CNTs, being small in diameter, could be used for producing nanoribbons. Indeed, there have been many studies on unzipping or etching of CNTs that have shown promise in producing GNRs using various methods including sonochemical etching, oxidative unzipping with subsequent reduction, selective gas-phase reaction etching, plasma etching, electrochemical unzipping, and etching with hypervelocity application (Jiao et al., 2009; Kosynkin et al., 2009; Ozden et al., 2014; Shinde et al., 2011; Wu et al., 2010; Zhang et al., 2006). While all these techniques have demonstrated the ability to produce nanoribbons, they all also risk exposing the whole sample including the support materials (such as silicon and oxide which are often used for making an electronic device) to reactive and/or corrosive environments.

2.4.1 Top-down approaches

To obtain a sufficiently large band gap, the width of GNRs needs to be less than 10 nm. Initially, researchers thought to use E-beam lithography (EBL), a sophisticated instrument to produce nanoscale patterns, to cut graphene to obtain nanoribbons. Han et al. exfoliated graphene

flakes from bulk graphite crystals and transferred them to a SiO_2-coated substrate, obtaining GNRs with a width of 10~100 nm by using a mask in photolithography and oxygen plasma etching. The bandgap of the nanoribbons was determined based on transport tests, with the results showing that the bandgap decreased with increasing nanoribbon width (Han et al., 2007). Utilizing electron beam exposure (Figure 2.9), Wang et al. (Wang & Dai, 2010) obtained GNRs by introducing NH_3 to the high-temperature oxidation etching method; the width of the nanoribbons was further reduced to less than 5 nm, leading to a room temperature switching ratio of 10^4 in field effect transistors fabricated from these GNRs. Another top-down method involves the scanning tunneling microscopy (STM) instrument, as shown in Figure 2.10. Magda et. al. reported the patterning of GNRs with well-defined widths and predetermined crystallographic orientations, utilizing STM lithography-based technology. They obtained semiconducting ribbons from graphene with predetermined energy gap values up to 0.5 eV(Magda et al., 2014).

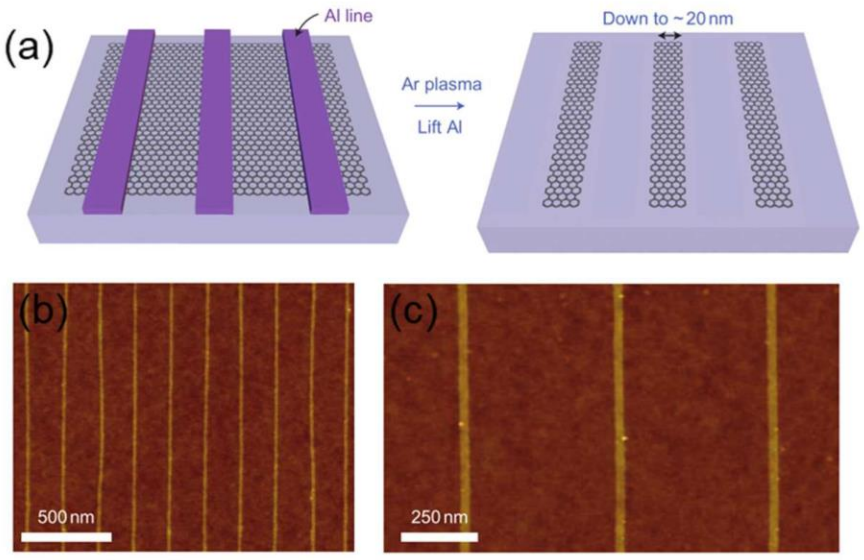

Figure 2.9. Top-down EBL (Electron Beam Lithography) method. (a) Schematic diagram of the EBL process; (b) and (c) AFM images of a GNR array with a width of about 20 nm and 22 nm, respectively (Wang & Dai, 2010).

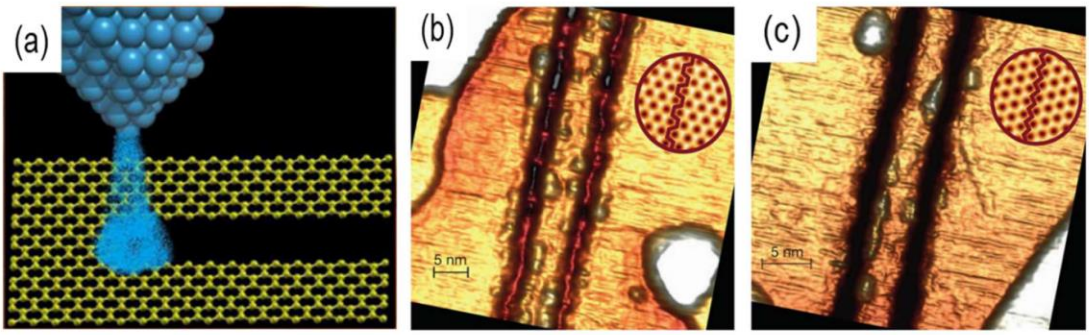

Figure 2.10. (a) Schematic diagram showing the use of STM (Scanning Tunneling Microscope) to cut graphene. (b) STM image of AGNR with the width of 5 nm through scanning tunneling nanolithography in a graphene sheet. (c) STM image of ZGNR with a width of 6.5 nm (Magda et al., 2014).

2.4.2 Bottom-up growth methods

Bottom-up methods regard GNRs as conjugated macromolecules composed of many benzene rings and obtain GNRs by reacting small molecular units with each other. Monomers are essential to chemically synthesize GNRs due to the flexibility in designing width and edge types with atomic precision by designing the structure of precursor monomers. GNRs obtained by chemical methods typically have uniform structures, which is the primary advantage of this method, particularly when compared with top-down methods. In 2010, Dai's group first introduced the preparation of GRNs by surface synthesis (Wang & Dai, 2010). Under the catalysis of the metal substrate, the specially designed molecular precursor undergoes dehalogenation polymerization, dehydrocyclization, and other reactions in sequence after annealing, thereby producing GNRs with armchair boundaries. Precursor molecules are the basic building blocks of nanoribbons in the surface synthesis method. Therefore, by appropriately designing the chemical structure of the precursor, the parameters such as the boundary structure and width of the product GNRs can be directionally changed (Moreno et al., 2018; Nguyen et al., 2017; Talirz et al., 2013). Through this method, effective control of the properties of the nanobelt is realized, which is

beneficial to the scientific and technological advancements. GNRs prepared by this method have atomically precise peripheral boundaries and uniform widths. The boundaries of the nanoribbons are also all saturated with hydrogen atoms, which is consistent with the theoretically calculated structural model of the nanoribbons (Figure 2.11) In addition, the synthesis method is simple, the synthesis efficiency is extremely high, and it can be used for growing many GNR materials. However, the biggest challenge of this method is transferring the synthesized GNRs to suitable substrates with precise position control, which is required for most GNR applications. Also, chemical free formation of GNRs leading to clean device fabrication in a whole wafer scale process is difficult to implement with GNRs obtained by this method (Li et al., 2008).

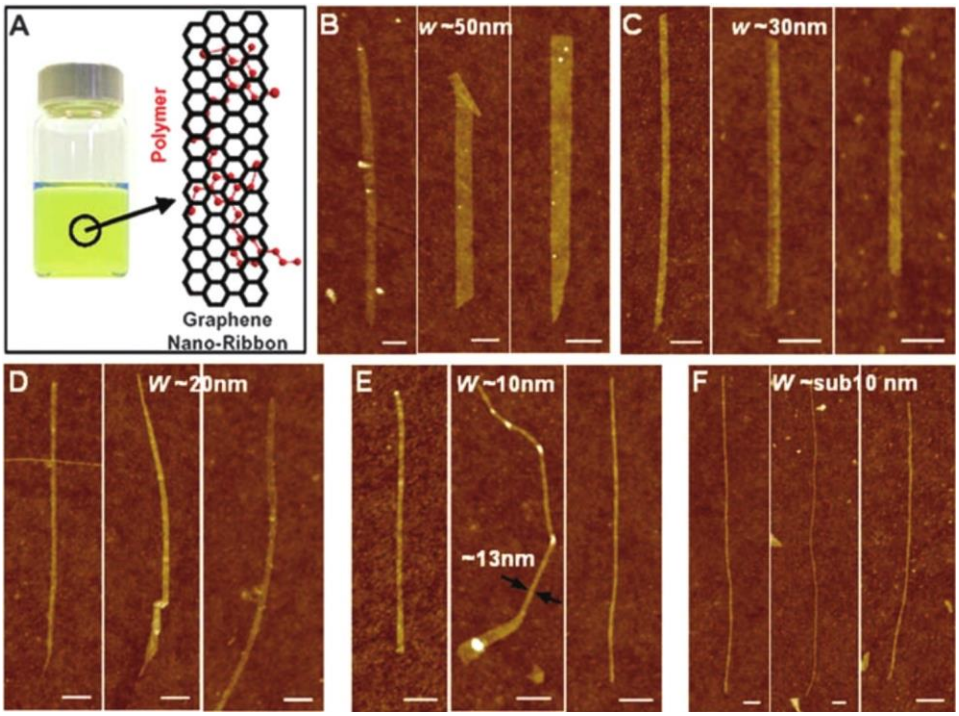

Figure 2.11. (a) Left: PmPV/DCE solution with GNRs; right: illustration of a GNR with PmPV polymer adsorbed on GNR; (b)-(f) AFM images of GNRs with widths ranging from 50 nm to sub-10nm. All scale bars indicate 100 nm (Li et al., 2008).

2.4.3 Unzipping CNTs

CNTs share many similarities with graphene, such as their nanoscale width and Q1D structure. A CNT can be unzipped longitudinally to produce a GNR. Also, single-walled CNTs can be converted to single-layer GNRs, and multi-walled CNTs can be converted to multi-layer GNRs. Unzipping can be achieved using chemical approaches and controllable RIE etching approaches to partially remove some top parts of a CNT to leave a GNR. Wet chemical reactions and dry etching processes have both been used successfully.

2.4.3.1 Chemical method

Kosynkin et al. reported an oxidation process in solution to cut multi-walled carbon nanotubes lengthwise (Kosynkin et al., 2009). This process yielded nearly 100% GNR structures with high water solubility. The advantage of their approach is that GNRs can be produced with controlled widths and edge structures with high quality by controlling the placement and alignment of the CNTs. They also noted that the use of few-walled CNTs produces sub-10 nm GNRs with bandgaps which are sufficient for room-temperature transistor applications. However, due to the existence of abundant oxygen-containing functional groups on the surface, the conductivity of the as-produced GNRs was not good. The conductivity can be improved by subsequent chemical reduction by N_2H_4 or annealing in H_2.

2.4.3.2 Plasma unzipping

Jiao et al. reported a gas-phase plasma etching process to convert CNTs to GNRs producing high-quality, and narrow GNRs. A two-step process was suggested to unzip nanotubes for the mass production of high-quality GNRs. Mild calcination at 500℃ in air induced oxidation of pre-existing defects to produce pits on the side walls of CNTs; sonication in organic solvents then effectively enlarged the pits and unzipped the CNTs to form GNRs. The GNRs were then purified by ultracentrifugation, producing narrow GNRs with a width of 10–30 nm. CNTs have also been

unzipped by catalytic cutting and pulse burning at high currents. As new methods for scalable fabrication of uniform CNTs and their alignment continue to be developed, the synthesis of GNRs by longitudinal unzipping of CNTs is also becoming a promising approach for the mass production of GNRs. This method could be further improved by synthesizing GNRs of uniform width with narrow width distribution, and GNRs of defined edges with specific chirality (Jiao et al., 2009).

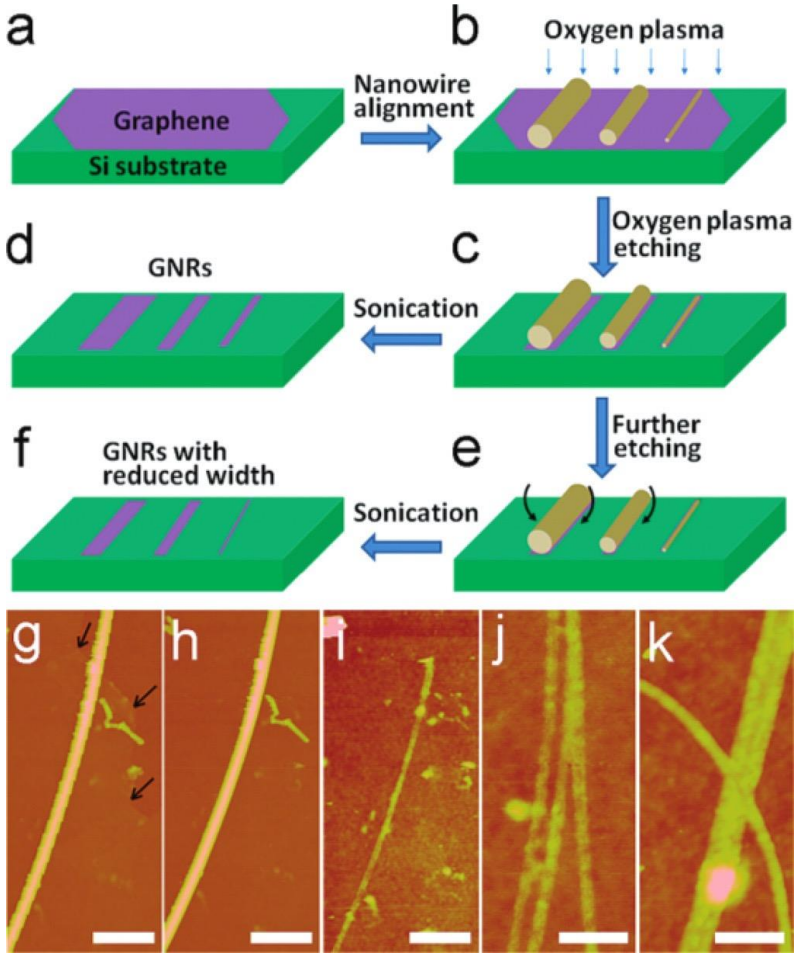

Figure 2.12. (a)-(f) GNR fabrication process by oxygen plasma etching with a nanowire etch mask; (g) and (h) AFM images of a nanowire etch mask on top of a graphene flake before and after the oxygen plasma etch, respectively. The scale bars are 300 nm and 100 nm in (g)-(i) and (j) and (k), respectively (Bai et al., 2009).

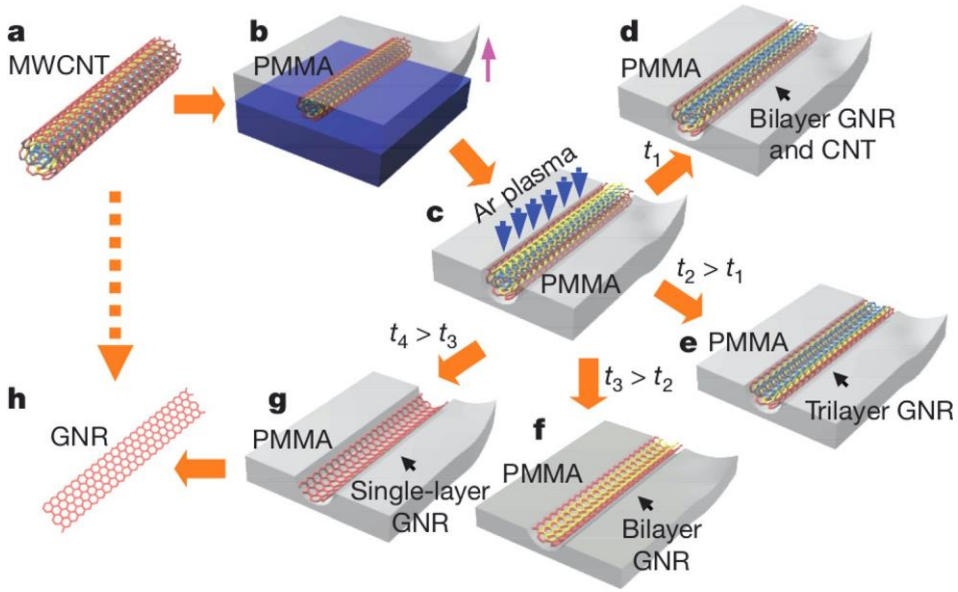

Figure 2.13. (a) A pristine MWCNT; (b) MWCNTs deposited on a Si substrate with coated PMMA; (c) coated PMMA/MWCNTs film peeled and exposed to Ar plasma; (d)–(g) potential GNR products depending on various etching time; (h) removal of the PMMA to obtain GNRs (Jiao et al., 2009);

2.4.3.3 Laser-based unzipping

Laser-based unzipping of nanotubes along their longitudinal direction to form GNRs has been reported; however, the study lacks clarity and did not pay attention to a systematic mechanism to understand the process, making it hard to control (Kumar et al., 2011). For example, study by Kumar et al. used a nanosecond laser to thermally excite nanotubes suspended in an aqueous solution and demonstrated the unzipping of the tubes, but it does not report the specific tube's shape, size, and electronic properties before and after the laser exposure to precisely understand the phenomena associated with the light-matter interaction. Also, the nanotubes are suspended in a solution that absorbs laser radiation, which makes the process complicated to analyze. Han et al. used picosecond and femtosecond laser excitation to exploit processes far from equilibrium (as described in this work) involving electron-phonon heating (Han et al., 2007). While they observed various carbon morphologies, including diamond nano bundles, the process did not result in any nanoribbon formation. However, there were no clear indications of phase transformation from one

type of carbon atom hybridization to another (e.g., sp^2 to sp^3). The ability to precisely manipulate the material structure in the nanometer scale with high spatial control is necessary for creating the building blocks for numerous scientific and technological topics including quantum science and quantum technologies. The limitations discussed in the above techniques highlight the need for a manufacturing technique that would enable to fabricate ultra-narrow GNRs with a large yield, chemical-free ribbons and tunable structures.

Chapter 3 - Characterization Methods on Individual MWCNTs

Individual nanomaterial characterization in terms of their detailed physical, chemical, thermal, optical, and electrical properties is very important to further understanding of science at nanoscale materials and their use in technological applications. Extensive research has been made in the growth and characterization of carbon nanotubes (CNTs) over the past three decades, yet new phenomena in growth science are emerging, often as a result of practical needs to build new technologies. For example, even today it is challenging to grow CNTs at low enough temperatures to be compatible with semiconductor processing for heterogeneous integration. Likewise, for studying GNRs it is not only critical to design a room-temperature process but also it is important to study fundamental process-structure-properties correlations of the CNTs involved in the light-matter interaction.

Although several techniques can be used to investigate the morphological and structural characterizations of CNTs, only a few techniques can characterize them at the individual level, such as atomic force microscopy (AFM), scanning tunneling microscopy (STM), and transmission electronic microscopy (TEM). In this chapter, we will discuss various analytical techniques for the CNTs and GNRs used in this thesis: AFM is discussed in Section 3.1, while electron microscopy is in Section 3.2. In addition to the microscopy techniques, we will discuss other techniques, such as Raman spectroscopy (in Section 3.3), that includes traditional Raman spectroscopy as well as tip-enhanced Raman spectroscopy (TERs). While Raman spectroscopy is a widely used characterization technique for structure and chemical footprint of nanomaterials, other techniques focusing on the chemical functionalization of CNTs and GNRs, such as energy-dispersive X-ray spectroscopy (EDX), that can also provide bulk chemical information on CNTs, and X-ray photoelectron spectroscopy (XPS), that is helpful to determine the chemical structure

of nanotubes. Neither EDX nor XPS is discussed in the present work but suggested for future studies to conduct. In the last section, we use the Tip-Enhanced Raman Spectroscopy technique to analyze the relevance between the properties of individual MWCNTs.

3.1 Atomic Force Microscopy (AFM)

AFM is based on the interaction force between a sharp metallic tip (typical diameter ~ 5 – 10 nm) and the sample to reconstruct the topography of the surface, and hence, image at the atomic scale. It is used to characterize the topographic structure of a sample surface. However, many other physical details of the sample beyond the topographic structure can be studied by AFM. Figure 3.1 shows the components in an AFM tool, including a scanning microscope, a feedback controller, and a computer to control the setup and display the images during the scanning. The method broadly falls under the category of a so-called scanning probe microscopy (SPM) along with scanning tunneling microscopy, where a sharp probe is used to scan across the surface of interest and an information at nanoscale is gathered by monitoring and understanding the probe-sample interactions. Three modes of operation of AFM are generally used: contact mode AFM, non-contact mode AFM, and a tapping mode AFM. The studies described in this dissertation are made using tapping mode AFM where a scanning tip is attached to the end of an oscillating cantilever when scanned across the surface of the sample. Usually, the cantilever oscillates at or slightly below its resonance frequency with the tip repeatedly and gently tapping onto the sample surface. The general principle is the following: an AFM tip is fixed onto an end of a tiny oscillating cantilever. A laser beam with small diameter hits the cantilever/tip end and is reflected towards a quadrant photodetector device (shown in Figure 3.2). When the tip scans on the surface of the sample, a preset interaction force between the tip and the sample causes a deflection of the cantilever. This deflection continually gets monitored by the photodetector which further gets

feedback controlled by the controller. In this way, the force between the tip and the sample is "mapped" to reconstruct the surface topography of the sample. When the AFM is operating, the interaction forces between the tip and the sample include the van der Waals force, the electrostatic force (the interaction distance is tens of nanometers), and the short-range chemical force (the interaction is several angstroms). Figure 3.2 (a) shows schematic working principle of tapping mode and (b) shows the laser path followed inside the scanner and finally gets guided towards the detector. This AFM is suitable for operation in atmospheric conditions.

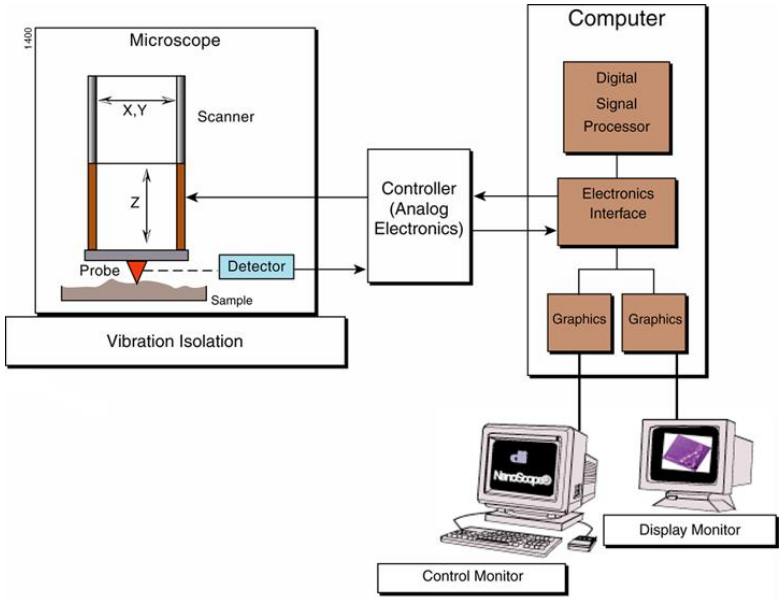

Figure 3.1. Basic SPM components (Thornton, 2000).

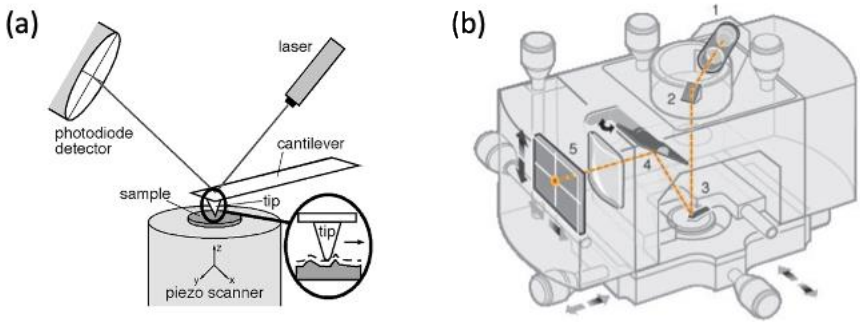

Figure 3.2. AFM working principle. (a) Tapping mode; (b) laser path inside a scanner: 1. laser; 2. mirror; 3. cantilever; 4. tilt mirror; 5. photodetector. (Thornton, 2000).

AFM has two operational modes: quasi-static and dynamic. The quasi-static mode is the simpler AFM working mode. Its principle is based on a simple spring model that considers the elastic coefficient of the cantilever to be constant (k). For a certain deflection q, ($F = k \cdot q$), the feedback system in the circuit maintains constant deflection (q), and the value of vertical height (Z) is recorded to obtain the topographic structure of the sample. Due to the existence of the long-range van der Waals force in this mode, the tip can be easily absorbed into the sample surface during scanning, resulting in damage to the sample surface. In dynamic mode, the cantilever vibrates around its eigenfrequency when the needle tip is scanned, which can be divided into amplitude modulation and frequency modulation according to the feedback mechanism.

The tapping mode AFM that operates in atmospheric conditions uses amplitude modulation. In this mode, the interaction force between the tip and the sample changes the vibration amplitude of the cantilever. The feedback system maintains constant amplitude by changing the height of the tip and records its position. The change in height generates the surface topography of the sample. The non-contact AFM used in this study utilizes frequency modulation, such that the tip vibrates at a constant amplitude at its resonant frequency while scanning the image, and the system records the change of the resonant frequency and image.

Unlike optical microscopy, where the resolution is limited by the optical diffraction limit, AFM breaks the diffraction limit to capture images of much smaller spatial dimension due to above mentioned operational principles involving the interaction forces. However, the direct force interactions that provide the advantages of AFM over other analytical techniques are also the source of many of its limitations. One such limitation is that while the surface is very flat, the interaction is limited to only the apex of the probe tip, however, as the surface is featured with variations in height beyond a certain limit, the shape of the probe structure can dominate the tip-

sample interaction and introduce tip artifacts that can obscure the data. Another significant limitation of AFM is that it can only characterize the surface features of CNTs and GNRs, for example, in contrast, to the detailed internal structure, such as the number of walls of CNTs and information about their micro-domain etc. as measured by TEM. It is complex to observe and analyze structures with nanometer dimensions. In addition to the sample preparation, it is also important to develop specific protocols for other processes involved in the measurements, such as analysis criteria, evaluation and interpretation of the results, analysis reliability and repeatability, and sample storage.

3.2 Electronic microscopy

In contrast to the optical diffraction limit in an optical microscope, the wavelength of electrons is much smaller than that of photons. The visible light wavelength range is approximately from 400 nm to 760 nm, while the wavelength of electrons is dependent on their energy, making it as small as 3.7 pm at 100 keV, 2.5 pm at 200 keV, and 1.97 pm at 300 keV. Therefore, the resolution of an electron microscope is sufficiently smaller for imaging nanomaterials such as CNTs and GNRs. However, with available practical instrumentation involved, typically the resolution is limited to ~ 0.1 nm due to the objective lens system in electron microscopes. Despite this limitation, it is sufficient to image the wall structures in MWCNTs.

There are two types of electron microscopy: scanning electronic microscopy (Klimenko et al.) and tunning electronic microscopy (TEM). Figure 3.4 shows the SEM (Versa 3D™ DualBeam™ from FEI company) and TEM (Hitachi H-8100Transmission Electron Microscope) instruments used in this project. An electron microscope uses a beam of accelerated electrons as a source of illumination. Ernst Ruska, a German engineer, built the first electronic microscope in 1931, based on the same principle (Ruska, 1987) that still applies to modern electronic microscopy.

When electrons enter the specimen, the electrons interact with the specimen and gradually lose their energy. The incident electron is referred to as the primary electron and the electrons that are produced by the electron-matter interaction are referred to as the secondary electrons. The scattering range of the electrons is dependent on the energy of the primary electrons, the atomic weight of the elements in the specimen, and the density of the atoms. The scattering range increases with the energy of the primary electrons and is also influenced by the thickness of the specimen. Thinner specimens experience more scattering events than thicker specimens. When samples are irradiated by an electron beam, three mechanisms occur on the sample surface or near-surface: the elastic scattering of electrons as the backscattered electrons (BSE), the inelastic scattering of electrons as the low-energy secondary electrons (SEs) and Auger electrons, emitted photons as the X-ray emitted and cathodoluminescence from the atoms. Figures 3.3 (a) and (b) illustrate the scattering process involved in thick specimens and thin specimens, respectively. In SEM, one generally uses thicker samples and the major scattering process involved are SEs and BSEs, whereas in TEM, one uses thinner sample, and the images are generally constructed from the transmitted electrons.

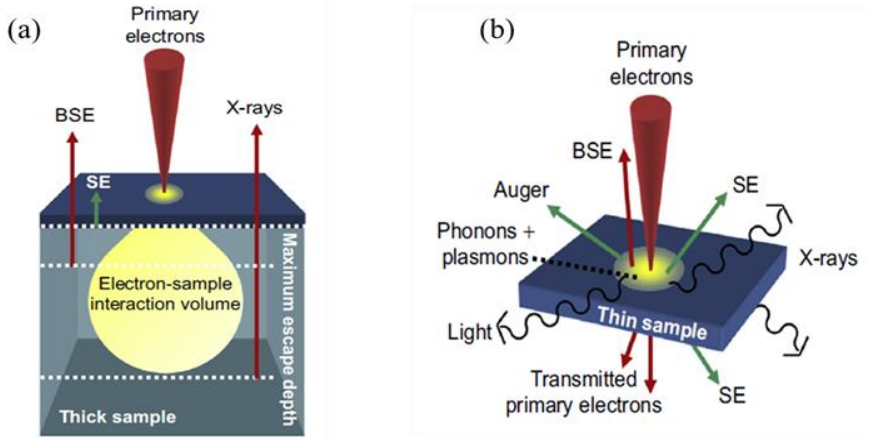

Figure 3.3. Interaction between primary electrons and (a) thick specimens; (b) thin specimens.

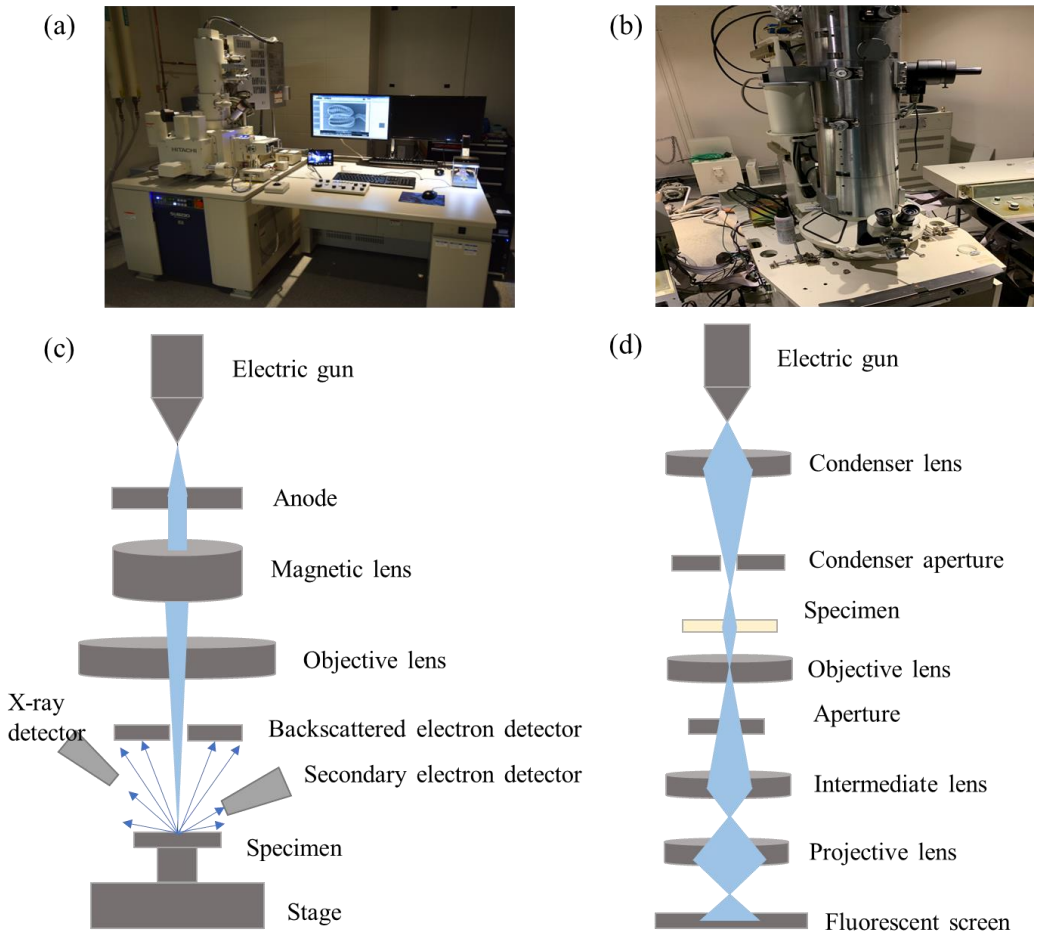

Figure 3.4. (a) SEM (Versa 3D™ DualBeam™ from FEI company); (b) TEM (Hitachi H-8100); (c) and (d) illustrate SEM and TEM components, respectively designed by the author.

As shown in Figure 3.4, both SEM and TEM include an illuminating system (electron gun and condenser lens), specimen manipulation system (specimen stage for SEM, specimen holder for TEM, and related hardware), an imaging system (objective lenses, projector, and intermediate lenses, and detector), and vacuum system (mechanical pump, oil diffusion pump, and/or ion pump). The main difference between SEM and TEM is the mode of imaging: SEM detects the reflected or knocked-off electrons from the surface while TEM detects the transmitted electrons. SEM can directly gain information on the size, size distribution, and shape of the CNTs and GNRs.

TEM can acquire information about internal structures because the electron beam passes through nanomaterial. Due to the fact that TEM uses transmitted electrons, the samples must be very thin (less than 150 nm). This raises another important difference between these two methods, that is the sample preparation.

Specimen preparation for SEM is simple; the specimen can be thick bulk material, powder, or nanoparticles sprayed on the surface of a supporting substrate. However, a dry and clean sample is needed to obtain a better characterization of the material. If the sample is non-conductive, a proper coating of ultrathin metal layer is required to flow the electrons accumulated on the surface to the ground. Common coating materials are gold, platinum, and iridium; specific coating materials may be required for certain samples.

In contrast, sample preparation for TEM is more complex. To allow the electrons to pass through the specimen, they must be very thin (typically less than 100 nm) and relatively flat. Meshed grids of metals and/or conductive elements can be used to hold samples. For the CNT samples used in this project, three factors are critical in the preparation of a successful sample: the density of the CNTs, the concentration of the solvent N-dimethylformamide (DMF) in which CNT dispersion is made, and any other intermediate substances such as surfactants used in the dispersion (in our case, no surfactants are used). Figure 3.5 shows examples of SEM and TEM images of the MWCNTs used in this study. As can be seen in the figure, TEM can offer higher resolution than SEM, where individual walls and the spacing between them is apparent (0.35 nm).

When switching the SE detector to the X-ray detector, energy-dispersive X-ray analysis can be performed. Both SEM and TEM can perform X-ray spectrum analysis. This technique can be used to obtain elemental profiles across nanoscale features. There are other applications of TEM, such as EELS (electron energy loss spectroscopy), but that is outside of the scope of this

study. Here, SEM imaging was obtained using an FEI Versa 3D Dual Beam Field Emission SEM and high-resolution transmission electron microscopy (HRTEM) imaging was achieved using an FEI Tecnai F20 XT Field Emission Transmission Electron Microscope at 200 kV energetic electrons.

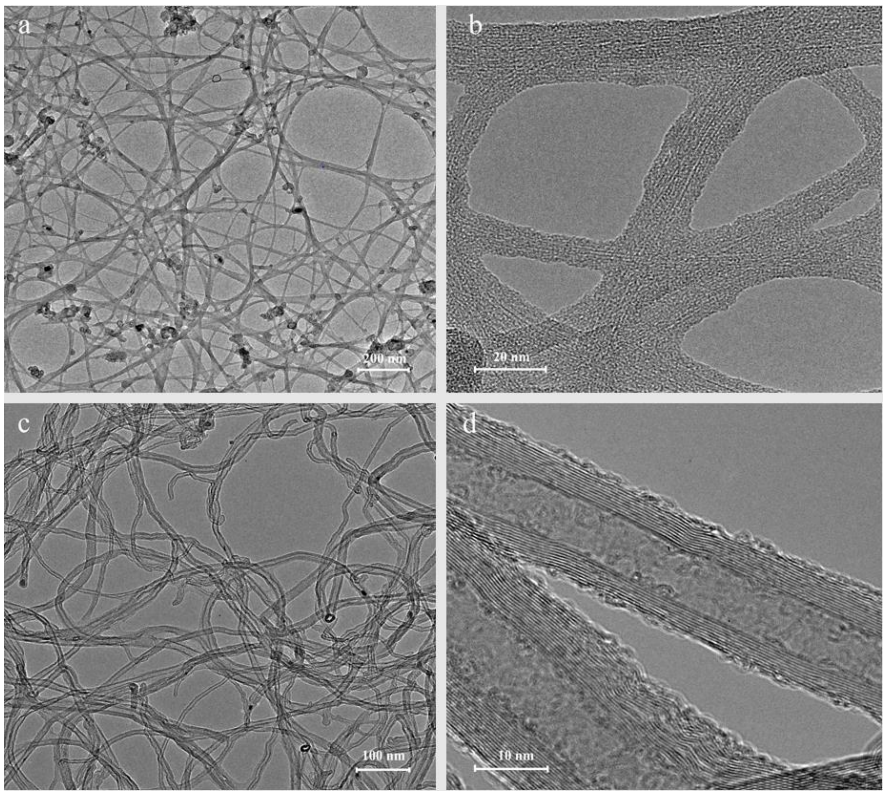

Figure 3.5. (a) and (b) SEM images of starting MWCNT; (c) and (d) TEM images of MWCNT.

3.3 Traditional Raman spectroscopy of graphene-based materials

3.4.1 Raman spectroscopy principle and instrumentation

When shining laser light on a material, the incident photon interacts with a molecule or crystal lattice and is scattered elastically or inelastically. As a result, when the scattered photon energy equals the energy of the incident photon, it is referred to as Rayleigh scattering. In contrast, when the energy and momentum of scattered photons shift from the incident photons, it is referred

to as Raman scattering. During the scattering, both the energy and momentum are governed by the conservation laws, which is expressed as $\omega_s = \omega_i \pm \omega_v$ and $k_s = k_i \pm k_v$ respectively, where subscript "s" denotes the scattered photon, subscript "i" denotes the incident photon, and subscript "v" denotes the vibrations of the molecule or the crystal lattice while interacting with the incident photon. Raman spectroscopy is a technique based on Raman scattering phenomena. A Raman spectrum records the scattered photons' energy (intensity) as a function of the shift of energy in wavenumber (cm^{-1}) from the incident light (the Raman shift). It is a fast, nondestructive, and high-resolution tool for characterizing the lattice structure and the electronic, optical, and phonon properties of carbon material.

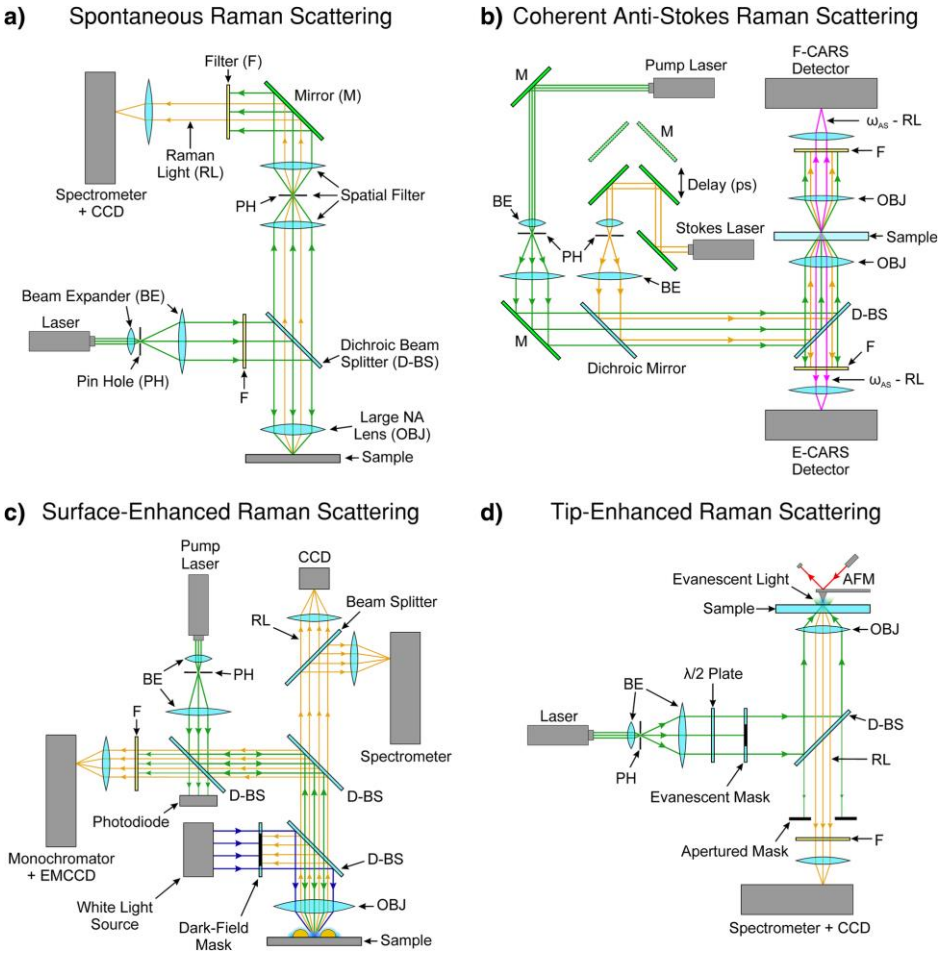

Figure 3.6. Instrumentation of four major Raman spectroscopy techniques (Jones et al., 2019).

Researchers have developed many types of Raman spectroscopy techniques based upon a variety of applications; Figure 3.6 shows the instrumentation involved in four major Raman techniques. Further details of spontaneous Raman scattering, coherent anti-stock Raman scattering, surface-enhanced Raman scattering, and tip-enhanced Raman scattering are provided in Jones' review (Jones et al., 2019). The Raman technique that the dissertation exploits to measure the CNT and GNR samples is a confocal Raman microscopy, which combines optical confocal microscopy and a Raman spectrometer, as shown in Figure 3.6 (a). In this technique, the incident laser is spatially filtered through a pinhole in front of the spectrometer. A notch filter is then used to filter the back-scattered Raman light. A spectrometer with an attached charge-coupled device CCD camera is used to detect the Raman signal. To differentiate from tip-enhanced Raman spectroscopy, confocal Raman spectroscopy will be referred to as traditional Raman spectroscopy herein.

3.4.2 Typical Raman peaks of CNTs and graphene

Raman spectroscopy is a powerful technique used to characterize nanomaterials. In this study, we use a Renishaw in-Via Raman spectrometer with a 514 nm excitation source with a resolution of 0.3 cm^{-1} in a backscattered configuration. The setup uses a microscope with a 100X objective lens to take the Raman spectra for MWCNTs and GNRs formed from MWCNTs. The laser spot size is about 1 um in diameter. In the measurements, a circularly polarized light is used to obtain the Raman spectrum.

Figure 3.7 (a) shows the typical Raman peaks of carbon nanomaterials. The wavenumbers and attributions of different Raman peaks the carbon nanomaterials are presented in Figure 3.7 (b).

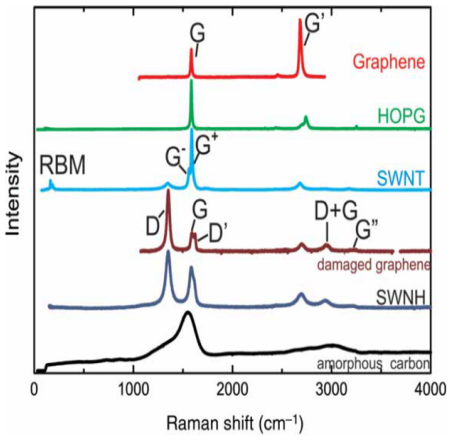

Mode	Frequency/cm-1	Attribution	
G	1580	Tangential vibration of the graphitic carbon atoms	Graphene, CNT, GNR
G' (2D)	2700	2nd order two-phonon scattering, interband	Graphene, CNT, GNR
D	1330-1360	Disordered amorphous carbon	Graphene, CNT, GNR
D'	1620	2nd order two-phonon scattering, intraband, Double resonace	Graphene, CNT, GNR
RBM	120-250 for d=1~2nm	Radial breathing mode, atomic vibration in the radial direction	CNT
G+	1587-1592	Atomic displacement along the tube axis	CNT
G-	1550-1570	Atomic displacement along the circumferential direction	CNT

Figure 3.7. (a) Typical Raman peaks of carbon nanomaterials (Saito et al., 2011); (b) Summary of attributions of different Raman modes.

It should be noted that the excitation laser energy is important for resonant Raman spectroscopy. Studies have shown that certain exciting laser energy is needed to promote specific Raman peaks. Raman peaks can also be used to identify the electronic properties of an SWCNT. For metallic CNTs, the G- line shape is a broadened Breit Wigner Fanoline shape; or semiconducting single-walled carbon nanotubes (SWCNTs), the G- line shape is a Lorentzian shape. Furthermore, the splitting of G+ and G- can be used to predict the diameter range (Saito et al., 2011), as shown in Figure 3.7 (a) and (b). Another method of determining the diameters of the nanotubes is the presence of the radical breathing mode (RGB) in the Raman spectrum at low wavenumber values.

3.4 Tip-enhanced Raman spectroscopy (TERs) studies on CNTs

3.4.1 Current state of knowledge of TERs on CNTs

TERs is an effective and powerful technique to characterize individual CNTs because 1) it provides structural and chemical information down to the nanometer scale or even under single molecular detection because of its extraordinary spatial resolution, and 2) it is nondestructive,

label-free, and easy to operate under ambient conditions (Mahapatra et al., 2020; Schultz et al., 2020; Stöckle et al., 2000; Yano et al., 2009; Zhang et al., 2019).

A SWCNT can be treated as a graphene layer rolled into a cylinder, while a MWCNT can be treated as a cylinder formed by multiple graphene layers. Thus, besides the typical Raman peaks that belong to graphene (D, G, and 2D peaks) (Childres et al., 2013), CNTs possess new Raman peaks rising from the rolling behavior, as a result of breaking the original symmetry and boundary condition of the graphene. These new signatures include presence of a radial breathing mode (RBM) peak and the splitting of the G peak (G+ and G- peaks) (Childres et al., 2013; Dresselhaus & Eklund, 2000; Rao et al., 1997; Saito et al., 2011). Individual CNTs have been investigated by near-field Raman spectroscopy and TERs both experimentally and theoretically. Most studies have focused on using Raman spectroscopy on individual SWCNTs (Anderson et al., 2007; Chen et al., 2014; Liao et al., 2016; Maciel et al., 2008; Milnera et al., 2000; Okuno et al., 2013; Rao et al., 2012; Yano et al., 2013). Fewer studies have been conducted on isolated double-walled or triple-walled CNTs (Bandow et al., 2002; Heeg et al., 2018; Hirschmann et al., 2013; Villalpando-Paez et al., 2008), as well as individual MWCNTs (Chaunchaiyakul et al., 2016; Kato et al., 2020; Zdrojek et al., 2012). Novotny et. al. (Anderson et al., 2007) reported a change in the chirality based on mapping two resonant RBM phonon frequencies along spatially isolated SWCNTs by using near-field Raman spectroscopy. They mapped both the transition from semiconducting-to-metal and metal-to-metal chirality at the individual nanotube level and determined the spatial resolution of the transition region to be 40–100 nm. Rao et al. (Rao et al., 2012) provided evidence of the chiral-selective growth of SWCNTs. They conducted in situ Raman spectroscopy measurements of individual SWCNTs and correlated them with their chiral angles during growth and showed that the growth rates are directly proportional to the chiral angles.

A noteworthy study performed by Okuno et. al. showed that a phenomenon of semiconductor-to-metal transition of an SWCNT occurs near the extremely localized X cross junction area by utilizing state-of-the-art TERS spectroscopy and microscopy techniques (Okuno et al., 2013). The change in electronic properties of a SWCNT can only be identified at extremely high spatial resolutions. Yano et al. (Yano et al., 2013) developed a TERs technique utilizing a silver-coated nanotip and imaged the stain distribution along an individual SWCNT. By nanoimaging of the AFM nanotip-induced localized strain, they confirmed the strain of the manipulated SWCNT depends on its diameter and chirality. TERs is an improved technique in comparison with the previously used TEM due to its ability to measure the Raman modes arising from the symmetry breakdown caused by the atomic rearrangement on the inner and outer surfaces of the nanotube. Another study conducted by Hayazawa et al. (Chen et al., 2014) utilized the scanning tunneling microscopy-based TERs technique to simultaneously measure the chemical and structural properties of individual SWCNTs. They distinguished several types of CNTs and obtained the properties of the CNTs such as the diameter, local defects, and bundling effects while using the TERs measurement with a spatial resolution of 1.7 nm. Later, Dong's group improved the spatial resolution of TERs measurement to a sub-nanometer region of 0.7 nm due to the high TERs enhancement factor induced by the nanogap between the silver nanotip and silver substrate. With such a high spatial resolution, it is possible to visualize the D band scattering induced by defects and track the strain-induced spectral evolution (Liao et al., 2016).

Double-walled carbon nanotubes (DWCNTs) are simple systems to study the interaction between two concentric graphene layers. Individual DWCNTs with four possible metallic and semiconducting configurations were investigated by resonant Raman spectroscopy. Villalpando-Paez et al. concluded that the Raman bands could be used to confirm the different types of

configurations and that the G peak is sensitive to interlayer interactions (Villalpando-Paez et al., 2008). Another study conducted by Heeg et al. related to TERs on DWCNTs investigated the relationship between the long linear carbon chains encapsulated inside the DWCNTs and its host carbon nanotube. The authors concluded that the inner tube of the host CNT determines the vibronic and electronic properties of the long linear carbon chains (Heeg et al., 2018).

Raman spectra of MWCNTs are more complex than those of SWCNTs due to the increased graphene layers and interwall interactions. The signatures of the SWCNT Raman band indicate the presence of the low-frequency RGB and the splitting of the G peak into G+ and G- modes. These are often not observed in MWCNT Raman spectra, especially when Raman spectra spatial resolution is insufficient. The G band is often used to distinguish SWCNTs and MWCNTs. Unlike the splitting of the G band in SWCNTs, the G band in MWCNTs appears to be a broad symmetric band for traditional Raman spectra and multiple splitting in TERS measurement.

Nanot et al. (Nanot et al., 2010) studied double sharp line features in the G-band of an individual MWCNT by resonant Raman spectroscopy in FET configuration at room temperature. They observed a multipeak G- band spectrum of an MWCNT comprised of four distinct modes and proposed a straightforward way to assign each peak to a distinct shell. For the G+ band, the interlayer interactions are likely to induce a more graphite-like behavior rather than a graphene-like behavior. A recent study analyzed the interwall interactions through D-band imaging with TERs (Kato et al., 2020). It was experimentally confirmed that the D band is strongly correlated to the number of walls and was theoretically interpreted to the origin of this correlation. The D band in SWCNT was proposed to originate only from the defects while in MWCNTs it is related to structural defects and interwall interactions.

Chaunchiayakul et al. conducted a nanoscale analysis of an individual MWCNT focused on the relationship between the number of walls and the intensity ratio of 2D and G bands based on TERs. The number of walls in MWCNTs is found to be strongly related to the ratio of 2D intensity and G intensity; it is also found that 2D band intensity increases with the interaction between two CNTs (Chaunchaiyakul et al., 2016). To date, no studies on the domain like structure in Raman imaging in CNT have been obtained, but two studies on graphene nanoscale size domain and domain boundaries were conducted using Raman spectroscopy. TERS with a spatial resolution of 0.7 nm were used to observe and study nanometer-scale domains down to 5 nm in graphene (Balois et al., 2019). The effect of domain boundaries of mechanically strained graphene was investigated by confocal Raman spectroscopy. It was found that the strain induced by the presence of domain boundaries causes a G band shift (Bissett et al., 2012).

3.4.2 TERS on individual MWCNTs

CNT samples (obtained from our collaborators at University of Pittsburgh, Pennsylvania) were grown in a custom-designed multizone rapid thermal CVD reactor with the ability to decouple the catalyst temperature and growth temperature (Lee et al., 2019). A silicon wafer coated with 300 nm silicon dioxide was used as the substrate. Alumina and iron were deposited on the substrate surface to grow CNT. The customized CVD reactor offers the ability to study the effect of the growth temperature separately. Figure 3.8 (a) – (d) shows SEM images of CNT forests grown separately under growth temperatures (T_g) of 550 ℃, 600 ℃, 650 ℃, and 750 ℃, respectively. All four batches were grown under the same catalyst temperature (Tc) at 720 ℃. The height and the density of different batches of CNT forests are summarized in Table 3.1. SEM images provide visual information about the density and the overall alignment of the grown CNT forests; however, to obtain more structural information for the CNTs, such as diameter, the wall

number, and quality, we performed TEM measurements. A sharp blade was used to remove the CNT forests grown on a substrate. The CNTs were suspended in DMF solvent at a density of 10 µg/ml. Then the CNTs were sonicated for 30 min while keeping the temperature under 35 ℃. Next, 5 µl of the dispersion was drop casted on a copper TEM grid with lacey carbon support (product # 01894, from Ted Pella) and allowed it to dry in air. Figure 3.8 (e) – (h) shows TEM images of representative CNTs grown at Ts 550 ℃, 600 ℃, 650 ℃, and 750 ℃, respectively. Overall, all 4 batches of CNTs showed diameters of approximately 10 nm. However, more work is needed to relate the growth temperatures with their properties. TERS, on other hand, is not only a more economical method of obtaining images for a large set of samples, but also it can provide additional information about molecular vibrations.

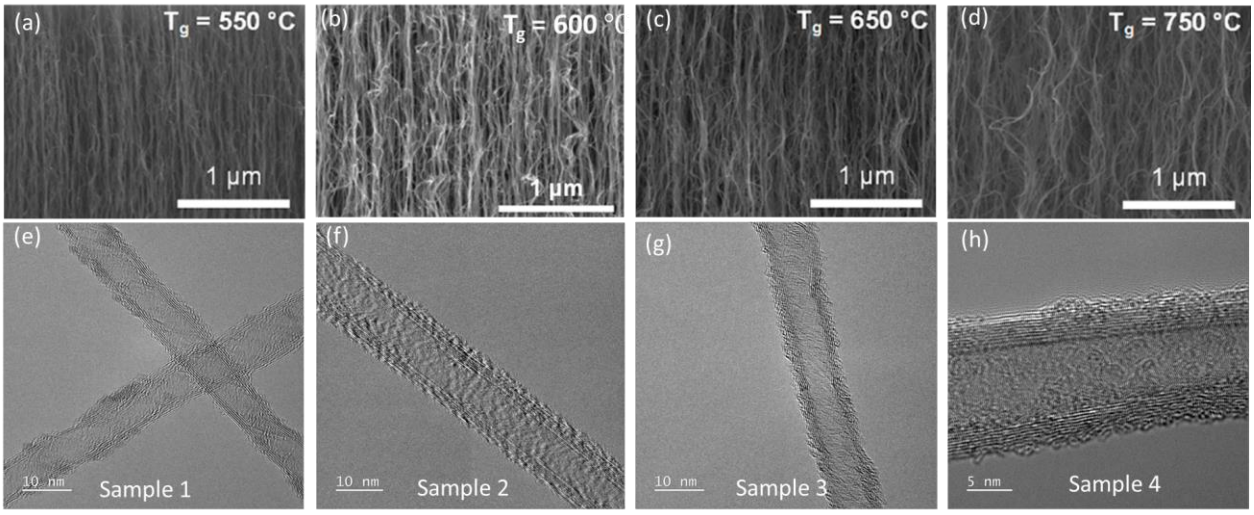

Figure 3.8. SEM images of CNT samples with different growth temperatures. (a)-(d) are from (Lee et al., 2019).

Table 3.1. Properties of CNT samples for different growth temperatures.

Growth T_g	Batch	Height (mm)	Density (g/cm^3)
600	1	0.362	0.032483
650	2	1.467	0.006196

700	3	0.351	0.006702
720	4	0.418	0.009801

TERS, a technique that combines AFM and Raman spectroscopy, was used to characterize individual MWCNTs with different CVD growth temperatures. This technique can obtain topological information on CNTs and simultaneously map each individual Raman peak at any spatial location on a single nanotube. Combining the spatial resolution of AFM, the chemical information from Raman spectroscopy, and single molecule sensitivity due to high enhancement factors from the novel tip, the spectral resolution of this method can reach as low as 8 nm. Figure 3.9 shows the TERS mapping image of a MWCNT showing different Raman bands and spatial information of tubes from sample 1, which has a growth temperature of 600 degrees. Figure 3.9 (d) shows a topographic atomic force microscopy (AFM) image of the MWCNTs in a 1.5×1.5 μm^2 square area (638 nm excitation laser). The step size of the AFM image was about 8 nm, and the scan rate was 1 Hz. AFM data were analyzed by AIST-NT SPM control software.

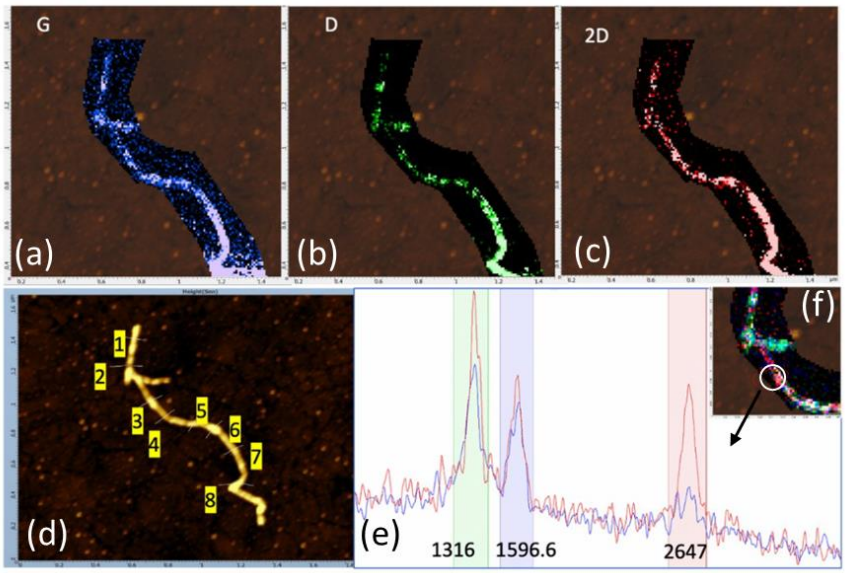

Figure 3.9. TERs mapping image of CNTs (sample 1) with Raman peaks chosen at different points on the same nanotube.

Figure 3.9 (a) – (c) show confocal Raman images of the same CNT, constructed by the intensity of the G-band, D-band, and 2D band. Clearly the G-band, D-band, and 2D-band intensities of MWCNT were observed along the length of the tube, although there is significant variation observed that is otherwise not possible to characterize the individual tubes even with high resolution TEM. This indicates that all these three bands are related to MWCNT structural properties, even though D peak and 2D peak are commonly used to identify defects. Meanwhile, when the difference between Figure 3.9 (a) and (b) is compared, variation in defects or disorders along MWCNT length can be identified from the variation in the dark regions shown in the figure. Figure 3.9 (e) shows two typical CNT Raman spectrum, which were taken from two on TERS image shown in Figure 3.9 (f). Figure 3.9 clearly indicates that TERS mapping has the capability to map out each Raman band in a pixel-to-pixel spatial resolution.

In the carbon family, the G peak (~ 1590 cm^{-1}) is a result of in-plane vibrations of SP^2 bonded carbon atoms. This band corresponds to the tangential vibrations of the graphitic carbon atoms. For MWCNTs, the G band shows a broad peak due to consolidation of super-positioning of the constituent tubes (Kato et al., 2020). The D peak (~ 1350 cm^{-1}) is due to out-of-plane vibrations attributed to the presence of structural defects. In MWCNTs, D peak is an indication of defects present in carbon nanotubes, carbonaceous impurities with sp^3 bonds or sp^2 broken bonds on the walls of the nanotubes, indicating that the nanotubes can have many degree of disorder (Yano et al., 2013). The D-band mode involves stretching and bending of C-C bonds. 2D peak (~2700 cm^{-1}) is assigned to a second-order two-phonon scattering process, and considered as a second order harmonic G band, also known as an overtone or second-order harmonic of the D mode, it happens as an inter-band process. 2D peak is sensitive to increasing defect density, but not as significantly as the first-order mode. The 2D peak could be used as an indication of the

number of graphene layers in multi-layer AB-stacked graphene (L. M. Malard et al., 2009) (Graf et al., 2007).

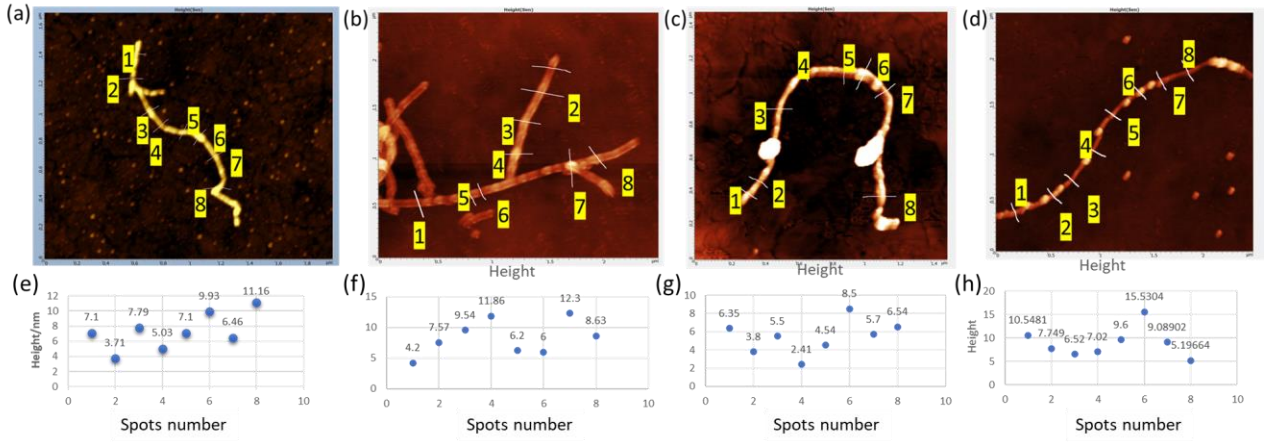

Figure 3.10 TERS mappings of the MWCNTs (upper row), (a) - (d) show 8 spots chosen on each tube, each spot is marked at a white line drawn normal to the tube length. (e) – (h) are the CNT heights at specific spots marked in (a) – (d), respectively.

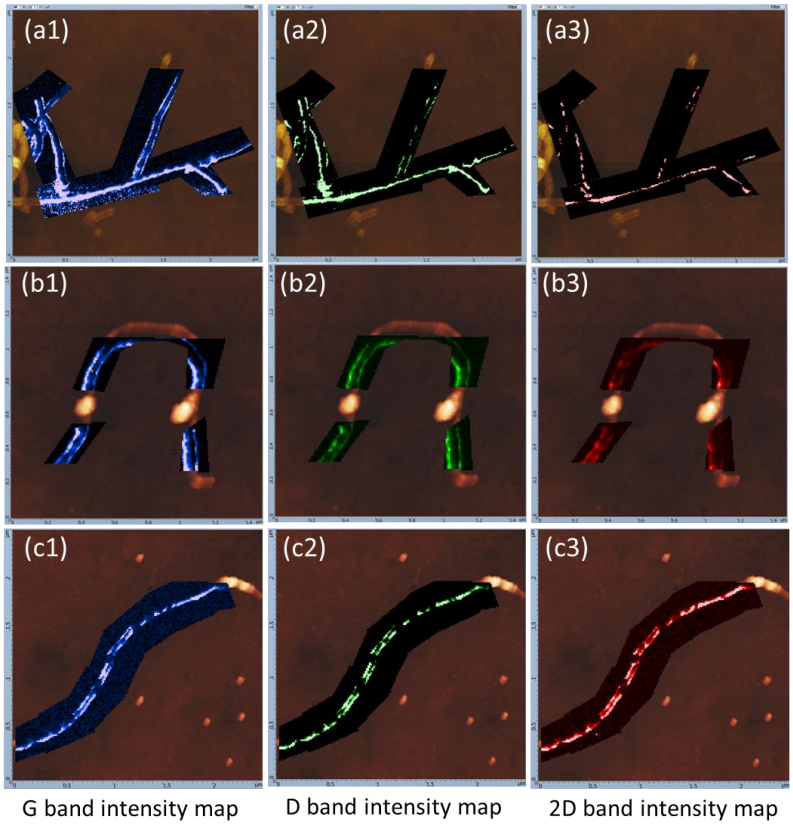

Figure 3.11 (a)-(c) show TERS mapping of Raman bands for sample batches 2, 3, and 4, respectively.

Fig. 3.10 shows the TERS imaging on MWCNTs performed on individual tubes taken from four batches of samples grown at different CVD growth temperatures described earlier. For each MWCNT, eight spots were chosen along each MWCNT, marked by a white line normal to the tube length. For each spot, its height along the white line was measured and the intensities of the three main Raman bands of the MWCNTs (G band, D band, and 2D band) were obtained. A typical example of the Raman bands images is shown in Figure 3.9 (a) - (c) for batch 1. Figure 3.11 (a)-(c) are TERs mapping of Raman bands for batch 2-4, respectively. The images in the left column are G band intensity maps for certain MWCNTs from batch 2-4, while the images in the middle column and right column are intensity maps for D band and 2D band, respectively. Similar to Figure 3.9, mapping of different Raman bands indicated that all these three Raman bands are related to MWCNT structural properties, while each band may indicate different properties, for example, carbon atom disorder or structural defects.

Figure 3.12 (a)-(d) shows the three major Raman peak intensities and their changes with the CNT height, length, etc. as obtained from the spectra taken at the eight locations chosen earlier. For batch 1 and batch 3, the intensity of three major Raman peaks approximately increases with MWCNT's diameter, while for batch 2 and batch 4, there is no relevance between Raman peak intensities and the tube's diameters. This might indicate that the growth temperatures applied on batch 2 and batch 4 were more suitable to grow stable nanotubes. However, the height profile from AFM of CNTs in batch 2 and batch 4 were not very accurate because they were taken near a large chunk of tubes, and measurements on more tubes are needed to justify it. All the Raman peaks intensities were averaged and plotted out in Figure 3.12 (e). Batch 3 has the highest D peak intensity, which suggests batch 3 has more defects than the other batches. The ratios between 2D band intensity and G band were found to be positively correlated to the layer numbers of the tubes.

Batch 3 has the lowest ratio between 2D and G peak, which means batch 3 has the least number of walls.

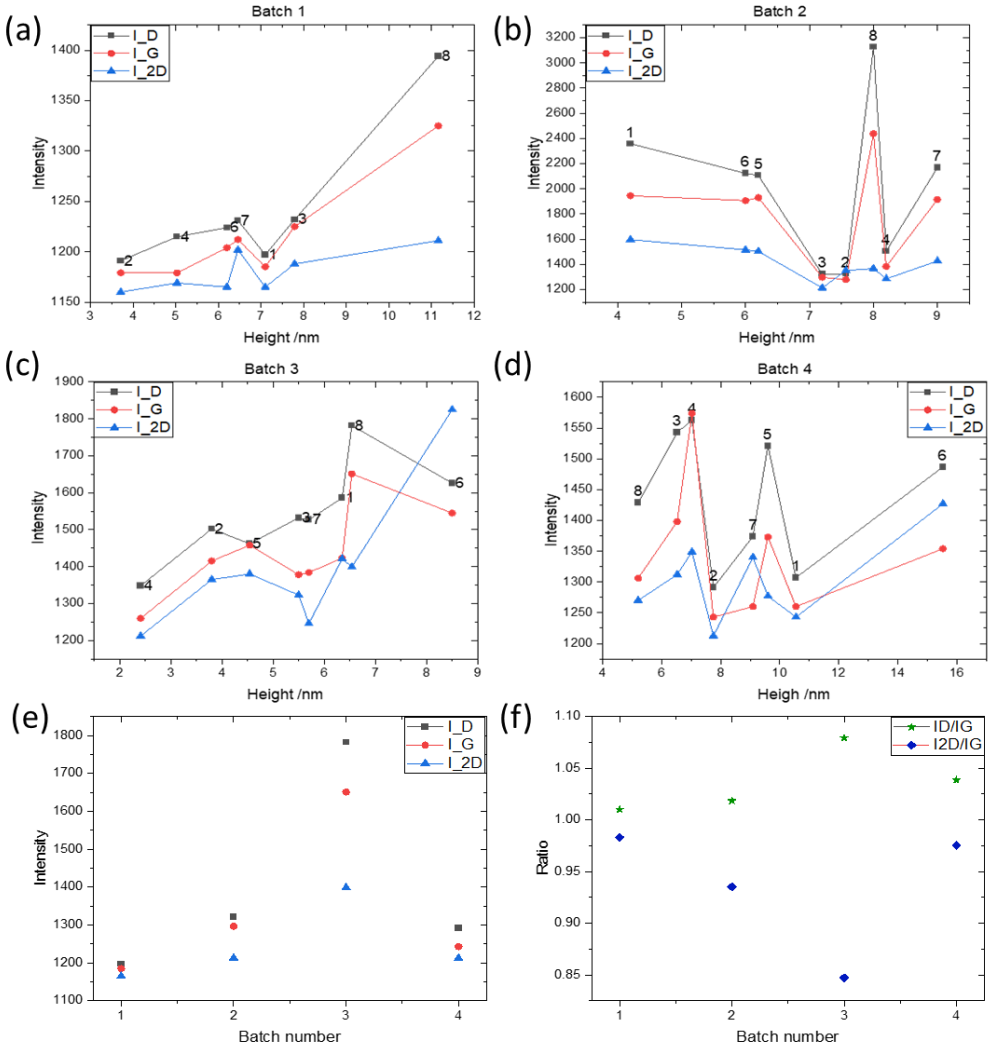

Figure 3.12. (a) - (d) The intensity of D, G and 2D for four batches, respectively; (e) The averaged intensity of D, G and 2D peaks for different batches. (f) The ratio of D peak over G peak, and the ratio of 2D peak over G peak for different batches.

This agrees with the fact that the average diameter from the height profile of batch 3 is the smallest among the four batches. Batch 1 has the smallest D peak intensity and highest ratio between 2D and G peak, suggesting a lower growth temperature will help to reduce the defects of the carbon nanotubes and to obtain a large diameter nanotube. From batch 1 to batch 3, with increasing growth

temperatures, the ratio between the D peak and G peak increases, while the ratio between 2D and G peak decreases, which suggests high growth temperature will increase the defect or disorder density and decrease the number of walls. However, for batch 4, when growth temperature gets higher, the ratio between the D peak and G peak again decreases, while the ratio between 2D and G peak increases, compared with batch 3. This might because a high temperature can help to anneal the tubes and make their structure more organized and less defect. This finding could help to provide knowledge for the study of the growth of MWCNTs as well as single-tube defect engineering. Another interesting phenomenon observed was the TERs image showing a sub-micro domain of Raman peaks, as shown in Figure 3.13 (right side); this may indicate an effortless method to distinguish between structural or electronic properties. A note that needs to be made here is for each batch of samples, only one carbon nanotube was chosen and measured, due to the measurement time was limited. More information about the properties of carbon nanotubes could be obtained, like microdomain, the interaction between walls, and structural transitions. It requires more measurements from each batch of samples and a related statistical analysis.

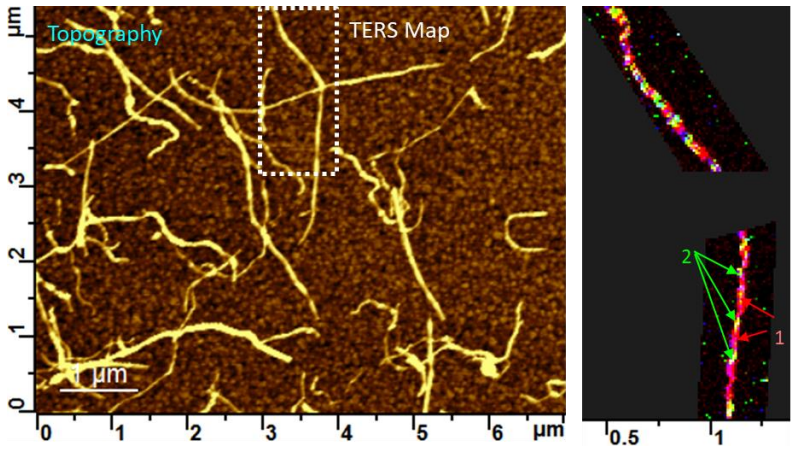

Figure 3.13 (a) Topography image of MWCNTs from batch 4. (b) TERS map (intensity of the 2D band) overlaid on the physical tube dimension from the dotted enclosure shown in (a).

Chapter 4 - Ultrafast Laser – CNT Interaction and GNR Manufacturing

Since the emergence of ultrafast lasers (UFLs), the interaction between light and materials has attracted widespread interest because of fundamental understanding and applicability to a variety of materials, from metal to semiconductor to insulators. UFLs also have the potential to be used in applications in numerous fields, such as ultrafast melting and ablation (Chichkov et al., 1996; Rousse et al., 2001), fabricating waveguides (Streltsov & Borrelli, 2002), material ablation (Chichkov et al., 1996), and creating functional surface nanostructures to name few (Ertekin et al., 2012; Her et al., 1998; Vorobyev & Guo, 2013; Wu et al., 2001). A UFL refers to a laser with a pulse duration from femtosecond (10^{-15}) to picosecond (10^{-12} s), typically shorter than the duration of carrier relaxation processes in materials, including the energy transfer process between electrons and lattice, heat diffusion processes, and the hydrodynamic motion of electrons and atoms. Compared with nanosecond lasers and even longer pulsed lasers, UFLs have higher laser intensity and provide more tunability when treating various materials of interest.

This chapter is organized as follows: section 4.1 provides an overview of several types of processes and mechanisms involved when a UFL interacts with a solid, including absorption, ablation, plasma formation, and plasmonics. Section 4.2 focuses on the interaction between the UFL and CNTs and the transition of CNTs into GNRs. This section includes the experimental details and the development of a finite element modeling to simulate the heat induced to the CNTs by the UFL. The context of this section is based on the study (Chen et al., 2020) published by the author. Section 4.3 provides the chapter summary.

4.1 Interaction between UFLs and materials

Some UFLs, such as femtosecond lasers, operate with laser pulses on a timescale of a millionth of a billionth of a second. Comparing a femtosecond to a second is equivalent to a second compared to 30 million years. Given this timescale, a femtosecond laser pulse is short enough to observe the motions of atoms or even electrons in materials that leads to design materials to manipulate the properties of the materials.

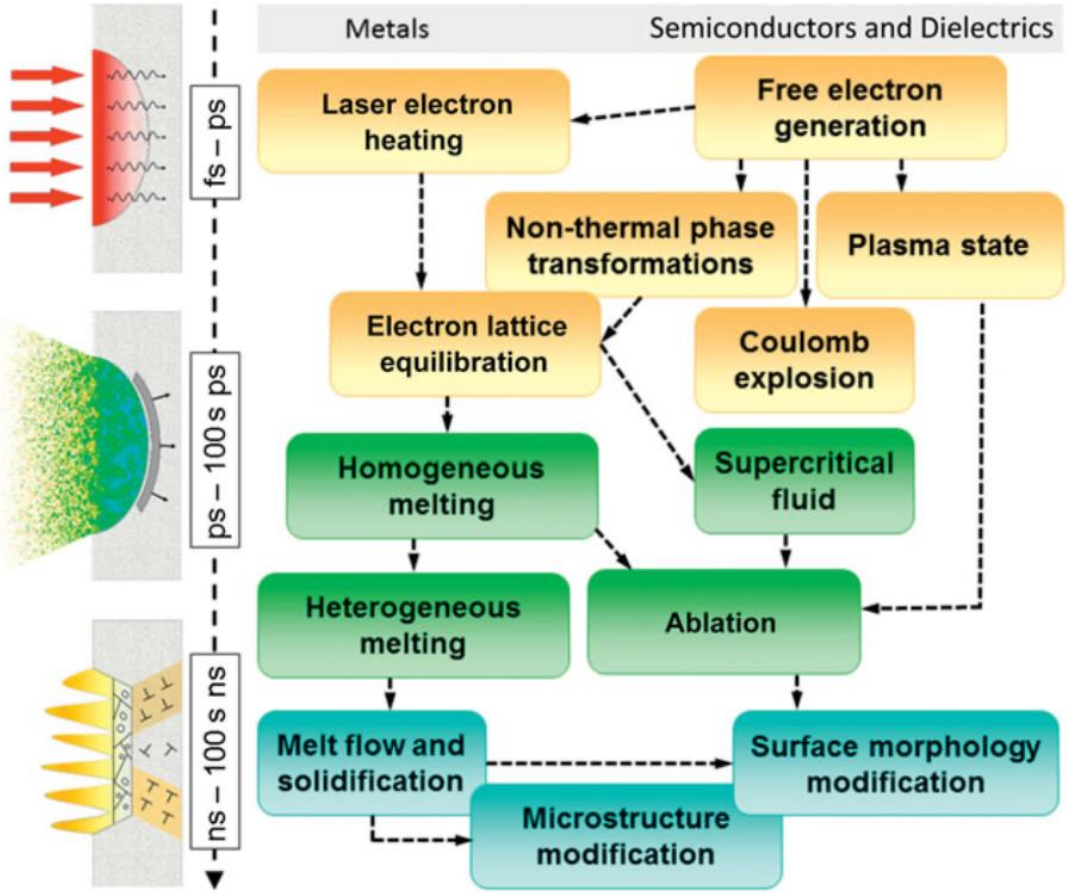

Figure 4.1. Typical timescales of energy dissipation and phase transformation phenomena during and after irradiation of a solid with an ultrashort laser pulse (Shugaev et al., 2016).

Figure 4.1 shows the typical timescales of energy dissipation and phase transformation phenomena during and after the irradiation of a solid with an ultrashort laser pulse (Shugaev et al., 2016). In the figure, the yellow-colored processes indicate electronic excitation and heating, which

occurs immediately after irradiating the ultrafast laser pulse on the material, in a time range of femtoseconds. After the laser pulses, the electrons-lattice heat transfer occurs, also known as rapid non-equilibrium phase transformations; this process occurs in the picosecond time range. The green-colored processes include lattice relaxation to reach homogeneous melting which takes up to a few hundred picoseconds, whereas the timescale of ablation occurs in the nanosecond time range. The last stage of this interaction process, shown in turquoise-colored boxes, is the cooling and solidification of the irradiated area which takes up to a few hundred nanoseconds.

The UFL-matter interaction is a complex process that involves multiple physical mechanisms. According to the order in which the steps occur, the process can be divided into three steps: absorption, generation of plasma, and ablation. Here, absorption refers to material absorbing photon energy, which is the first step in laser-matter interaction. Compared with atoms, electrons are lightweight and are thus much easier to be excited or removed. Depending on the laser energy and the material types, three major mechanisms might occur: intraband absorption, interband absorption, and non-collision absorption. After absorbing the laser energy, the electrons are equipped with high energy and will need to dissipate the energy to other electrons, to the lattice, or space. When the laser energy is low and the material is metal, intraband absorption is dominant because the number of free electrons in the metal is sufficient to absorb the photon energy. In contrast, when the laser energy is higher and irradiates on a semiconductor surface, interband absorption is dominant because there are insufficient free electrons. Ablation is the phenomenon of laser removing the material after absorption, and the ablation can be thermal or non-thermal.

4.2 Laser-unzipping CNTs

The goal of this work is to nanoscale engineer the CNTs using UFL-CNT interactions to manufacture the GNRs. A manufacturing technique was developed by laser unzipping CNTs to

address the issues associated with currently available technologies for fabricating GNRs. The optical and electronic properties, surface topography, and molecular vibrational properties of manufactured low-dimensional nanomaterials are evaluated in this work. By utilizing high electromagnetic-field interaction with CNTs, achieved by UFL exposure, a successful demonstration of the nanomachining of CNTs and their transformation to GNRs and carbon nanocrystal hybrids was established. The ribbons are narrow (typically less than 15–20 nm in width or even smaller depending on tube diameter), while the nanocrystals showing well-defined crystalline structures are embedded along the length of the ribbons from approximately 15 nm down to 3 nm in size. While the nanotubes are metallic in their electronic properties initially, the light-matter interaction was shown to transform them to semiconducting and/or insulating phase, potentially enabling their use in several applications such as nanoscale devices for sensing and electronics. The processes of using coherent and high-field electromagnetic radiation for laser-induced nanomachining (LINM) and laser-induced phase-transformation are scalable, spatially controllable, and operated at room temperature, thus making them suitable for numerous industrial applications of CNTs and related systems.

4.2.1 Experimental setup

A femtosecond laser system, called *Kansas Light Source (KLS)* (presently located at the JRM laboratory in the Physics Department at Kansas State University), was used as the primary UFL source but an alternative UFL, called the HITS, was also available for the design of the experiments. KLS is a titanium-sapphire laser system that produces tunable intensity laser pulses of 35 femtoseconds in pulse duration, or the full width at half maximum (FWHM) of the intensity. It generates the pulses using the principle of chirped pulse amplification (CPA), with a central wavelength of 790 nm and a repetition rate of 1 kHz. Figure 4.2 shows the schematic representation

of the experimental setup. In this experiment, the laser beam, which is linearly polarized, was focused onto the sample/substrate, with a pulse energy of 1.8 mJ. Before the laser treatment, the sample containing CNT network, had a random distribution of tubes spread on a patterned silicon chip. The sample was placed on a 3D motorized translation stage in ambient air. The size of the chip containing the nanotubes was much larger than the laser spot size, so the 3D translation stage was programmed to move the sample in the XY direction (stage speed = 0.1 mm/s) to ensure all the nanotubes were treated with laser radiation. Minimal overlapping of spot area was calibrated while moving the stage back and forth. The laser fluence was varied from 0.1 to 2 J/cm^2; by using a lens with a focal length of 50 cm, leading to achieve a large laser spot size with a diameter of 270 µm and a laser fluence of 2 J/cm^2. A schematic diagram of the laser irradiation setup is provided in Figure 4.3 , which shows the sample surface as normal to the incident radiation. A laser pulse treatment time of 2 seconds per laser spot was considered, resulting in approximately 2,000 laser pulses being received by individual MWCNTs.

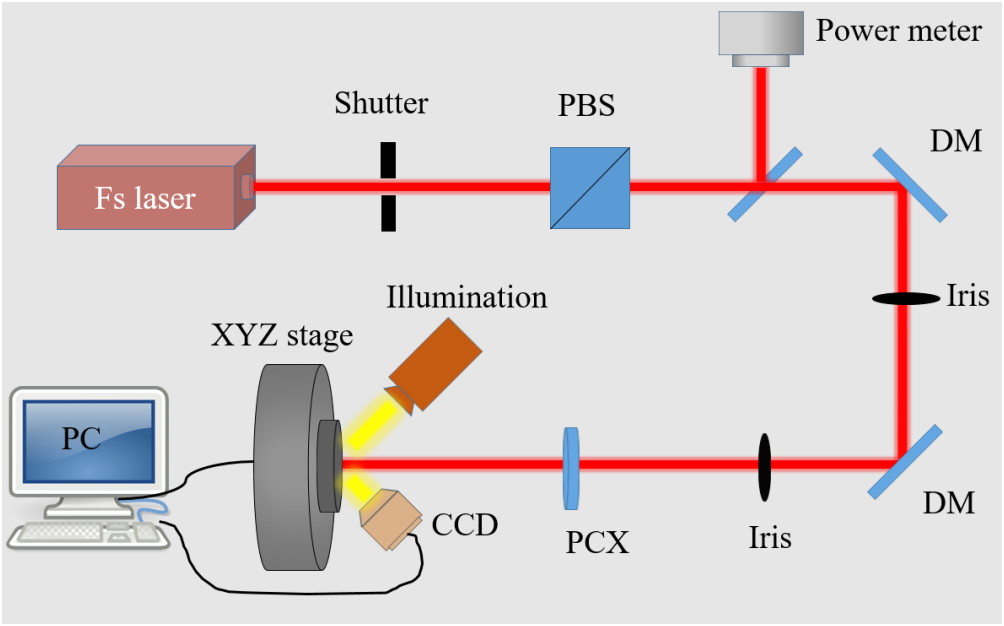

Figure 4.2. UFL irradiation experimental setup.

The laser irradiation experiment was performed according to the following procedure:

1) Optically align the laser system and collimate the laser beam.
2) Place the sample on the 3D motorized translation stage.
3) Move the stage such that the laser spot falls at a specified point on the sample (typically one edge). Place the sample 3 cm away from the focal spot along the collimated beam.
4) Align the laser to ensure that the sample plane is vertical to the laser beam propagation direction. This alignment is performed by using the beam at low power and monitoring its position at different locations along the optical path.
5) Shine the laser beam (at a low power setting) at the centers of the four large alignment markers at the four corners of the chip (these are the reference points on the chip that are used to determine the extent of the stage movement required to scan the whole sample).
6) Estimate the laser beam diameter to determine the pitch size used for laser scanning. This is accomplished using carbon tape affixed to a metal disk and inserting it onto the laser path at the point of interest along the optical path.
7) Program the 3D translation stage to ensure the laser beam moves along the substrate surface uniformly and covers the whole surface.
8) Set the velocity of the stage at 100 μm/s to ensure the laser beam to irradiate over the whole substrate area.
9) Conduct a series of experiments with varying laser fluence values. The detailed parameters are listed in the table shown in Figure 4.5 (b).

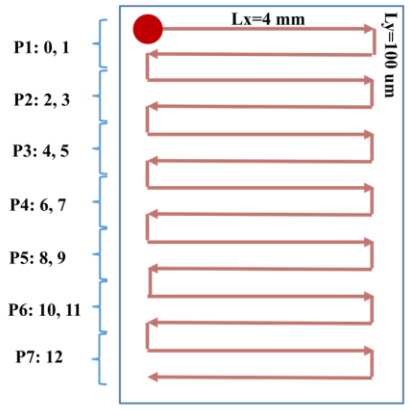

No.	Markers areas	Laser fluence (J/cm^2)	Average power (W)	Beam diameter (cm)
P1	0, 1	0.1	0.057	0.027
P2	2, 3	0.15	0.085	0.027
P3	4, 5	0.2	0.114	0.027
P4	6, 7	0.25	0.143	0.027
P5	8, 9	0.3	0.171	0.027
P6	10, 11	0.27	0.154	0.027
P7	12	0.26	0.149	0.027

Figure 4.3. (a) Laser beam scanning path; (b) laser beam parameters.

4.2.2 Sample preparations and Microscopy Studies

The following steps were involved in the MWCNT sample preparation for electron microscopy and AFM. To begin, MWCNTs were purchased from NanoIntegris Inc. (catalog #MW30-141). The outer diameters of most of the tubes were varied from 10 nm to 20 nm, the inner diameter was approximately 4 nm, and the length of the tubes was varied from 1 µm to 12 µm. SEM images (Figure 4.4 (a) and (b)) and TEM images (Figure 4.4 (c) and (d)) of the original MWCNTs were taken and the average diameter of the MWCNTs was between 10 nm and 20 nm. Additionally, the number of walls (equivalent to the number of rolled graphene sheets) present in the MWCNTs were counted from the TEM images. These observations were consistent with the predicted nanotube's outer diameter. For example, for the tube shown in Figure 4.4 (d) (a nanotube with 10 graphene-like layers), then with a ~ 4 nm inner wall diameter, the outer diameter of the tube is approximated by $d_{out}(nm) = 4\,nm + (2 * 9 * 0.34)\,nm + (2 * 10 * 0.32)\,nm = 16.52\,nm$. The gap between each wall is 0.34 nm and each wall thickness is 0.32 nm (Cai et al., 2009), and the interlayer distance is 0.34 nm in a CNT (Palser, 1999). The image in Figure 4.2 (d) shows a similar outer tube diameter.

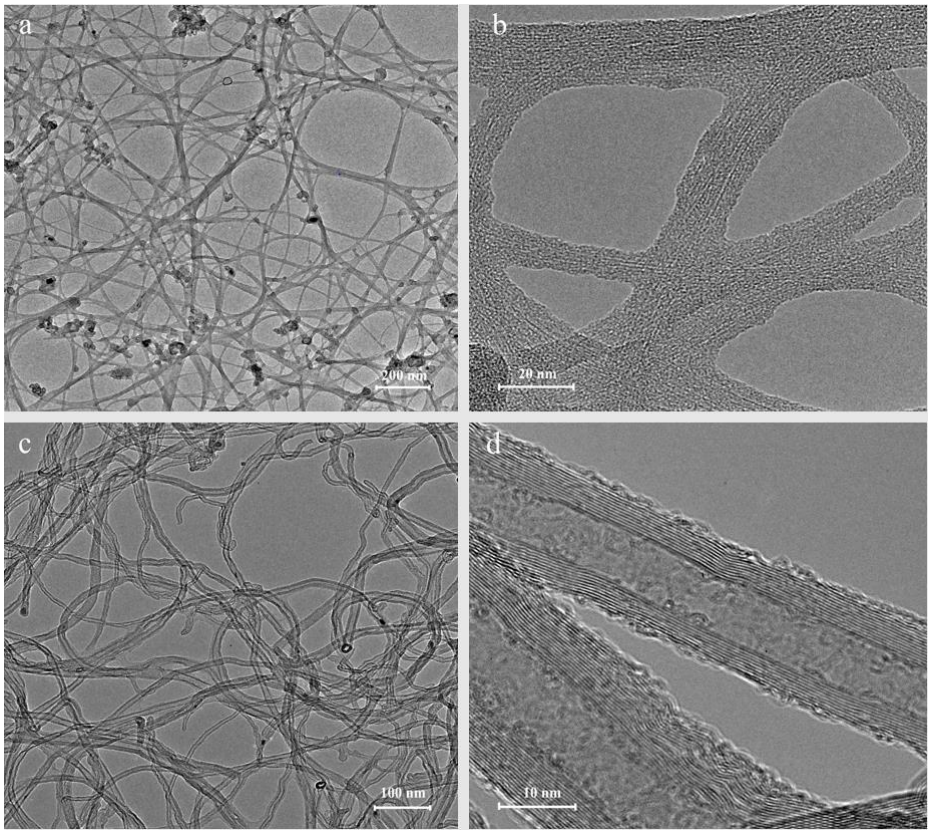

Figure 4.4. (a) & (b) SEM images of starting (untreated) MWCNT; (c) & (d) TEM images of untreated MWCNT.

The most critical requirement for the formation of the nanoribbons and nano-diamond embedded nanoribbons is to first make a clean suspension of the nanotubes in an organic solvent (explained below) by dispersing well inside the fluid. Once this is achieved, the nanotube concentration in the solution can be altered by diluting the suspension with a parent solvent; the solution can then be drop-cast onto the chip (as previously discussed). In our experiment, we used the organic solvent DMF (from Sigma-Aldrich, USA). Samples were prepared according to the following procedure:

1) Dissolve 0.4 mg MWCNT powder into 20 mL DMF in a vial, and double dilute the solution. The density of the MWCNT/DMF solution should be 10 mg/L.
2) Place the vial with the solution in an ultrasonic vibrator for one hour. The water temperature

will rise upon sonification. Avoid the temperature rising to above 40 °C; if it does, allow a few minutes to cool down or reduce the ultrasonic power.

3) Leave the solution overnight.
4) Use a pipette to gently pull 10 µL of the supernatant solution and drop it on the chip. Prior to the solution being dropped, the chip was cleaned by sonicating and rinsing with acetone (5 min), isopropyl alcohol (5 min), and methanol (5 min.). Finally, the chip was dried on a hotplate set at 50 °C for 5 min).
5) Let the sample dry for at least 6 hours in the air.
6) Place the sample on a hotplate set at 65 °C for 5 min.
7) Remove the DMF solvent following this procedure: a) soak the sample (MWCNTs on the chip) in toluene for 30 min at room temperature; b) remove it and soak in acetone for 30 min at 65 °C; c) soak the sample for a final time in methanol for 30 min at 65 °C; d) remove the sample and let it dry in air.
8) Place the sample on a hotplate set at 65 °C for 5 min.

The chip used in the project was specially made with markers of coordinates of locations, as shown in Figure 4.5 (a). This is critical because CNTs and GNRs are hard to locate under an AFM; since the maximum scanning area of AFM is 11 µm, it is important to know the location of the samples at the start of the AFM imaging. Optical microscope images of the tubes with respect to their relative location to the alignment markers can help locate an individual nanotube. AFM imaging, SEM imaging, and HRTEM imaging were systematically performed to monitor the nanoscale structural changes and nanotube/nanoribbon to nano-diamond crystal phase formation as a result of intense light interaction with the nanotubes. To closely monitor these events, we performed the above experiments side-by-side, with one set of measurements without laser

irradiation and a second set with laser irradiation. Figure 4.5 (d) shows a representative AFM topography with the tube's diameter shown in Figure 4.5 (e). All the images in Figure 4.3 are representative of individual MWCNTs without laser irradiation.

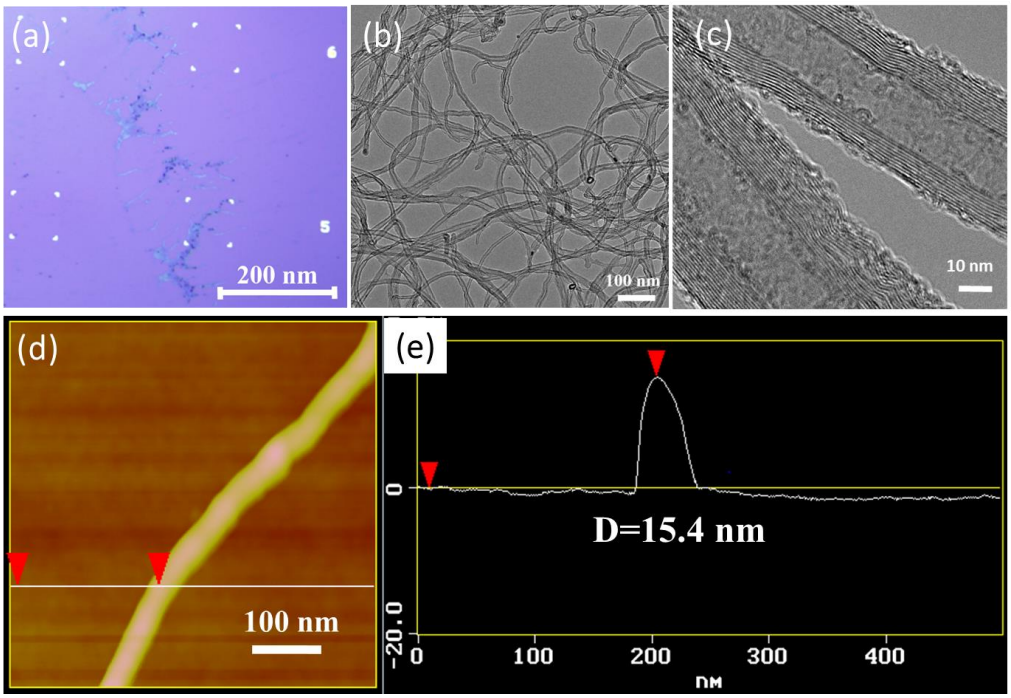

Figure 4.5. (a) Optical microscopy images of the samples before laser treatment; (b) low-resolution TEM image of the CNTs used in this study; (c) high-resolution TEM image of the represented MWCNTs; (d) and (e) atomic force micrograph image and the corresponding height profile of a representative MWCNT with a diameter of 15.4 nm (Chen et al., 2020).

4.2.3 Results and discussion of Laser-MWCNT interaction

The optimized laser conditions for the process were obtained by irradiating the MWCNTs with varied laser intensities, and an optimal fluence of 0.15 J/cm^2 was obtained which was subsequently used to study the interactions with the tubes.

For comparison purposes, fresh MWCNTs were initially examined without laser irradiation; the same measurements were subsequently performed over the same location on the chip after the laser irradiation. Figure 4.6 shows a series of resulting AFM images of the MWCNTs after laser irradiation. As shown in Figure 4.6 (a) and (b), the tube diameter of a nanotube before

the laser radiation was 9.2 nm; after the laser radiation, the height of the same nanotube was 1.9 nm, without a significant change in width. This result provides direct evidence of a nanotube geometry converting to a nanoribbon due to high-field laser-matter interactions. To further verify this effect, we imaged several nanotubes, as shown in Figure 4.6 (c). As can be seen in the figure, the topography of a cluster of MWCNTs changed entirely. To investigate the local geometry, we selected two areas (circled in Figure 4.6 (c)) and measured their local height profiles (Figure 4.6 (d) and Figure 4.6 (e)). The results showed heights of 2.1 nm and 1.8 nm, respectively, with widths comparable to those of the original tubes.

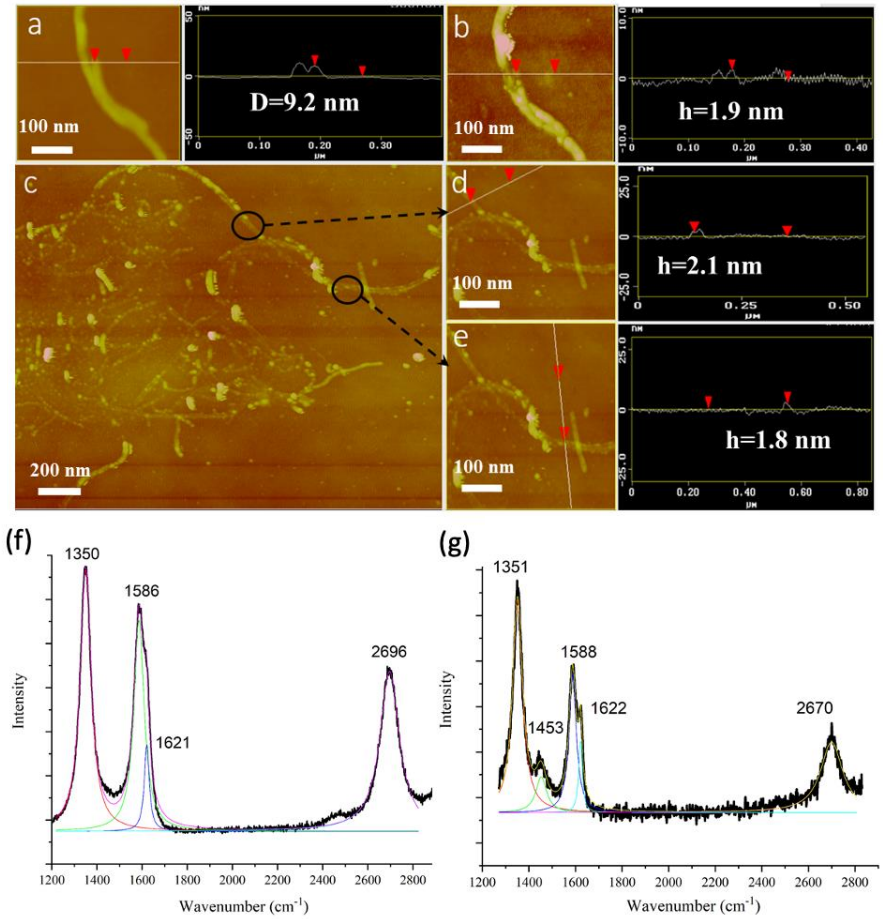

Figure 4.6. AFM image of a nanoribbon cluster formed by femtosecond laser exposure with 0.15 J/cm^2 laser intensity; (a) AFM image of an original tube (diameter 9.2 nm) before laser exposure; (b) AFM image of the same tube after laser exposure (diameter 1.9 nm), indicating ribbon formation; (c) laser exposure on a cluster of nanotubes, converting most of them to nanoribbons;

(d)–(e) two features within the cluster are selected and scanned, showing heights of 2.1 nm and 1.8 nm, respectively. (f) MCNTs Raman spectrum, and (g) carbon/GNR Raman spectrum, probed with a 532 nm excitation source (Chen et al., 2020).

While CNTs are uniquely characterized by their diameters and chirality, in the case of CNRs, they become more complex, due to their widths, thicknesses, and edge states. Raman spectroscopy, a nondestructive measurement technique capable of probing the structural information of the nanomaterial and addressing issues such as metallicity, strain, chirality, etc. of the nanotubes, was carried out on the MWCNTs and nanoribbons. In the Raman spectrum, CNTs (particularly MWCNTs) are characterized by several principal peaks. The peak at ~1585 cm^{-1}, corresponding to C-C bond vibration along the tube direction (axial or tangential direction, with neighboring atoms in opposite phase movement), represents the G peak. The peak at ~ 1348 cm^{-1} corresponds to a defect-induced peak activated by structural defects and/or disorders (D peak). The peak at ~2695 cm^{-1} corresponds to an overtone of the D-peak (two-photon Raman process) and is termed a G' peak or 2D peak. Additionally, although not shown here due to coincidence with a nearby silicon/oxide peak, a fourth peak was also characterized at low frequencies (about 100 to 300 cm^{-1}) that may correspond to the RBM (Delhaes et al., 2006; Lehman et al., 2011). As the CNTs are converted into the CNRs, changes in the above peaks are expected due to their sensitivity to the geometry (Bischoff et al., 2011; Rodriguez et al., 2019). A comparison of the Raman spectra of the MWCNTs and the CNRs is shown in Figure 4.6 (f) and Figure 4.6 (g). Since the Raman spot size (~ 1μm in diameter) is much larger than the width of an individual MWCNT or nanoribbon, the spectra obtained are averaged over multiple CNTs and CNRs present in the cluster discussed previously.

The Raman shift positions are consistent, although with some notable observations. The original MWCNTs possess a high degree of disorder, as evidenced by an FWHM value of the D

peak of 59 cm^{-1}. Although no visible fault lines or structural inconsistencies are observed in the tubes from the HRTEM images, these features could arise from the surface defects and deformations in these long and tortuous tubes. The D-peak remains strong after the laser treatment but with a narrower distribution, with an FWHM value of 51 cm^{-1}. A comparison of the D peaks between the tubes and ribbons shows almost no changes in D-peak positions (1350 cm^{-1} for tubes vs. 1351 cm^{-1} for the ribbons), indicating an absence of enhanced disorder-induced scattering contributions in the nanoribbons. A ratio of D to G peak of more than unity in both the geometries is indicative of a retention of higher structural defects present after the interactions of tubes with the femtosecond pulses. The apparent G-peak for both the tubes and ribbons shows asymmetry and fitting with Lorentzian peaks, which indicates the G peak splitting into a peak with a lower wavenumber or lower energy peak and a higher wavenumber or higher energy peak. The lower energy peak represents the G-peak and the higher energy peak is a characteristic of a defect-induced peak, known as a D' peak, which arises due to intra-valley scattering of electrons by LO phonon in contrast with inter-valley scattering for a D peak involving TO phonon (Ferrari, 2007; L. Malard et al., 2009). The G peak position is close to 1580 cm^{-1} which is similar to that of the graphene G peak (1586 cm^{-1} and 1588 cm^{-1} for MWCNTs and CNRs, respectively); in addition, its FWHM value is similar to that of the graphene G peak (26 cm^{-1} for the tubes and 19 cm^{-1} for the ribbons). The D' peaks are present at 1621 cm^{-1} and 1622 cm^{-1} for MWCNTs and CNRs, respectively, with FWHM values of 56 cm^{-1} for the tubes and 38 cm^{-1} for the ribbons. The asymmetry and splitting observed (with individual fitted peaks described above) in both MWCNTs and nanoribbons are shown in Figure 4.6 (f) and Figure 4.6 (g), respectively. From the ratio of I_D and I_G, it is evident that the defects and disorders increase after the tubes transform into ribbons (I_D/I_G is 1.3 for MWCNTs as opposed to 2.05 for ribbons), but with a narrower distribution. A

peak at 1453 cm^{-1} is visible for the nanoribbons but not the original nanotubes. The peak at this position was previously analyzed by Ren et al. as one of the two bands (the other is at 1530 cm^{-1}) responsible for hydrogen atom-terminated localized vibration of the edge atoms (Ren et al., 2010). Finally, there is a substantial softening of the 2D peak (or G' peak) for the nanoribbons as well as a decrease in the 2D peak intensity. All these changes observed may result from the edge states produced in the nanoribbons and/or the phase transformation (discussed later) of the carbon lattice (some sp^2 carbon converting to sp^3, as discussed previously in the context of Figure 4.6 (h)) due to the incoming heat flux from the laser.

Although the high-field interaction of electromagnetic radiation with the nanotubes leads to the formation of nanoribbons, closer observation of the GNR structure in Figure 4.6 (c) and Figure 4.7 reveals the presence of small dot-like structures along the length of the ribbons. To probe these dots, the HRTEM measurements were carried out in which the nanotubes in solution were directly dispersed on a TEM grid and cleaned; subsequently, the TEM grid with the tubes was laser-treated with the optimized laser power used earlier.

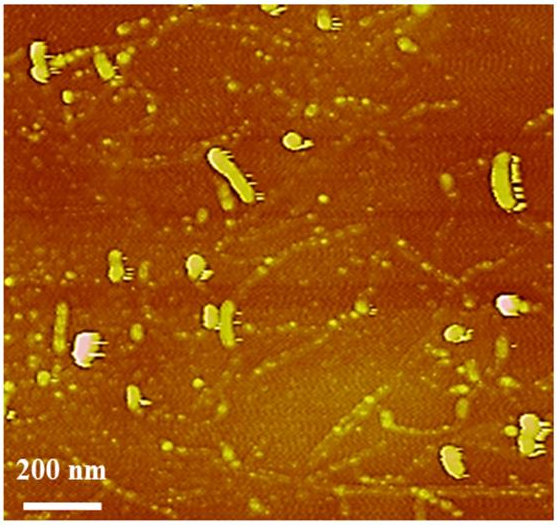

Figure 4.7. AFM images of nanoribbons

In Figure 4.8 (a), TEM images show a cluster of ribbons with an embedded dot-like structure. Many of the GNRs are associated with these high-contrast nanoparticle-type embedded structures. Moreover, Figure 4.8 (b) shows the representative diffraction pattern taken on one of the dots. Figure 4.8 (c) shows an HRTEM image of representative nanoparticles of 3 nm and 5 nm particle size with clear crystallographic orientations/planes. Therefore, the high-contrast dots observed in the TEM images in Figure 4.8 (a) and AFM images in Figure 4.7 are nanocrystals. To further explore their atomic composition, we performed energy dispersive x-ray spectroscopy (EDX) analysis of the same 5 nm nanocrystal in the TEM chamber. Figure 4.8 (b) shows the elemental peaks of carbon, cobalt, iron, copper, and oxygen present in the nanocrystal. These results indicate that the nanocrystals are formed from carbon atoms with the presence of iron and cobalt magnetic impurities arising from the catalyst particles used for the CNT growth and oxygen most likely from atmospheric contamination, particularly during photothermal-induced atmospheric oxidation. The copper signal arises from the TEM grid. Understanding the formation of this crystallographic phase transformation, starting from the sp^2 phase of CNTs to the sp^2 phase of nanoribbons to, finally, the carbon nanocrystals (possibly, the sp^3 phase), is of continued interest.

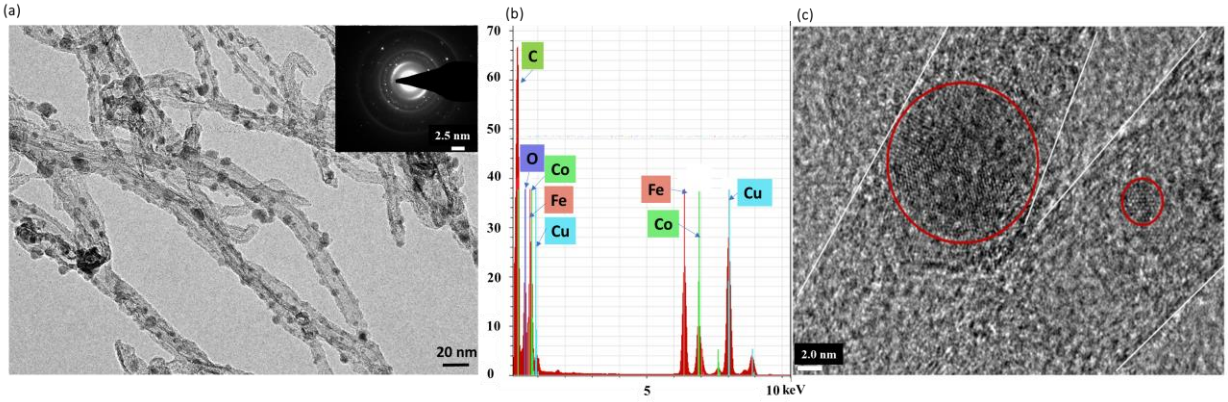

Figure 4.8. (a) TEM image of a cluster of GNR/nanocrystals. The inset image shows the representative diffraction pattern taken on one of the dots; (b) EDX spectrum of the GNR/

nanocrystal hybrid, with peaks of carbon, cobalt, iron, copper, and oxygen visible; (c) HRTEM images of GNRs/nanocrystal hybrids; while the GNR on the left shows a nanocrystal ~12–15 nm in diameter (extending the width of the ribbon), the GNR on the right shows the onset of crystal formation (~3 nm diameter) as the tube/ribbon interacts with high-field laser radiation; the white lines are inserted for guidance to the eye for convenience; the scale bar is 2 nm (Chen et al., 2020).

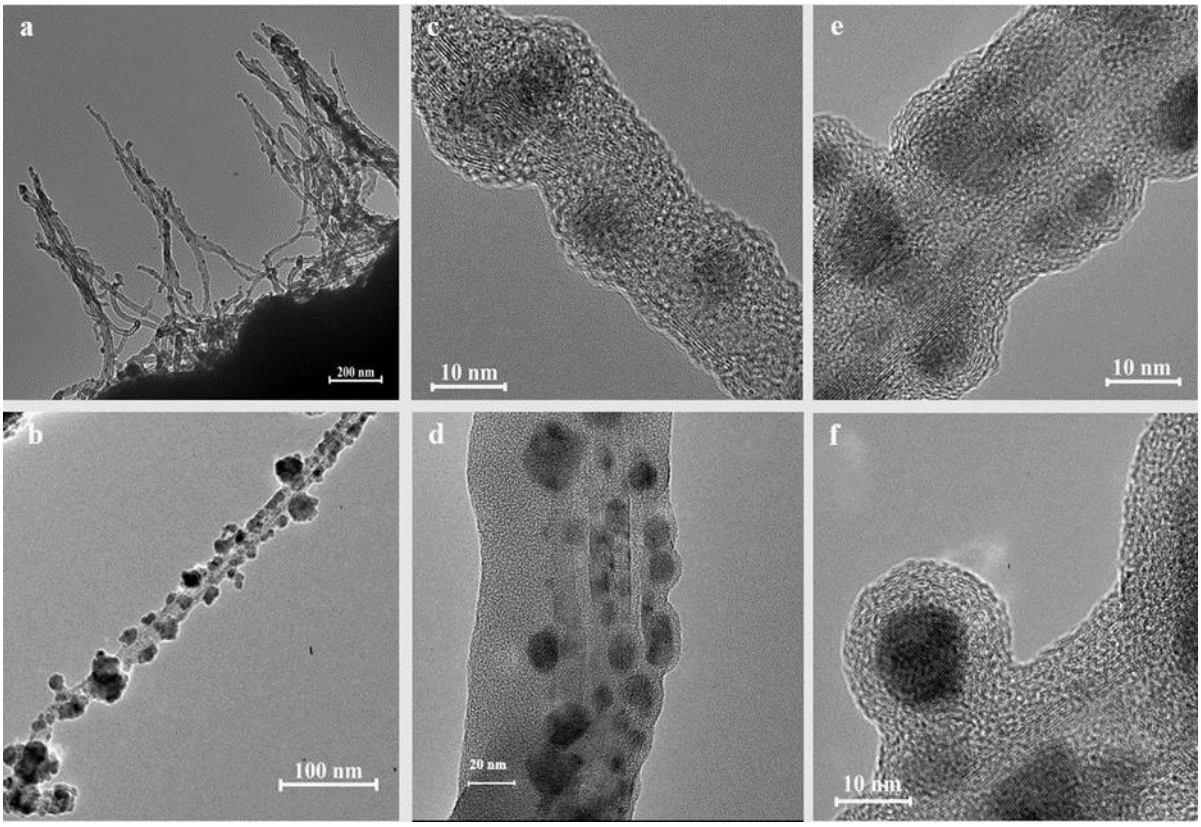

Figure 4.9. (a)–(f) TEM images of nanoscale phase transformation.

Figure 4.9 (a)–(f) provides more evidence with low resolution (the image with some CNRs captured on the edges of the TEM grid) and high-resolution TEM images of the nanocrystals at different stages of their crystallographic formation, such as early-stage formation, and structures with a core-shell type of formation with crystalline core and amorphous shell. The amorphous shells are typical spherical particles of carbon with concentric graphite-type shells, known as '*carbon onions*', which here are evidence of crystallographic transformation of carbon atoms from one phase to the other enabled by the light-matter interaction. Since the light-matter interaction

involves a temperature of thousands of degrees for an extremely short period on the surface of the geometrically confined CNTs, this laser-induced phase-transformation (Rao et al.) process could be exploited for future nanoscale material synthesis. Indeed, studies have reported on carbon nanotube to diamond crystal structure transformation, carbon onion to diamond structure transformation, and a reversible phase transformation between nano-diamond and carbon onion; these transformations could be investigated using laser-nanotube interactions (Sun et al., 2004; Wei et al., 1998; Xiao et al., 2014). The process of using coherent and high-field electromagnetic radiation for LINM and laser-induced phase-transformation (Rao et al.) is scalable, spatially controllable, and is performed at room temperature, making it suitable for numerous industrial applications of CNTs and related systems.

4.2.4 Infrared nanoimaging studies

To determine the physical properties of all the sample regions, we performed systematic infrared nanoimaging studies of our samples with a scattering-type scanning near-field optical microscope (s-SNOM) (Chen et al., 2019; Fei et al., 2011; Hu et al., 2017). The s-SNOM is designed based on an AFM and can measure simultaneously the topography and optical information of the sample with a spatial resolution of approximately 25 nm. The probing laser energy is set to 0.11 eV. With s-SNOM, we measured the amplitude and phase of the complex infrared (IR) near-field signals. With the measured IR signals, the IR optical constants of the measured samples were determined. As shown in Figure 4.10, we plot simultaneously the AFM topography (Figure 4.10 (a)), IR amplitude (Figure 4.10 (b)), and IR phase (Figure 4.10 (c)) of a representative sample region that contains many MWCNTs and laser processed GNRs. We then select three spots (marked ‘P1’, ‘P2’, and ‘P3’ in Figure 4.10 (a)) in the image, where three 1D features are seen. In Figure 4.10 (d)–(f), we plot the line profiles taken perpendicular to these

features. As shown in Figure 4.10 (d), the features at ‘P1’, ‘P2’, and ‘P3’ have heights of approximately 12 nm, 3 nm, and 1 nm, respectively, indicating P1 with nanotube signature, and P2 and P3 with nanoribbon signatures. Their widths are significantly smaller than the linewidths of the AFM peak profiles (marked with a double-sided arrow in Figure 4.10 (d)).

Regarding the IR properties of the three nanotubes and nanoribbons, from the IR images and profiles in Figure 4.10 (b)–(f), we observe a significant signal difference between the nanotube at ‘P1’ and ribbons at ‘P2’ and ‘P3’. Both the IR amplitude and phase of the nanotube at ‘P1’ are higher than those of the SiO_2/Si substrate. In contrast, the ribbons at ‘P2’ and ‘P3’ have a weaker IR amplitude compared to that of SiO_2/Si, with no apparent phase contrast. Using quantitative modeling, we converted the IR amplitude and phase signals to effective infrared permittivity: $\varepsilon_{P1} \approx -6 + 0.6i$, $\varepsilon_{P2} \approx 4.2 + 0.2i$, and $\varepsilon_{P3} \approx 4.2 + 0.2i$. Based on these numbers, we interpreted the nanotube at ‘P1’ to be metallic, which is as expected for an MWCNT. The nanoribbons at ‘P2’ and ‘P3’, on the other hand, were determined to be either insulators or semiconductors with sizable bandgaps. We believe that they are multi-layer nanoribbons (MLNRs) and are generated by LINM of MWCNTs with laser irradiation (discussed in greater detail in the next section and shown in the modeling section). Although the origin of the semiconducting/insulating behavior of these MLNRs is not fully explored in this work, it is possible that laser irradiation, by breaking the material symmetry and introducing unique types of defects into these nanoribbons, causes electron localization, resulting in insulating/semiconducting behavior. It is also possible that edge oxidation occurs during laser irradiation, leading the samples to become partially graphene oxide nanoribbons, as shown in the EDX. Finally, due to the phase transformation from sp^2 to carbon nanocrystals, the latter nanoscale crystals will develop higher and tunable bandgaps.

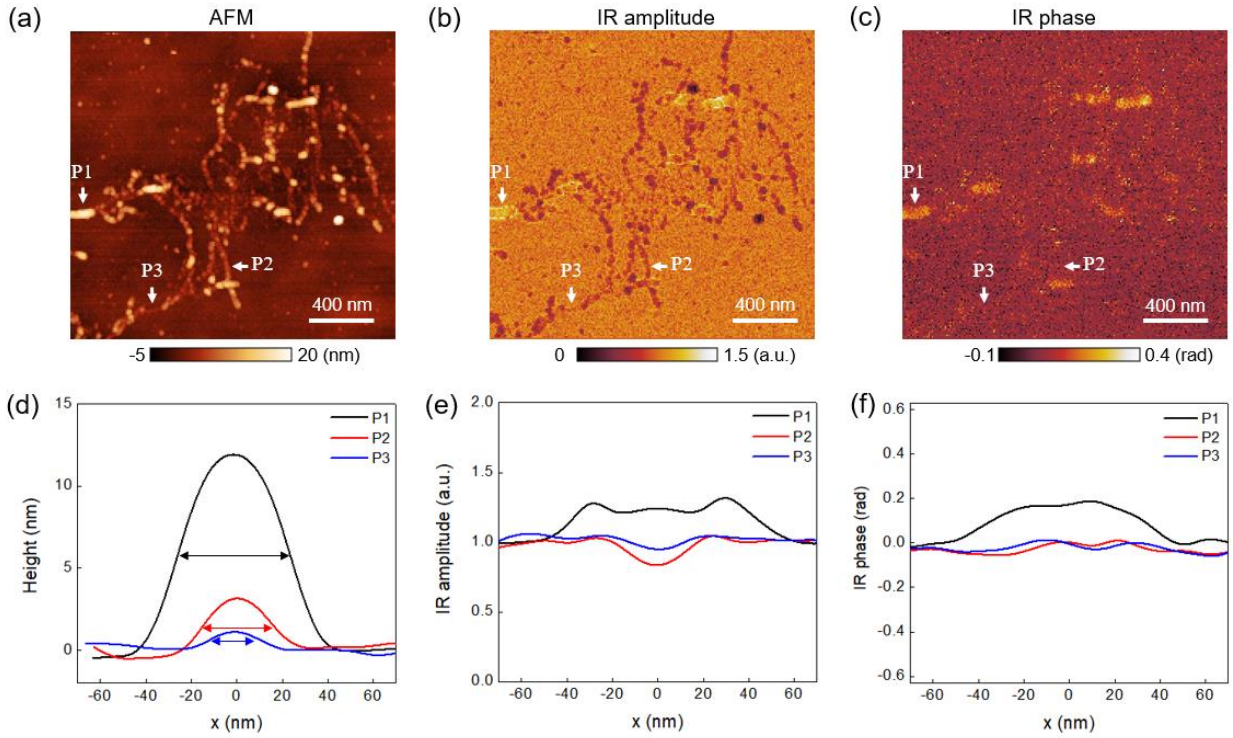

Figure 4.10. Infrared nano-imaging data; (a)–(c) AFM topography, IR amplitude, and IR phase images of a typical sample area, respectively; (d)–(f) topography, IR amplitude, and IR phase line profiles taken perpendicular to the nanowire features at locations ‘P1’, ‘P2’, and ‘P3’; these line profiles were taken perpendicular to the nanowires; the double-sided arrows in (d) mark the linewidths of the three topography peaks (Chen et al., 2020).

4.2.5 Finite element method modeling of heat transfer

4.2.3.1 Governing equations

To understand the conversion of the MWCNTs to GNRs or CNRs, we next modeled the femtosecond laser heating process of MWCNTs and estimated their transient temperature profile during laser irradiation using finite element analysis with COMSOL Multiphysics 5.3. In our model, femtosecond Gaussian laser pulses were applied to the MWCNTs as the heat source (used as heat flux). A laser pulse energy of 2 mJ with 800 nm wavelength and a pulse width of 40 fs were used as input parameters. The range of average laser power used in the experiment was 57–114 mW.

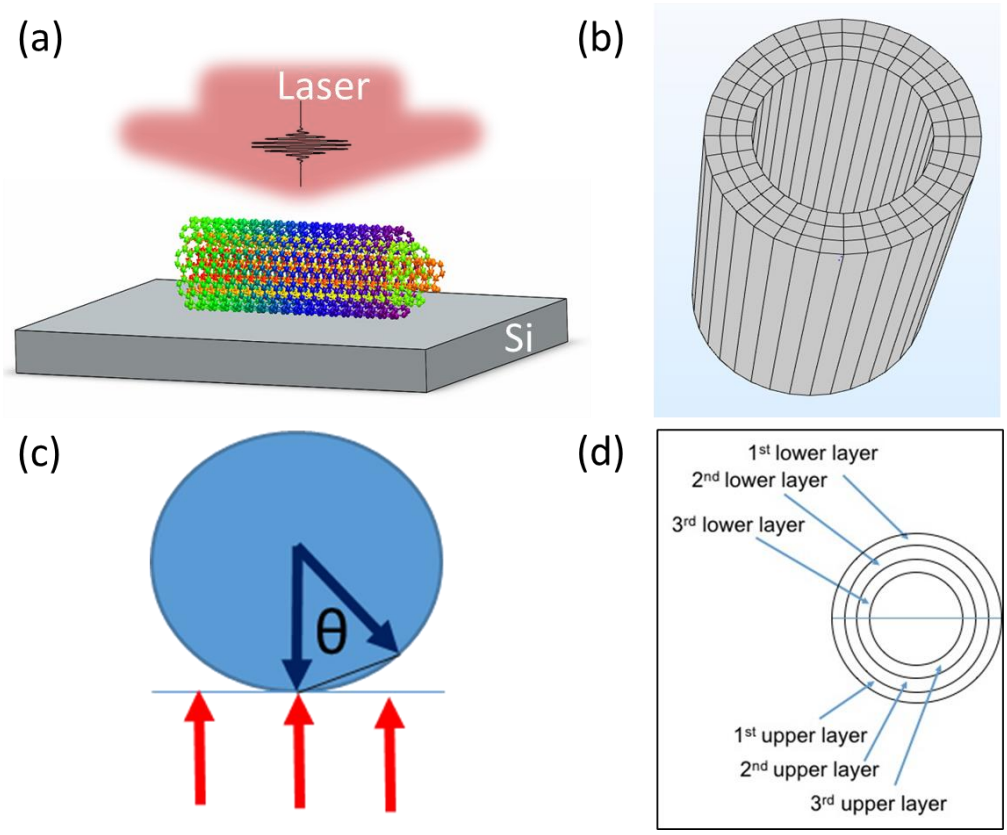

Figure 4.11. Finite element modeling to study the heat transfer processes during femtosecond laser-MWCNT interaction; for simplicity, an MWCNT with three walls is considered; (a) schematic of the laser treating a carbon nanotube; (b) MWCNT treated as a hollow cylinder with layered solid walls; (c) schematic of normal and angular incidence of the laser beam with the nanotube surface; (d) cross-sectional view of the three-walled nanotube; for ease of calculation, the walls are grouped into upper-half and lower-half walls.

The model configuration for the fs laser-MWCNT interaction is shown in Figure 4.11. Figure 4.11 (a) shows the laser irradiation on a single MWCNT (three-walled CNT) kept on a silicon wafer. The MWCNT is treated as a hollow cylinder with layered solid walls (i.e., continuum shell model), as shown in Figure 4.11 (b). A femtosecond laser source is treated as a heat source which irradiates from the top (incoming) layer to the bottom, as shown in Figure 4.11 (a). However, the irradiation direction in Figure 4.11 (c) is shown in the inverse direction for computational purposes only. Figure 4.11 (c) shows a schematic of the normal and angular incidence of the laser

beam with the nanotube surface that is considered for the implementation of initial and boundary conditions (the red arrow shows the incident laser beam first irradiating the upper graphene layer in the nanotube). In Figure 4.11 (d), a cross-sectional view of the three-walled nanotube with the first, second, and third upper layers and first, second, and third lower layers with respect to the incident laser beam is illustrated. The upper half and lower half of the tube volume were each divided into 20 segments (Figure 4.11 (b)) to apply the proportionate amount of heat flux at every segment, given the curvature of the tube, and for the mesh creation for the boundary value.

Uniform heating by the laser beam was achieved due to the extremely small size of MWCNTs. The transient temperature distribution of the single MWCNT was obtained by solving the governing heat transfer partial differential equation (PDE):

$$\rho C_p \left(\frac{\partial T}{\partial t} + u_{trans}.\nabla T\right) + \nabla.(q + q_r) = -\alpha T:\frac{dS}{dt} + Q \qquad (1)$$

where ρ and C_p are the density and specific heat capacity at constant pressure. In our calculation, ρ is taken as 2100 kg/m^3 and C_p has a temperature-dependent value of 0.75 J/(g·K) at room temperature (Lu et al., 2006; Pradhan et al., 2009). T is absolute temperature,$\boldsymbol{u}_{trans}$is the velocity vector of translational motion, **q** and $\boldsymbol{q_r}$ are the heat flux by conduction and radiation, respectively; α is the coefficient of thermal expansion, S is the second Piola-Kirchhoff stress tensor, and Q contains additional heat sources. The term $-\alpha T:\frac{dS}{dt}$ is the thermoelastic damping and accounts for thermoelastic effects in solids. For computational simplicity, a three-walled CNT was used (cross-section shown in Figure 4.11 (d)), having graphene-like walls, each with a wall thickness of 0.35 nm. A tube inner radius of 4 nm and length of 1 μm were used. To simplify the calculation, we made several assumptions. First, in our experiment, MWCNTs are located on a substrate, but here we only consider one individual MWCNT and neglect the reflection caused by the substrate because the reflection of SiO_2 at 800 nm is only 3% (Malitson, 1965). Second, we did not consider

the heat loss due to the thermoelastic effect due to the much smaller thermal expansion coefficient of CNTs compared to metals (for CNTs it is on the order of 10^{-6}) (Bao et al., 2009). Third, we assumed fixed spatial locations of the CNTs during laser irradiation, making $\boldsymbol{u}_{trans}$ negligible. The laser spot diameter is ~ 300 μm and the diameters of the MWCNTs are between 10 nm and 20 nm, allowing the Gaussian laser beam spatial profile to be treated as plane waves with evenly distributed energy over the entire nanotube surface. Then the above equation becomes:

$$\rho C_p \frac{\partial T}{\partial t} + \nabla.(q + q_r) = Q \qquad (2)$$

where Q, in our model, represents the laser heat source with both spatial and temporal Gaussian distributions. Ignoring the edge effects (since the laser spot size is much larger than the individual MWCNTs), only the temporal distribution is considered in our simulation. The intensity of the ultrashort pulse can be approximated as $I(t) \cong \alpha I_0\, exp(-2.77\frac{(t-t_0)^2}{\tau^2})$, where $I_0 = \frac{P_{ave}}{A \cdot \tau \cdot prr}$ is the peak laser intensity, P_{ave} is the average laser power, A is the laser spot area, and prr is the pulse repetition rate (we use 1 kHz, meaning a laser pulse period of 1 millisecond) (Paschotta, 2008). t_o defines the peak location of the laser pulse and the pulse duration τ is 40 fs. We considered the following temporal and spatial distribution for the modeling:

$$I\,(t,x,y) \cong \alpha I_0 \exp\left(-2.77\frac{(t-t_0)^2}{\tau^2}\right) \exp\left(-\frac{2(x^2+y^2)}{d^2}\right) \qquad (3)$$

For the mesh creation to implement the finite element analysis, the three-walled CNT was divided into various zones for heat input (first, second, and third upper layers, first, second, and third lower layers, input boundary flux, input domain, etc.), as shown in Figure 4.13. α ~ 0.25 is the absorbance of MWCNTs, which was taken from an experimental value of MWCNT film (Xiao et al., 2010). Here we use α ~ 0.643 based on the fact that the average diameter of MWCNT is 20 nm and the absorption coefficient of a film of 22 nm is approximately 7.4×10^5 cm^{-1} (De Nicola et

al., 2015). The heat fluxes **q** and $\mathbf{q_r}$ were calculated using Fourier's law (**q** = -$k\nabla$T) and the Stefan-Boltzmann law ($\mathbf{q_r} = \varepsilon\sigma(T_{amb}^4 - T^4)$), respectively, where k and σ are thermal conductivity and the Stefan-Boltzmann constant (5.67 x 10^{-8} W/ m^2K^4), respectively, ε is the emissivity (~ 1 for CNTs, a perfect black body), and T_{amb} is the ambient temperature (room temperature, 293.15 K). CNTs, being anisotropic, have a radial thermal conductivity of ~ 1.51 W/m K and an axial thermal conductivity value of ~ 3000 W/m K, respectively, at room temperature (Kim et al., 2001). Due to the significantly larger axial value, we neglect the temperature variation due to radial thermal conductivity (Pop et al., 2006). The temperature dependence of the axial thermal conductivity and heat capacity of the nanotubes are fitted according to $k_{axial}(T) = \frac{1}{(2.769\ X\ 10^{-6}+9.20721\ X\ 10^{-7}\ T)}$ and $C_p(T) = (3900 - 21.08\,T + 0.03492\,T^2)$, respectively (refer to the plots of $k_{axial}(T)$ and $C_p(T)$ in Figure 4.12). A summary of the model parameters and details of the boundary and initial conditions as well as the mesh generation provided in Figure 4.12.

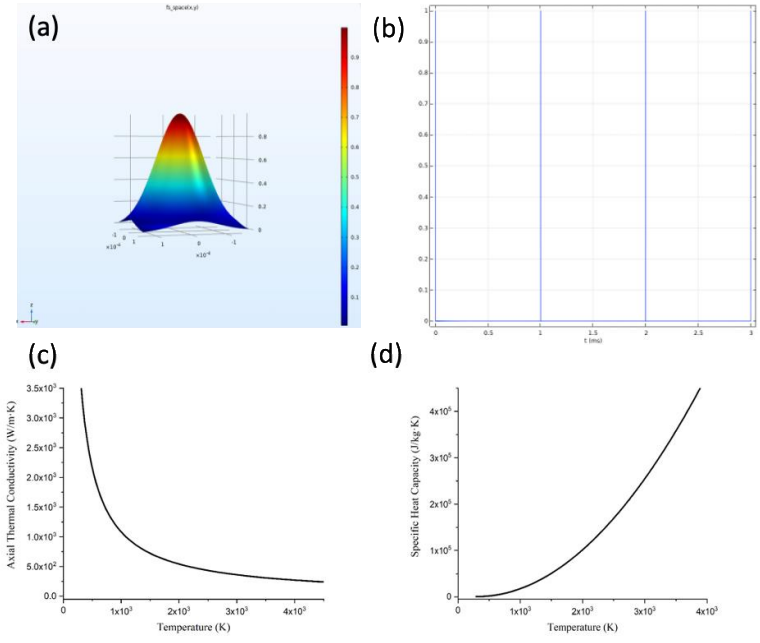

Figure 4.12. (a) Figure Gaussian laser beam: spatial distribution; (b) periodic multi-pulse femtosecond laser beam; (c) temperature-dependent axial thermal conductivity of MWCNTs (k_{axial}(T)); (d) temperature-dependent specific heat capacity of MWCNTs (C_p(T)).

4.2.3.2 Parameters used in the modeling.

To resolve the numerical model, the parameters discussed in the previous section were used in the calculation; the parameters are summarized in Table 4.1.

Table 4.1. Finite element analysis model parameters used in COMSOL

Parameter	Variable	Value	Units
Thermal conductivity	(Nakada et al., 1996); $k_{ij} = 0$	(Nakada et al., 1996)	W/(m·K)
Density of MWCNT	rho	2100	kg/m³
Heat capacity at constant pressure	Cp	Cp(T)	J/(kg·K)
Diameter of MWCNT	r_cnt	3.05[nm]	3.05E-9 m
Length of MWCNT	l_cnt	20[nm]	2E-8 m
Laser wavelength	lam	800[nm]	8E-7 m
Average power of laser	p_ave	0.057[W]	0.057 W
Laser pulse width	t_pulse	40[fs]	4E-14 s
Laser beam radius	r_focus	150[um]	1.5E-4 m
Layer thickness of MWCNT	t_layer	0.35[nm]	3.5E-10 m
Laser peak intensity	I_peak	p_peak/area	2.016E16 W/m²
Laser spot area	area	pi*(r_focus^2)	7.0686E-8 m²
Laser peak power	p_peak	p_ave/(t_pulse*prr)	1.425E9 W
Absorbance of 1st layer	a1	0.29	0.29
Absorbance of 2nd layer	a2	a1*(1-a1)	0.2059
Absorbance of 3rd layer	a3	(1-a1-a2)*a1	0.14619
Total absorbance of MWCNT	a_total	a1+a2+a3	0.64209

4.2.3.3 Boundary conditions and initial conditions

The boundary heat sources are governed by $-n \bullet q = Q_b$, where n is the normal vector to the surface. The quantities of heat sources applied on different layers of the tube are expressed as follows: $Q_b = \alpha I(t) \cos\theta$, on the 1st upper layer, on the 2nd upper layer, and on the 3rd upper layer. $\theta$is the angle between the incident beam and the normal vector of the surface, and α is the total absorbance of light in MWCNTs at 800 nm. For boundaries other than the input boundaries, we applied thermal insulation boundary conditions, which are governed by $-n \bullet q = 0$. We also applied surface-to-ambient radiation to all the boundaries.

Since we calculate the time-dependent temperature profile of MWCNTs, the initial condition (temperature of MWCNTs at t = 0 s) is the starting point to solve Equation (2) above, defined as $T(x, y, z, 0) = 293.15\ K$, on the entire structure.

4.2.3.4 Mesh generation and convergence verification

The mesh structure, as shown in Figure 4.13 below, was constructed as follows. In the radial direction of the tube, we used a minimum mesh size of 0.1 nm; in the axial direction, we used a minimum mesh size of 100 nm. Three elemental segments along the radial direction per layer were considered, corresponding to the three-walled tube.

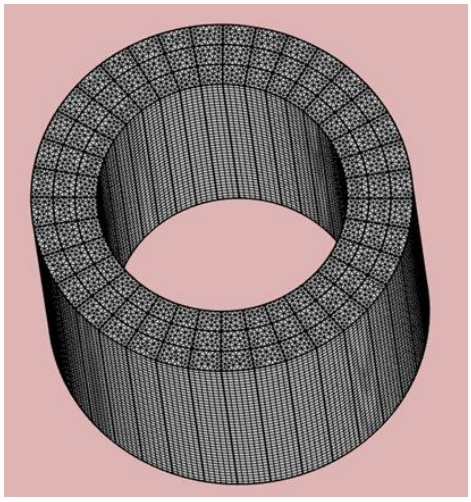

Figure 4.13. (a) CNT mesh structure for numerical calculation

4.2.3.5 Results and discussion

Figure 4.14 shows the modeling results of the average transient temperature of the MWCNT when all six layers (in Figure 4.11 (d)) were considered for their absorption with an average laser power of 57 mW. A temperature of 2200–2000 K is estimated in the upper half of the tube that may be sufficient to soften (or even ablate) the nanotubes to make nanoribbons. Furthermore, if we consider the MWCNTs with absorption of an average laser power of 114 mW, an average temperature of 2700–2400 ^{0}C will be generated, as shown in Figure 4.15 (a). A temperature of ~ 2900 K was earlier reported for their onset of sublimation for SWCNTs (Begtrup et al., 2007). Since the thermal ablation/etching of MWCNTs is expected to happen at a lower temperature than that of SWCNTs, our predicted temperature values are consistent with the experimental findings. A lower ablation/unzipping temperature in our case could likely also arise from a high level of defects present in our MWCNTs (as evidenced by the high D peak in the Raman spectrum). The effect of Stone-Wales defects in SWCNTs by reducing their melting temperatures from 4800 K down to 2600 K was previously reported theoretically (Zhang et al., 2007). The transient temperature is generated in picoseconds duration of laser exposure, after which the heat flow continues toward a thermal equilibrium state. This is rational because the high electromagnetic field interaction with matter (solid), enabled by a femtosecond laser irradiation, causes electronic excitation followed by energy transfer (in the form of heat) from electrons to the lattice. Figure 4.14 (b) shows a profile of the surface temperature of an MWCNT at 0.001 ms. Typically, this timescale is in the picosecond range, providing the equilibrium timescale for such processes. To observe the heat accumulation/buildup effects over the entire experimental time of exposure (and hence, the overheating due to the buildup), the modeling was carried out for 3 ms

(actual experimental time). As shown in Figure 4.15 (b), no heat buildup and associated temperature rise were observed due to exposure to thousands of ultrafast pulses.

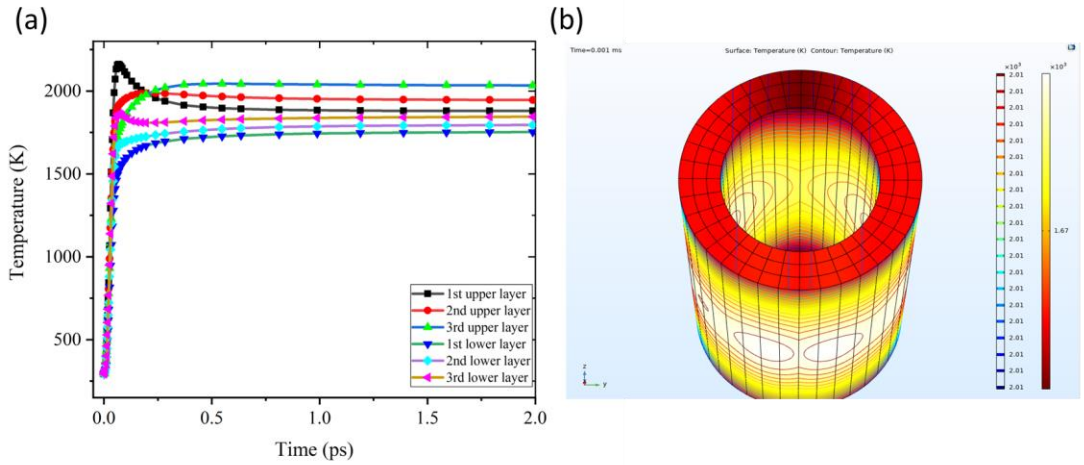

Figure 4.14. (a) Average transient temperature of an MWCNT when all six layers are considered for their absorption with an average laser power of 57 mW; (b) surface temperature profile of an MWCNT at 0.001 ms.

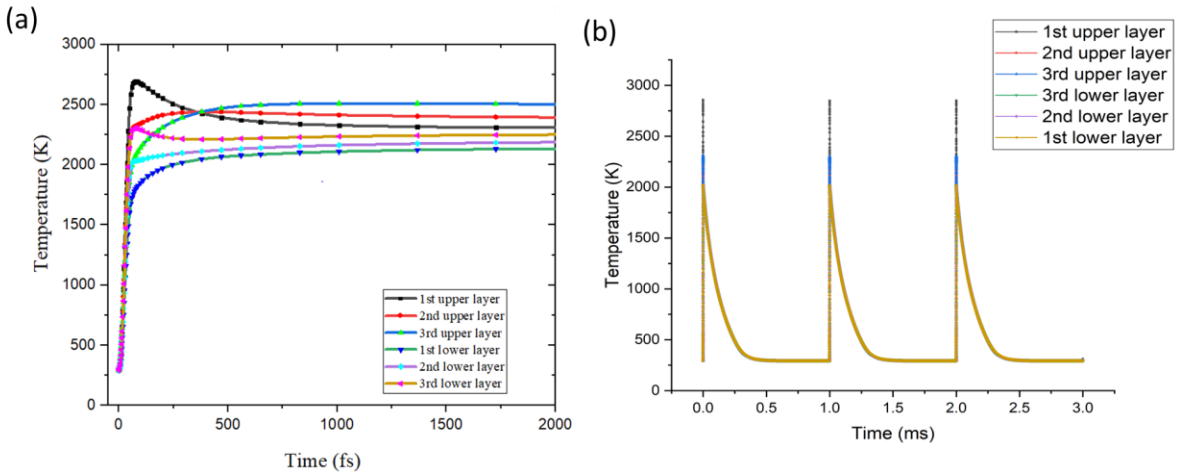

Figure 4.15. (a) Average transient temperature of the nanotubes with absorption on every layer with laser average power of 114 mW ; (b) surface heat accumulation and effect on temperature; surface temperature profile of an MWCNT between time t = 0 and 3 ms.

4.3 Summary

In this chapter, the interactions between laser and matter, particularly the UFL interactions with MWCNTs, were studied with a focus on the high electromagnetic-field interaction with CNTs. A manufacturing technique of laser-unzipping of CNTs was developed to address the issues associated with currently available technologies for fabricating GNRs. The optical and electronic properties, surface topography, and molecular vibrational properties of manufactured low-dimensional nanomaterials are evaluated in this work. By utilizing high electromagnetic-field interaction with CNTs, achieved by UFL radiation, successful demonstration of the nanomachining of CNTs and their transformation to GNRs and carbon nanocrystal hybrids was made. The ribbons are narrow (typically less than 15–20 nm in width or even smaller depending on tube diameter), while the nanocrystals showing well-defined crystalline structures are embedded along the length of the ribbons from approximately 15 nm down to 3 nm in size. While the nanotubes are metallic in their electronic properties initially, the light-matter interaction provides them with semiconducting and/or insulating properties, potentially enabling their use in several applications such as nanoscale devices for sensing and electronics. The processes of using coherent and high-field electromagnetic radiation for laser-induced nano-machining (LINM) and laser-induced phase-transformationare scalable, spatially controllable, and operated at room temperature, thus making them suitable for numerous industrial applications of CNTs and related systems.

Chapter 5 - Carbon Nanotube Alignment based on the Dielectrophoretic Method and Nanoribbon Plasmonics Simulation

This chapter explores the possibility of aligning CNTs by using a principle called dielectrophoresis (DEP). Also, the chapter will employ a hybrid dielectrophoresis and additive manufacturing method to align the CNTs.

The purpose of CNT alignment is to offer a method to the fabrication of GNR arrays. By combining a material printing technique and dielectrophoretic method the CNT alignment proof-of-concept was demonstrated. A UFL based nanomachining of aligned CNTs, therefore, will enable the manufacturing of aligned GNRs. Applications based on GNRs depend on the orientation of the ribbons and number of ribbons, such as field electrical transistors and on-chip sensors. Another important application is modifying the optical resonance of graphene plasmonics. If the CNTs are produced along the required spatial direction, the output GNRs could be well-controlled according to the pre-designed structures, and thus obtain the desired signals. This chapter first introduces CNT alignment techniques developed by researchers, then describes the dielectrophoresis technique and experimental design to align our CNTs; graphene plasmonics are then introduced, which is the primary motivation to pursue the alignment of CNTs and GNRs. The last section of the chapter presents the simulation of GNR array plasmonics.

5.1 CNT alignment techniques

There are two major approaches to aligning CNTs: (1) alignment during the growth process, guiding the tubes to grow along a given spatial direction, and (2) alignment after the growth process. We focus on post-growth processing alignment methods that include stretching CNTs in polymer, applying shear force, utilizing electric and magnetic fields, and printing.

Stretching CNTs in a polymer matrix (Peng, 2008) is one type of solid-state process, as shown in Figure 5.1 (a)–(c). The stretching method utilizes a polymer matrix to pull out embedded CNT arrays to induce a stable and uniform sheet, followed by spin-coating a composite film. The CNTs will sit in a polymer sheet, which makes them easy to transfer by peeling them off. This is a simple and efficient method that can control the thickness and functionality of the composite film. The drawback of this method is that it is not suitable for all MWCNT arrays, and it largely depends on the quality of the arrays. The so-called "domino pushing" (Wang et al., 2008) method (shown in Figure 5.1 (d)) involves a lateral shear force applied during the peeling process which forces the CNTs to align in the out-of-plane direction. By placing a cylinder upon the CNT array with constant pressure, CNTs are pushed over to one direction. After this step, the aligned CNT sheet is ready to be used by applying a membrane to peel it off the substrate. One drawback of this method, similar to the previous two methods, is that it requires initial high-quality CNTs. Another drawback of this method is that some of the CNTs can be damaged during the process.

Magnetic/electric field-induced alignment is an attractive method that relies on the anisotropic magnetic/electric susceptibility and anisotropic polarizability of CNTs which produce a magnetic/electric torque that helps the CNTs orient parallel to the field direction. By utilizing a magnetic/electric field, CNT alignment can be realized either in post-processing or during growth. For the post-process procedure, to make CNTs rotate and orient freely along the magnetic field direction, typically a solvent is required to disperse the CNTs. As shown in Figure 5.1 (e) (Goh et al., 2019), the substrates holding the solution-based or polymer matrix-based CNTs are placed within a magnetic field. Two advantages of this method are it can reach a high level of individual CNT alignment, and it is free of any electrodes. The drawback of the magnetic field method is that it typically requires a strong magnetic field, as high as 10–30 T (Smith et al., 2000). Regarding

methods utilizing an electric field, electrodes must be deposited on the substrates to apply a voltage supply, as shown in Figure 5.1(e). The degree of alignment can be controlled by tuning the frequency and amplitude of the electrical field (Chen et al., 2001). Earlier work, in this regard, required standard lithographic fabrication of electrodes and the process is typically expensive, tedious, and does not involve flexible substrates such as plastic, etc. The inkjet printing method has attracted attention because it offers several advantages, such as it does not need an additional process of the substrates, it is fast and cheap, and it has the capability to print small-scale electronic devices directly because it can deposit materials simultaneously or layer-by-layer with high pattern precision. The degree of CNT alignment by printing depends on the solution suspension, the surface roughness of the substrate, the rate of evaporation, and the evaporation mechanism.

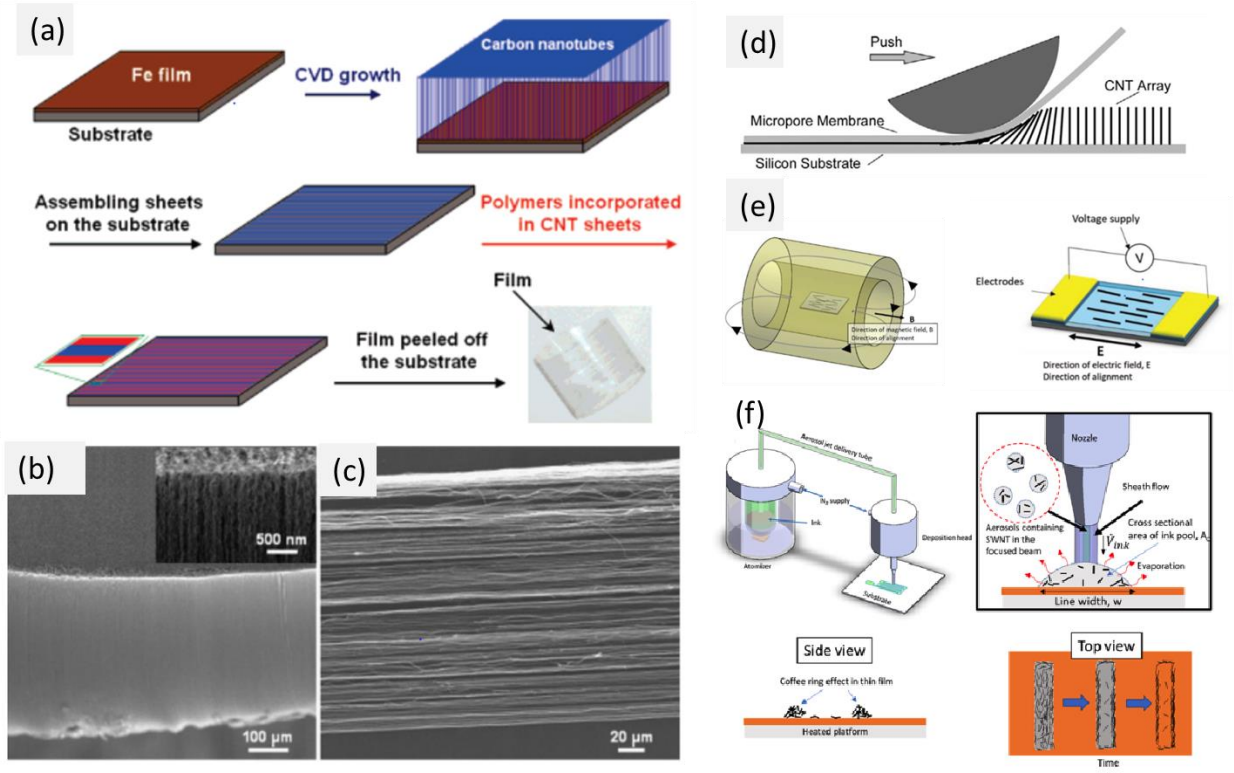

Figure 5.1. CNT alignment techniques; (a)–(c) stretching method (Peng, 2008); (d) domino method (Wang et al., 2008); (e) magnetic and electric field method (Chen et al., 2001); (f) printing method (Goh et al., 2019).

5.2 CNT alignment based on the dielectrophoretic method

As mentioned in the previous section, the electric field has been proven to be an effective method to align CNTs. When the migration of CNTs in a suspension relies on the electric field, the mechanism is called electrophoresis. The dielectrophoresis (Wang et al.) method involves the migration of CNTs due to CNT polarization induced by a oscillating electric field. The degree of alignment can be controlled by tuning the frequency and amplitude of the electric field. When CNTs are exposed to an oscillating electric field, an electric dipole moment is created in the tube. The dipole moment along the longitude axis of the nanotube is much stronger than that in the perpendicular direction; therefore, the nanotube in a suspension solution has the freedom to be aligned to the electric field direction. The DEP force on the nanotube can be expressed (Raychaudhuri et al., 2009) as:

$$F_{DEP} = \Gamma v \varepsilon_m \varepsilon_0 R_e[f_{cm}] \nabla E_{rms}^2$$

where Γ is a geometry factor that contains the volume information of the nanotube *v* is the CNT's volume, ε_m and ε_0 are the permittivity of the fluid medium and free space, respectively, and ∇E_{RMS} is the root mean square of the gradient of the external electric field. The polarization factor (Clausius-Mossotti factor) f_{cm} is expressed as (Raychaudhuri et al., 2009):

$$f_{cm}(\omega) = \frac{\varepsilon_{cnt}^* - \varepsilon_m^*}{\varepsilon_{cnt}^* + 2\varepsilon_m^*},$$

$$\varepsilon^* = \varepsilon - i\frac{\sigma}{\omega}, \omega = 2\pi\nu$$

$Re[f_{cm}]$ is the real number part of f_{cm}, which is related to the nanotube and the medium. ε_m^* and ε_{cnt}^* are the permittivity of the fluid and CNT, respectively. Re[*f(w)*] is the real part of the complex polarization factor and *E* is the electric field. As shown in Figure 5.2, when a CNT is placed in the DEP field, the dielectrophoretic force F_{DEP} balances the hydrodynamic drag force F_D on the

nanotube, and $F_D = \frac{4\pi\mu l V}{ln(2l/r)-0.72}$, where μ is the viscosity of the fluid, l is length of the nanotube, and r is the radius of the nanotube. V is the fluid velocity which can be expressed as $V = \frac{F_{DEP}(ln(2l/r)-0.72)}{4\pi\mu l}$. When the two forces balance, the CNT lands on the substrate. Further details about the DEP principle are provided in Dimaki's work (Dimaki & Bøggild, 2004). From the equation of the DEP force, it is known that the factors that affect CNT alignment include the geometry of the nanotubes, the properties of the CNT solution/medium, and the strength of the electric field. In this study, four parameters were adjusted to control the alignment of the nanotubes: bias voltage and frequency of the electric field, distances of the electrodes, and concentration of nanotube solution. Since the actual process can be complicated, we will vary parameters, such as the solution density and the electric field, during the experiments while keeping other parameters constant. More research on the optimization of DEP processes is needed in future.

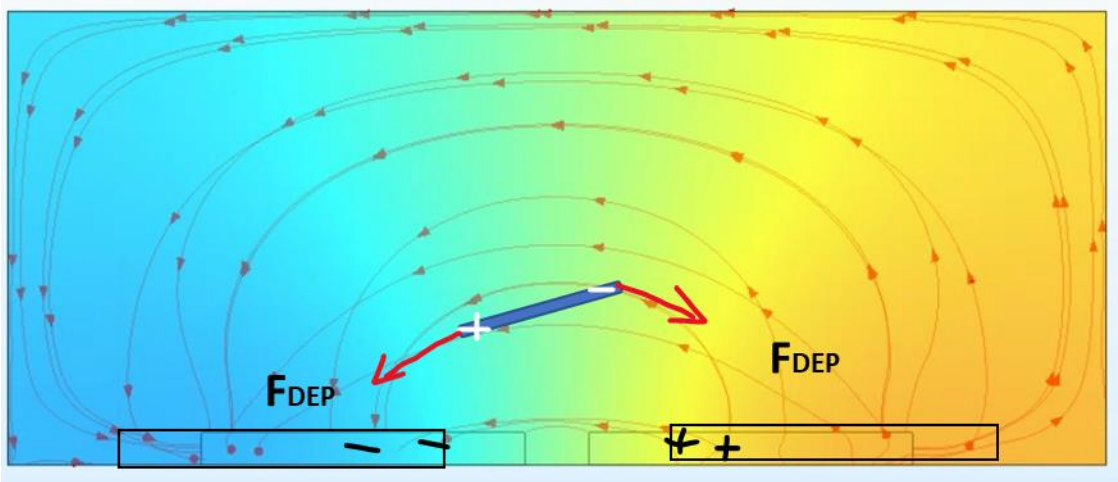

Figure 5.2. Schematic diagram of the forces experienced by a CNT in the electric field during DEP process of aligning nanotubes.

The CNTs used in this work were grown as a forest on silicon substrate using the chemical vapor deposition method (Lee et al., 2019); the CNTs had a mean diameter of 10 nm and a height

of 0.418 mm. It should be noted that the average lengths of CNTs were several micrometers after transferring the CNT forest into the solution and following a sonication process. The nanotubes were ultrasonically dispersed in an organic DMF solvent (Sigma-Aldrich, USA) to form a dispersion with a density of 10 ug/L. The chips used in this study are made of glass substrates coated with a dielectric layer (SU-8) and hydrophobic layer (Teflon), with deposited ITO (indium tin oxide) as driving electrodes with designed patterns, as shown in Figure 5.3 (b) and (c). The distances between the two electrodes vary from 20 to 100 μm, while the thickness of the electrodes is 250 nm. Figure 5.3 (a) shows a schematic diagram of a DMF droplet containing isolated CNTs on a substrate with aligned and microfabricated electrodes. Alignment markers marked in Figure 5.3 (c) on the chip represent the six areas where we dropped the CNT solution. At the marked Areas 1 to 6, the frequencies of the applied electric field during DEP experiments are 0.5 MHz, 1 MHz, 2 MHz, 3 MHz, 4 MHz, 5 MHz, and 0.5 MHz, respectively. The root mean square voltages applied from Area 1 to 6 are 116.2 V, 37.7 V, 28 V, 17.5 V, 12.3 V, and 133.8 V, respectively. For each marked area, 1 μl of CNT solution was dropped on the substrate and the electric field was applied until the droplet was dried. The SEM images of CNTs after applying an electric field, shown in Figure 5.3 (d)–(g) were obtained using a Hitachi SU8230 Field-Emission SEM with a 10 kV accelerating voltage. Figure Figure 5.3 (d) and (g) show the aligned CNTs in Area 3 with low and high magnification, respectively; Figure 5.3 (e) and (f) show the CNTs in aligned bundles in Area 1 and Area 2, respectively.

These images demonstrate that the CNTs were aligned between the electrodes and suggest that many CNTs have overlapped between two electrodes for low electric field frequencies. CNTs dropped on Area 3 with the electric field with a frequency of 2 MHz and a magnitude of 28 V root mean square achieved the best alignment. From the images, it is observed that the nanotube

orientation is strongly dependent on the magnitude and the frequency of the electric field; it is also observed that the alignment degree of the CNTs reduced gradually with decreased electric field frequency. With a lower frequency, the nanotubes were tangled, which suggests an optimization of the evaporation timing and the concentration of the CNT solution is needed. Fewer CNT bundles were observed at higher frequencies; however, they are still there suggesting an improved dispersion method for the CNT solution is needed. The distance between electrodes in Area 3 is 60 μm; however, there is no evidence showing 60 um is better than 20 μm because, compared with the distances, the lengths of the CNTs are small. This CNT alignment method based on DEP is highly reproducible, fast, and low-cost.

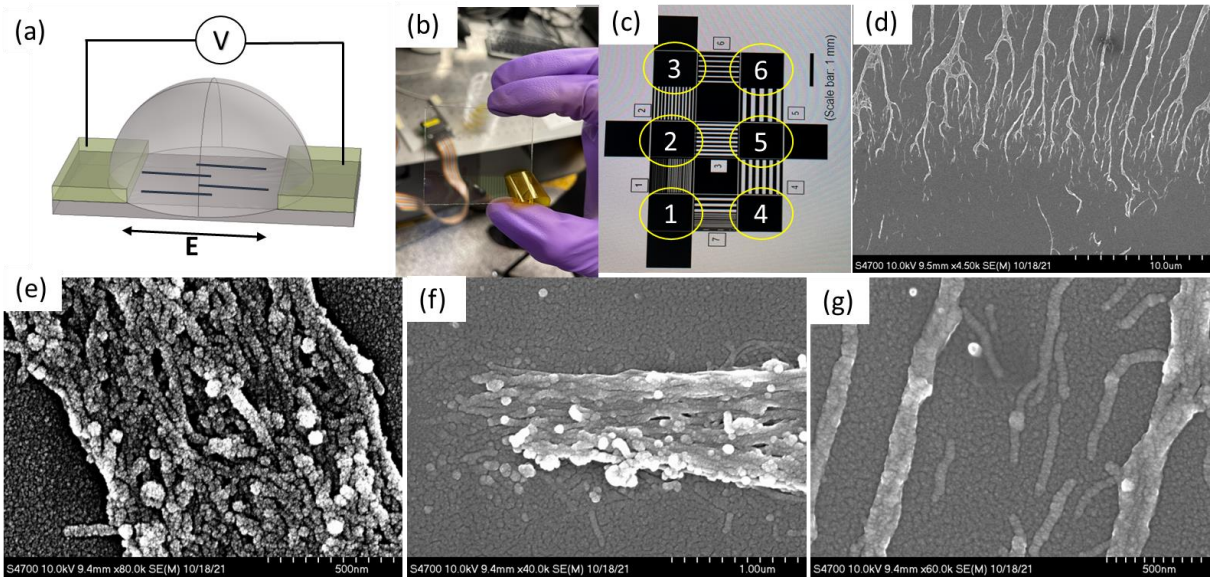

Figure 5.3. (a) Schematic diagram of the DEP method; (b) substrate with patterned electrodes; (c) electrode design diagram; (d)–(g) SEM images of CNTs after applying an electric field; (d) and (g) aligned CNTs in Area 3 with low and high magnification.

While the CNTs are straight and aligned in the above experiment, the CNTs are tangled together; we hypothesize two reasons for this. First, the density of the solution is high or the CNTs are not dispersed evenly, so while the CNTs are migrating and settling, they are attracted to each other and form bundles. This can be resolved by diluting the solution and utilizing IPA as the

solvent because the concentration of CNTs dispersion in IPA is less than that in DMF. Secondly, the applied electric voltage is high, thus the DEP forces on the CNTs are higher than the dragging forces, meaning the CNTs do not have sufficient time to react and migrate. The proposed solution to this is to apply lower electric field and use IPA as a solvent because IPA can volatilize faster than DMF. Another phenomenon we observed is that the CNTs only become aligned near the electrodes and there are far fewer CNTs in between the electrodes; this is due to the fact that the distances between the electrodes in the design are larger than the length of the CNTs, thus it is difficult for the CNTs to travel such far distances.

Electrode Design Considerations Using Material Printer and Conductive Ink: An alternative approach for the Fabrication of DEP Substrates

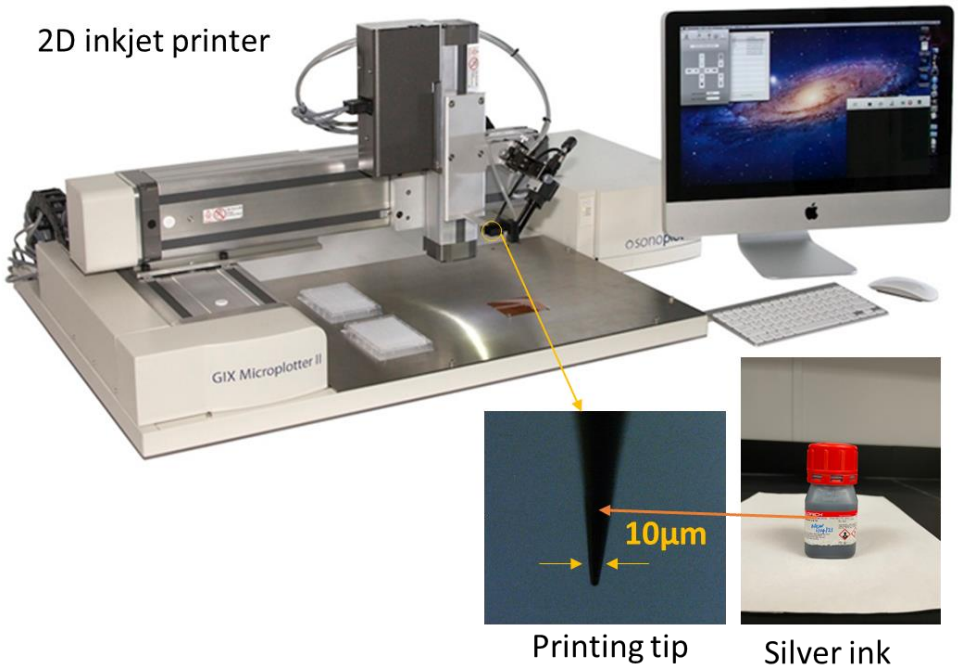

Figure 5.4. A Microplotter II from Sonoplot.

Based on the results of the above experiment, to obtain smaller distances in between electrodes, we designed a new electrode pattern combining our Microplotter II Material Printer (GIX Microplottor II, as shown in Figure 5.4) and the DEP method. Photolithographically fabricated electrodes with large distances (200 µm and 300 µm, as shown in Figure 5.5) were involved for proof-of-concept demonstration of the printing method of the active DEP areas definition and printing, however, the whole chip can be printed later. Silver microelectrodes (as shown in Fig. 5.6) on the large-scale electrodes (Fig 5.5) were made to achieve the narrow gaps for DEP. The average particle size of conductive printing silver ink (purchased from

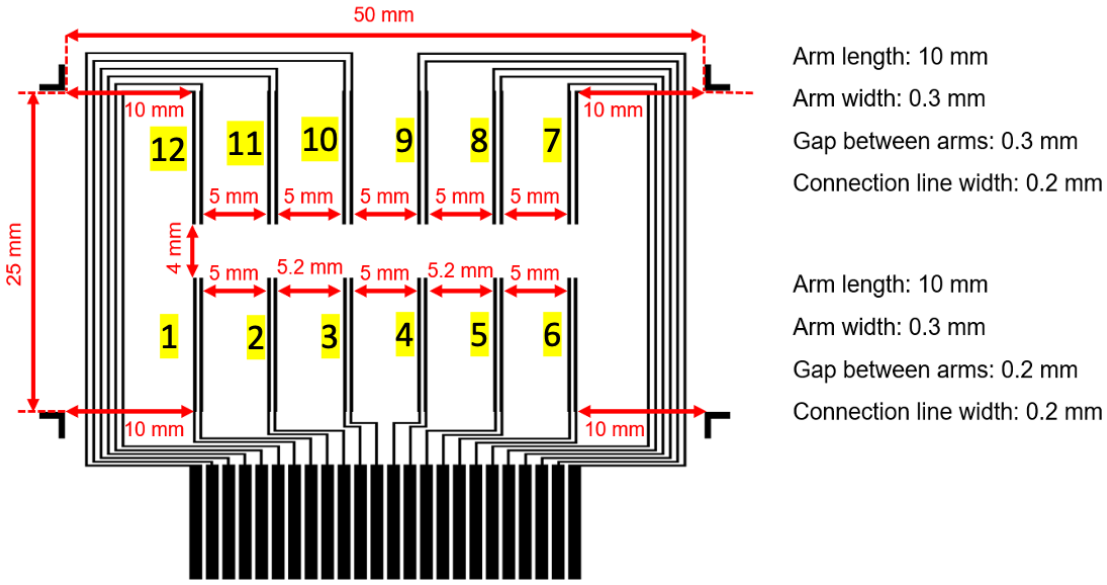

Figure 5.5. Design of electrodes for CNT alignment.

Aldrich Sigma, product #97022) was 100 nm; we measured the average resistance of a one-layer printed pattern to be under 10 Ω for a straight printed line on silicon over centimeter distance, with a width of 200 µm. As shown in Figure 5.4, a 10-µm diameter glass tip capable of printing a feature size as small as 10 µm with silver ink. The first layer, shown in Figure 5.5, is a photolithographically fabricated chip design on glass but in principle it could be printed and on

any substrates (our future work). In Figure 5.5, the numbers 1 to 12 indicate 12 pairs of arms, upon which when an electric field is applied with variable parameters during the DEP process. The gaps between the upper arms and lower arms are 0.3 mm and 0.2 mm, respectively.

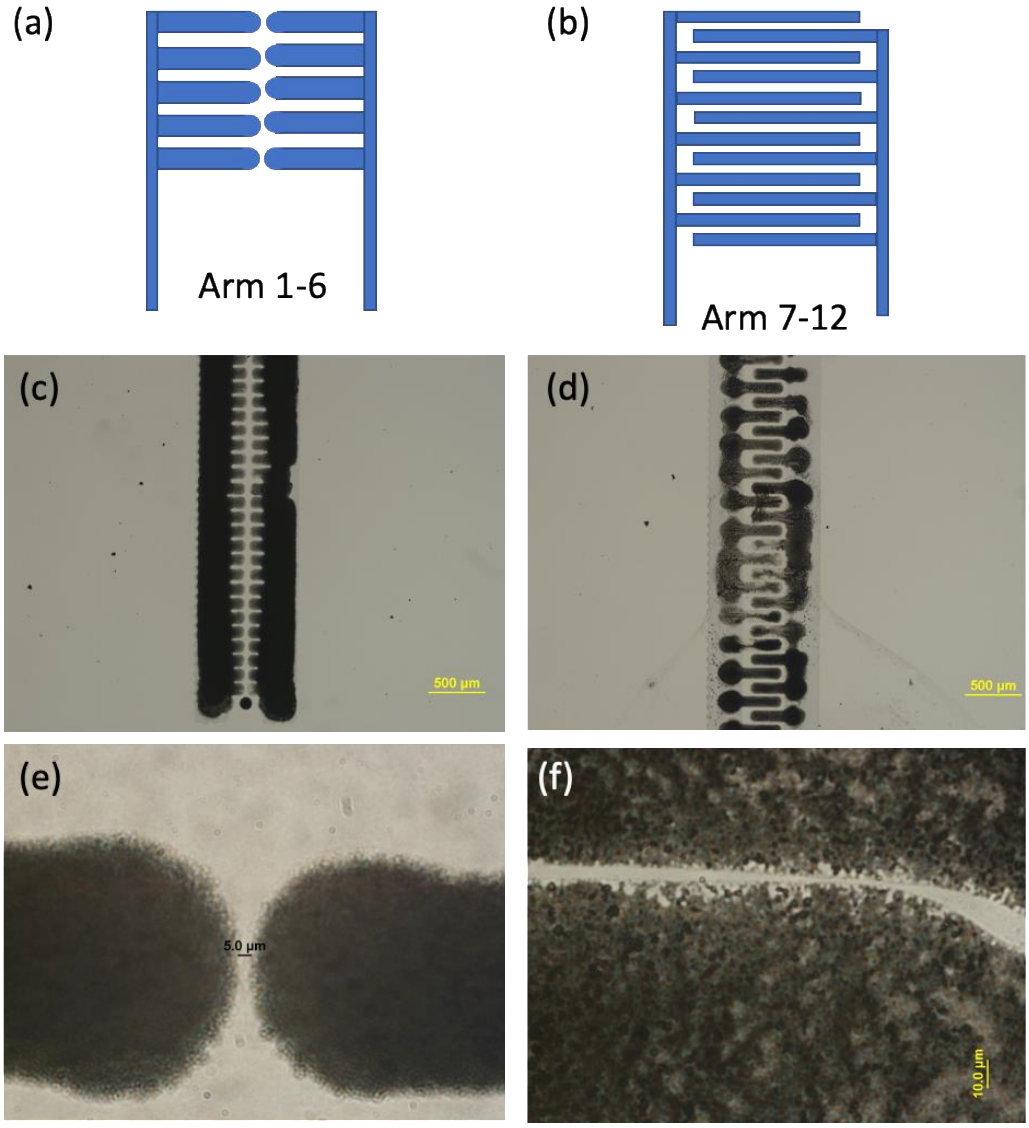

Figure 5.6. (a) and (b) Electrode patterns for microplotter printing; (c) and (e) optical microscopy images of the printed electrodes between arms 1 to 6; (d) and (f) optical microscopy images of the printed electrodes between arms 7 to 12.

With the above steps completed, we then used microplotter to print the silver electrodes on the substrates as the second layer. The designs of two electrodes are shown in Figure 5.6 (a) and

(b). The printing method is fast, and it enables designing patterns and choosing substrates (such as flexible substrates); it is therefore an effective method of scaling up and increasing the speed of the process.

Figure 5.6 (c) and (d) show optical microscopy images of the printed electrodes between Arms 1 to 6; Figure 5.6 (e) and (f) show optical microscopy images of the printed electrodes between Arms 7 to 12. The distances between the electrodes depend on the printing process and ink parameters. The microplotter printing parameters include the printing tip's moving speed as well as the voltage and frequency applied on the printing tip. The ink parameters include the dielectric permittivity and the viscosity of the solvent, and the medium dissolved in the solvent. To simplify the process, we consider the shape and the dimensions of the CNTs to be similar and vary our parameters of interest, as listed in Table 5.1.

Table 5.1. Parameters for the printed arms.

	Solution	Frequency (MHz)	Vp-p (V)	Time (min)	Volume (uL)	
Arm 1	IPA/MWCNT	3	50	<1	2	
Arm 2	DMF/MWCNT	3	60	20	4	
Arm 3	DMF/MWCNT	3	60	60	4	
Arm 4	IPA/MWCNT	0.1	100	Dry quickly	3	
Arm 5	IPA/MWCNT	0.5	100	Dry quickly	3	
Arm 6	IPA/MWCNT	1	100	Dry quickly	3	
Arm 7	DMF/MWCNT	3	65	30	4	IPA wash
Arm 8	DMF/MWCNT	2	111	60	4	
Arm 9	DMF/MWCNT	2	111	30	4	IPA wash
Arm 11	DMF/MWCNT	2	60	~60	4	

We performed SEM imaging for all the samples. The resulting SEM images of CNTs between different electrode arms are shown in Figure 5.7 to Figure 5.11.

Comparing all the results, we concluded the conditions for the best CNT alignment that is shown in Figure 5.11. They are taken from Arm 4, which uses IPA as the solvent and in which 0.1 MHz frequency and 100 V voltage was applied. However, more research is needed to optimize this process. The primary advantage of this method is that it offers the potential to scale up for industrial production, because both the printing and ink formulation processes can be automated once they are optimized.

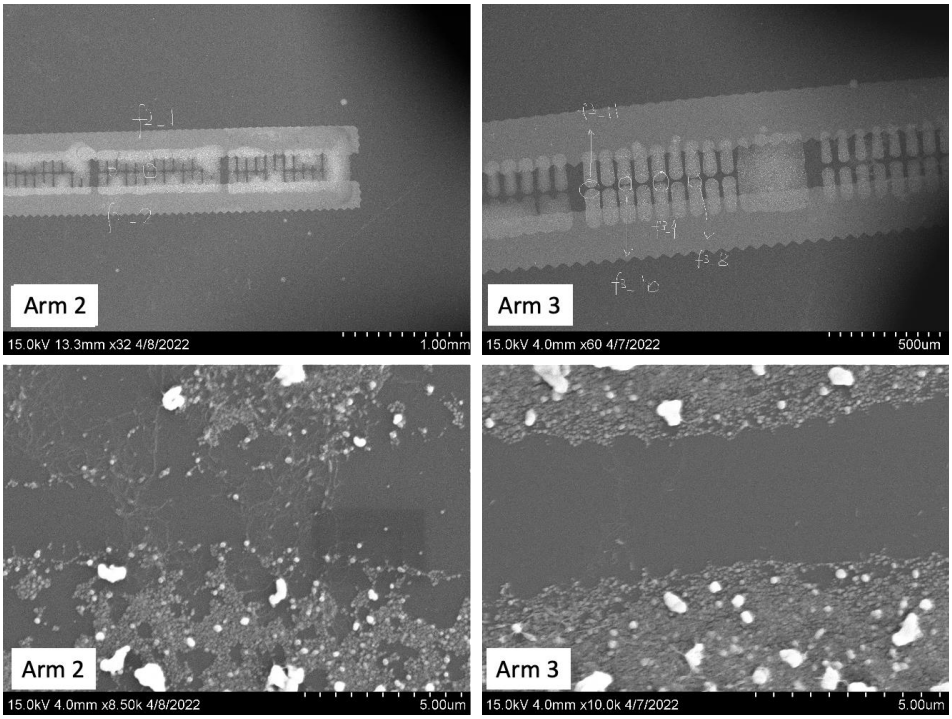

Figure 5.7. SEM images of CNTs between Arm 2 and Arm 3.

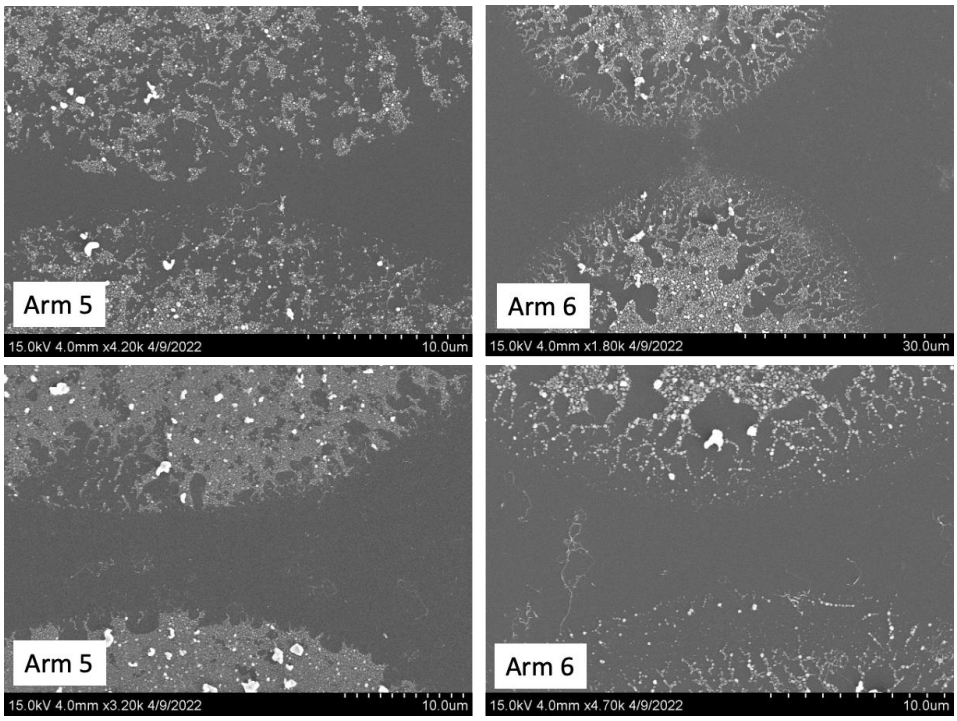

Figure 5.8. SEM images of CNTs between Arm 5 and Arm 6.

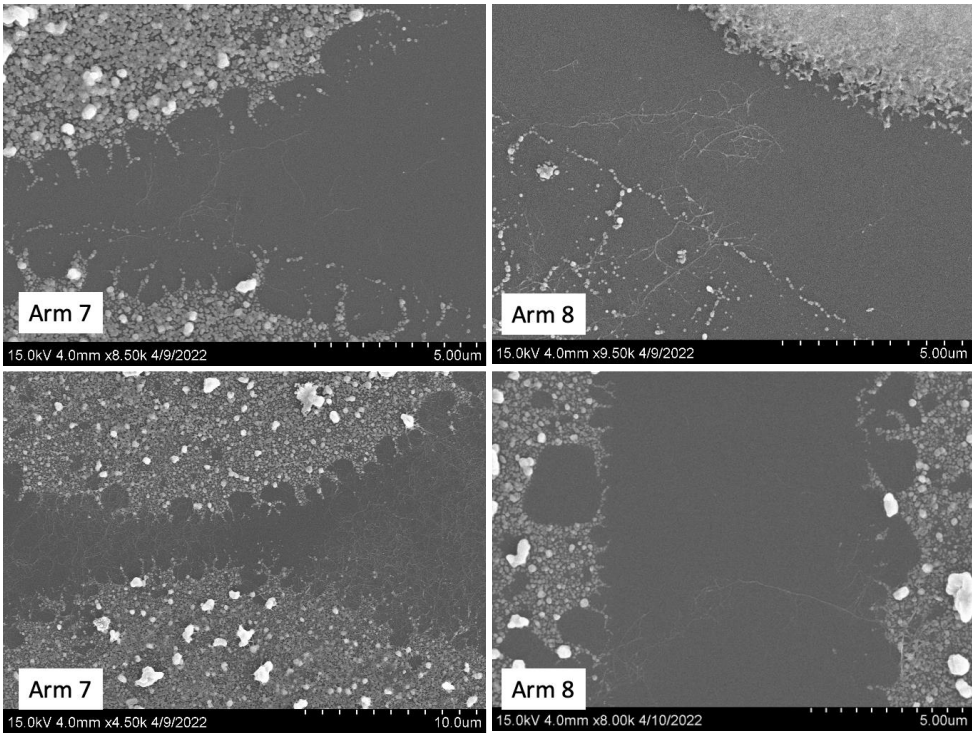

Figure 5.9. SEM images of CNTs between Arm 7 and Arm 8.

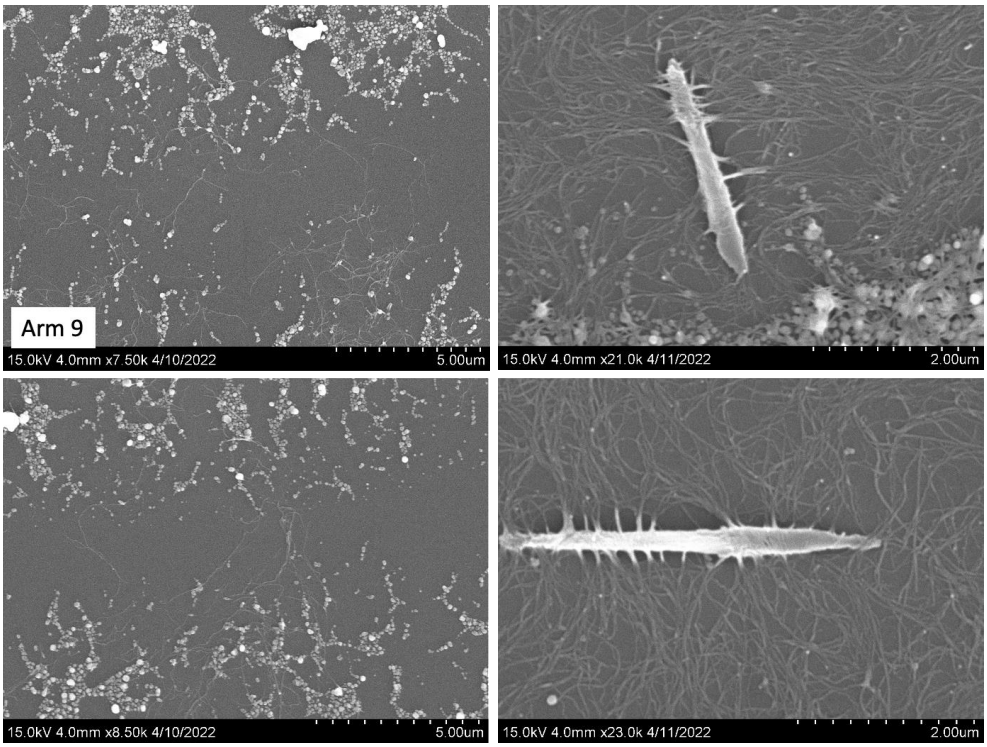

Figure 5.10. SEM images of CNTs between Arm 9 and Arm 11.

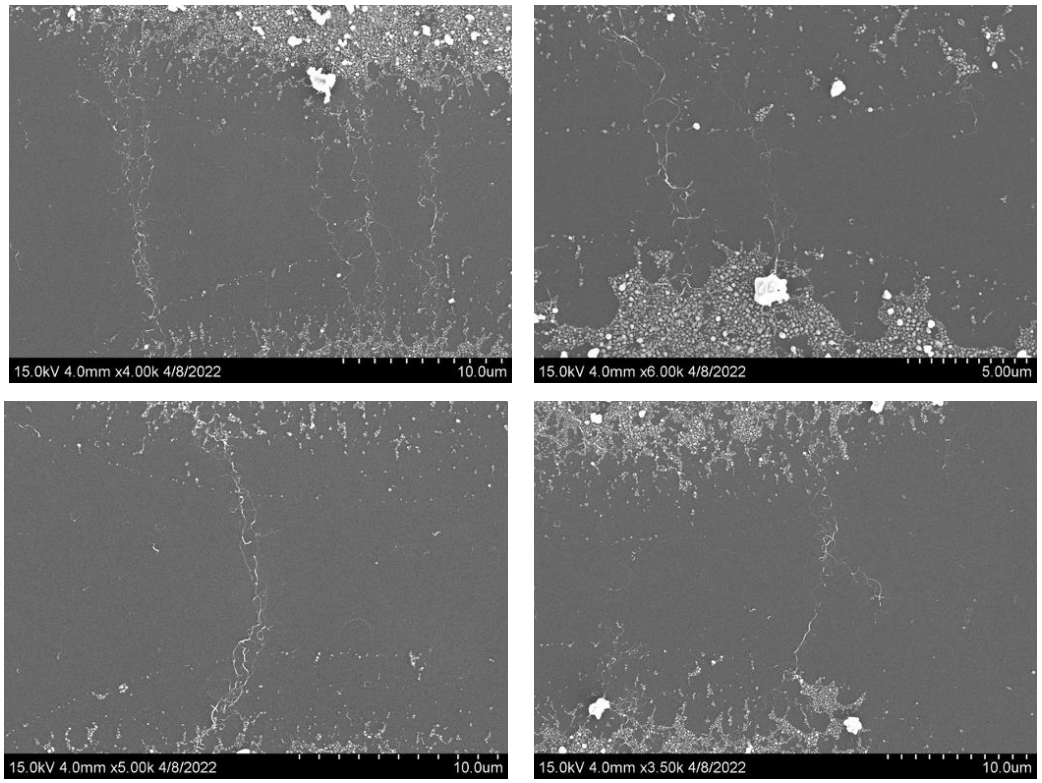

Figure 5.11. SEM images of CNTs in Arm 4.

5.3 Application: Graphene plasmonics

In this section, a unique and fundamental characteristic, called graphene nanoribbon plasmonics, is explained with their roles with technological importance.

Plasmonics is the study of the interaction between electromagnetic radiation and free electrons at metallic interfaces or in small metallic nanostructures, resulting in an enhanced optical near field generation of sub-wavelength dimension. The properties of plasmonics can be manipulated by the selection and fabrication of metallic structures of specific geometries. Surface plasmons are surface waves involving collective electron motion and propagation on metal surfaces or localized in metal nanostructures (e.g., nanoparticles); where they couple efficiently to light, they produce a strong confinement of the electromagnetic field (size << wavelength) and they generate a large enhancement of the optical electric-field intensity (Dennis et al., 2007; González et al., 2007; Myroshnychenko et al., 2008). However, graphene-based plasmonics does not require metals and can be tunable by electrostatic field. Graphene is a tunable plasmonic material that produces unprecedented confinement and strong light-matter interaction in a robust, solid-state environment (Koppens et al., 2011). Graphene has attracted a significant amount of attention due to its enhanced electronic, mechanical, and optical properties. The connection between graphene's unique properties and plasmonics was first established by Ju's study in 2011 (shown in Figure 5.12 (a) and Figure 5.12 (b)), which experimentally verified graphene plasmon-polaritons in micro-scaled graphene ribbon arrays (Ju et al., 2011). This work inspired interest in graphene plasmonics and paved the way for graphene to become a viable platform for dynamic control of optical phenomena as a plasmonic material. Plasmonics in traditional metal-based materials is difficult to tune due to metals having high electron density. Furthermore, tuning can only be done by controlling the size, shape, and dielectrics related with metal nanoparticles or thin films (Toropov & Shubina, 2015); thus, the resonance regime is narrow. However, since the

graphene plasmon resonance is directly proportional to the Fermi level and electron density, it can be dynamically controlled and tuned via chemical doping or electrical gating (Bludov et al., 2013; Jablan et al., 2009; Ju et al., 2011; Yan et al., 2013), meaning that graphene plasmonics can be easily tuned. In addition, graphene plasmonics enables a highly localized electric field and very high optical enhancements of 10^6, about two orders of magnitude higher than that of metals, with lower losses (Yan et al., 2013). Thongrattanasiri et al. experimentally demonstrated spatial mapping and electrical tunability of graphene plasmons (Thongrattanasiri et al., 2012). Other graphene nanostructure designs were investigated in addition to graphene stripes, including graphene nanoring arrays (Yan et al., 2012), doped graphene nanodisks (Thongrattanasiri et al., 2012), and stacks of nanodisks (Fang et al., 2014), as shown in Figure 5.12 (c)–(f). Among these structures, graphene ribbons have gained the most attention because the fabrication technique is relatively easy and their bandgap is geometrically controllable (Gomez et al., 2018) while most of the enhanced properties of graphene are preserved. Furthermore, GNRs enable a quasi-one-dimensional charge carrier confinement (Liu et al., 2009) while preserving enhanced field properties.

Challenges that remain in graphene plasmonics are to develop cleaner fabrication techniques that can produce high-quality graphene ribbons with lower losses, and to push the optical responses to visible and near-infrared range by producing ultranarrow nanoribbons and by doping appropriately (doping type and concentration).

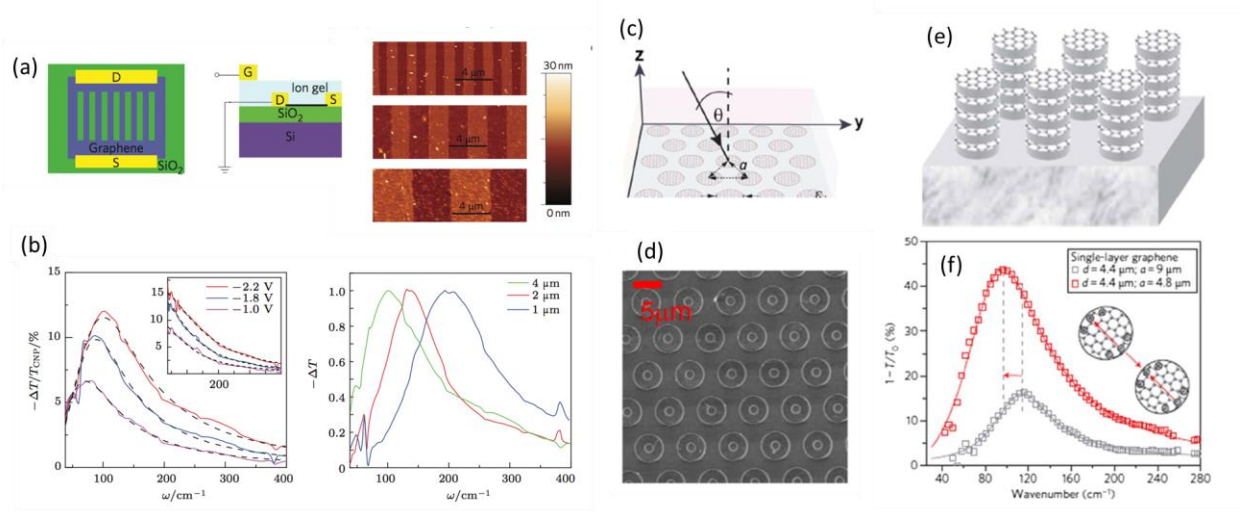

Figure 5.12. Different patterns of graphene nanostructures; (a) top (left) and side (middle) view of graphene micro-ribbon array control of THz resonance of plasmon excitation through electrical gating (reproduced from ref (Ju et al., 2011)); (b) transmission spectra with different micro-ribbon widths of (a); (c) graphene ring array (Yan et al., 2012); (d) doped graphene nanodisks (Thongrattanasiri et al., 2012); (e)–(f) stacked graphene nano disks and their optical responses (Fang et al., 2014) .

5.4 Aligned GNR plasmonics simulation using Drude model.

Fully understanding surface plasmon resonance requires quantum mechanical calculations due to their nanoscale size. When the frequency of the light matches the natural oscillating frequency of the surface electrons, the surface plasmon resonance condition is established. To simplify the simulation and reduce computing cost, we assume the material to be a homogeneous continuum medium, in which the materials' dielectric constant has a complex-valued permittivity when describing the existence and properties of surface plasmons. Using this assumption and combining classical electromagnetic theory by considering electromagnetic wave reflection, transmission, and absorption for GNRs on a silicon dioxide film, i.e., a layered system, we can simulate the surface plasmon resonance can be simulated and the dependence of the surface plasmon resonance on the width of GNRs can be explored.

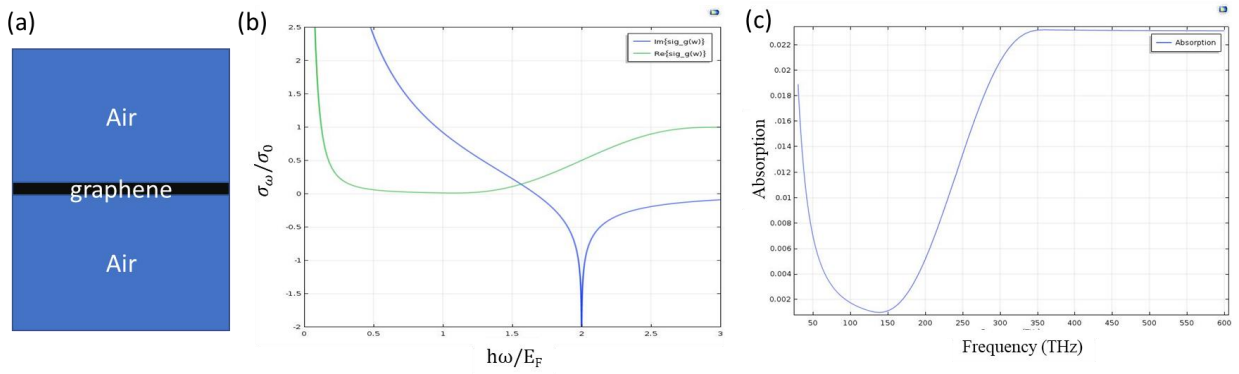

Figure 5.13. (a) Graphene plasmonics structure; (b) real and imaginary parts of the conductivity; (c) optical absorption spectrum of free-standing graphene.

The electromagnetic field distribution, reflectance/transmittance, and eigenmodes were simulated with the 'Electromagnetic Waves Frequency Domain' physics interface of the Wave Optics module in COMSOL. The Wavelength Domain and Boundary Mode Analysis study steps with COMSOL Multiphysics 5.3 was used. A 2D model (shown in Figure 5.13 (a)) was used in our simulation to save computing costs. The 2D simulation region was bounded by periodic ports and Floquet boundaries, and the reflectance and transmittance were calculated from S parameters, as a function of wavelength.

The essential aspect of this simulation is to determine the plasmonic properties of graphene numerically. Graphene is a monolayer with a thickness of about 0.35 nm; compared with the thickness of the silicon dioxide layer (a few hundred nm) and silicon substrate (a few hundred μm), making the numerical treatment of graphene challenging. Two main approaches to address this challenge can be used. The first approach is to treat graphene as a solid or thin film with a small thickness (1 nm was used in this work) and define a permittivity in terms of optical conductivity σ_g, light frequency, and thickness. This approach is effective when the dimensions of other layers are larger than the thickness of graphene. The second approach is to treat graphene as a medium with surface current with optical conductivity σ_g and apply it as a boundary condition to the

interface of two media in which the graphene is placed. This approach is convenient and accurate because most of the properties of graphene are fundamentally determined by its optical conductivity. The optical conductivity of graphene is considered to have two contributions and expressed as $\sigma_g(\omega)=\sigma_{intra}(\omega)+\sigma_{inter}(\omega)$, in which $\sigma_{intra}(\omega)$ represents the intraband transitions. Intraband transitions means the electrons transitions happen within the conduction or valence band where the momentum is not conserved. $\sigma_{inter}(\omega)$ describes interband transitions, which is vertical transitions from the valence band to the conduction band, and the momentum during the transition is conserved. By combining linear response theory, Kubo formula and some approximation, the analytical expressions can be obtained (Falkovsky & Varlamov, 2007; Falkovsky, 2008; Stauber et al., 2008). $\sigma_{intra}(\omega)=\frac{\sigma_0}{\pi}\frac{4E_F}{\hbar\gamma-i\hbar\omega}$ and $\sigma_{inter}(\omega)=\sigma_0\left[\Theta(\hbar\omega-2E_F)+\frac{i}{\pi}\left|\frac{\hbar\omega-2E_F}{\hbar\omega+2E_F}\right|\right]$. Figure 5.13 (b) shows real and imaginary parts of the ratio between the conductivity of a freestanding graphene σ_g and σ_0 and $\sigma_0 = {e^2}/{4\hbar}$. At zero temperature, or if the condition $E_F >> k_BT$ is fulfilled, then the optical conductivity is simplified as $\sigma_g(\omega)=\frac{\sigma_0}{\pi}\frac{4E_F}{\hbar\gamma-i\hbar\omega}$. The transmittance T and reflectance R of single-layer graphene which is related to its conductivity can be expressed as follows (Gonçalves & Peres, 2016; Markos & Soukoulis, 2008):

$$T=\sqrt{\frac{\varepsilon_1}{\varepsilon_2}}\left|\frac{2\sqrt{\varepsilon_2}}{\sqrt{\varepsilon_1}+\sqrt{\varepsilon_2}+\frac{\sigma_g}{c\varepsilon_0}}\right|^2, R=\left|\frac{\sqrt{\varepsilon_2}-\sqrt{\varepsilon_1}+\frac{\sigma_g}{c\varepsilon_0}}{\sqrt{\varepsilon_2}+\sqrt{\varepsilon_1}+\frac{\sigma_g}{c\varepsilon_0}}\right|^2,$$

The absorption of single layer graphene is A=1-R-T. Figure 5.13 (c) shows the optical absorption spectrum of free-standing graphene. The absorption plot has characteristic features such as a Drude peak at terahertz frequencies, a minimal absorption in the mid-infrared range and the universal 2.3% absorption beyond the far-infrared wavelength range. This result agrees with what is reported in literature (Low & Avouris, 2014), meaning our model is rational.

By solving the Maxwell equations for a graphene layer embedded in two dielectric media, the dispersion relations, $\omega(q)$, can be obtained for the graphene surface plasmon, which is $\frac{\varepsilon_1}{\kappa_1(q,\omega)} + \frac{\varepsilon_2}{\kappa_2(q,\omega)} + i\frac{\sigma(\omega)}{\omega\varepsilon_0} = 0$, where ε_1 and ε_2 are the permittivity of the two dielectric media around the graphene. By ignoring the damping factor and solving the dispersion equation, the frequency of the graphene surface plasmons $\omega_g \approx \sqrt{\frac{4\alpha}{\hbar(\varepsilon_1+\varepsilon_2)} E_F c q}$ can be obtained (Maier, 2007), where α is the fine-structure constant and E_F is the Fermi energy (i.e. charge density).

GNR arrays are considered periodic graphene strips with a spatially dependent periodic conductivity. If the width of the graphene nanoribbon is w and the spacing between the ribbons is d, as shown in Figure 5.14 (a), the lattice constant is (d + w) when the conductivity satisfies $\sigma(x) = \sigma(x + d + w)$. To add the geometry parameters of GNRs, the GNR surface plasmons could be simplified as $\omega_{GNR} \approx \sqrt{\frac{4\alpha\pi}{\hbar(\varepsilon_1+\varepsilon_2)} E_F c \frac{m(w+d)-w}{w^2}}$, where m = 1, 2,…. From this equation, we can see that the frequency is determined by the doping level of graphene, the environment, and the geometry parameters of the GNRs. With a smaller width and a smaller spacing of GNR arrays, the resonant wavelength can be pushed from mid-infrared to near-infrared, and even to the visible light range. We first simulate the optical response of free-standing graphene. The structure model shown in Figure 5.13 (a) and Figure 5.13 (b) indicates the real and imaginary parts of the optical conductivity of graphene used in the model based on a calculation using the Drude model. Figure

5.13 (c) shows the optical response of a freestanding graphene layer, which agrees well with the work by (Nair et al., 2008).

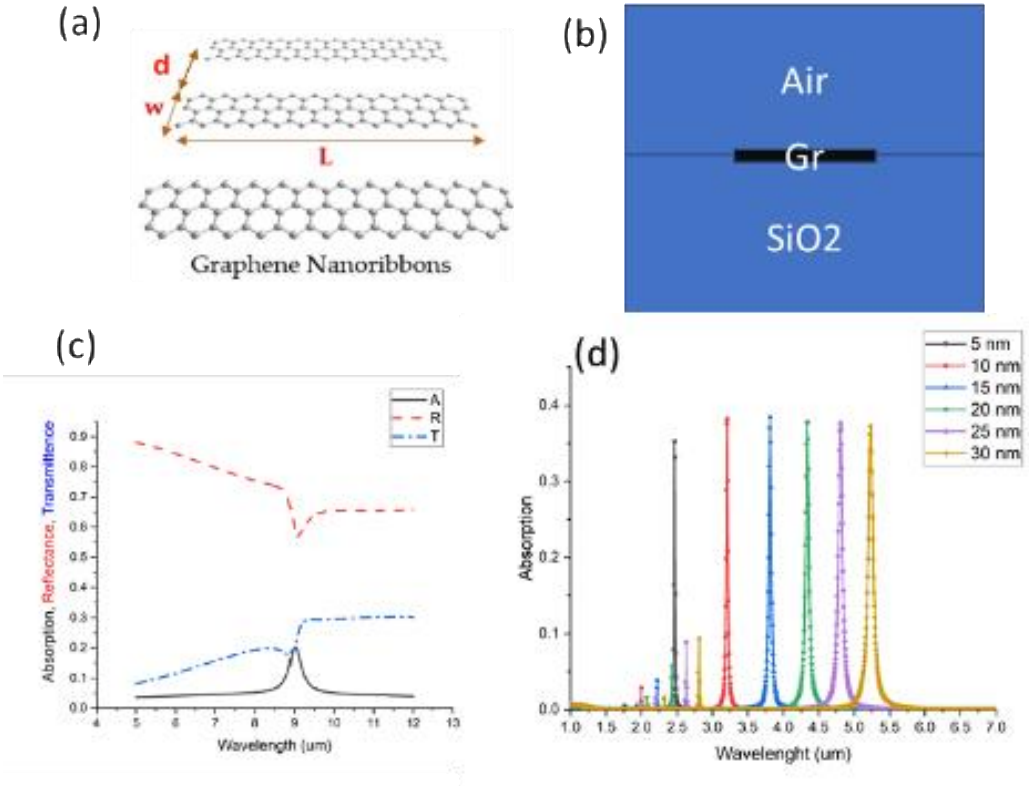

Figure 5.14. (a) Schematic of GNR parameters; (b) layered model used in the simulation; (c) reflectance, transmittance, and absorptance of a GNR array; (d) resonant wavelength of different GNR width with w = d.

We then added the dielectric layer to the model and changed the geometry of the GNRs and added a periodic boundary condition to make the GNR an array. Figure 5.14 (a) shows a schematic of the GNR parameters and Figure 5.14 (b) illustrates the layered model used in the simulation, where a GNR is located on a silicon dioxide film; for comparative purposes, we did not consider the silicon substrate in the simulation. Figure 5.14 (c) shows the reflectance, transmittance, and absorption of a GNR array with a width of 30 nm and a spacing of 10 nm. As shown in the figure, a peak is observed in the absorption that appears at 9 μm. To understand the dependency of the GNR surface plasmon resonant wavelength, we first fixed the relationship

between the spacing and the width of GNR as w = d, where w is the width of GNR, and d is the spacing between two ribbons. We then decreased the width from 30 nm to 5 nm; the simulation results are shown in Figure 5.14 (d). As can be seen in the figure, when the width of GNR becomes smaller, the surface plasmon resonant wavelength gets shifted from the mid-infrared (5.25 μm) to the near-infrared (2.5 μm) range. If we increase the doping level of the GNRs, thereby increasing the Fermi energy, the resonant wavelength may be pushed even further to the visible light range. More work is needed to investigate this hypothesis, including experimental work.

Chapter 6 - Summary and Future Work

6.1 Summary

In summary, this dissertation demonstrates graphene nanoribbons and hybrid ribbons (with nanocrystals) of sub-20 nanometer and sub-10 nanometer ribbon widths by studying ultrafast laser matter interactions using carbon nanotubes as starting materials. The method is highly tunable due to the control of various laser parameters such as intensity and number of pulses exposed, making it possible to discover various nanomaterials in future. Nanoribbons, hybrid nanoribbons and nanocrystals, and related nanoscale carbon materials are of numerous technological importance in electronics, photonics, plasmonics, and sensing devices. The method studied here provides a pathway to create GNRs of sub-10 nanometer width thereby creating tunable bandgap energies in graphene ribbon – a key requirement for graphene-based quantum materials for logic devices for electronics. Since the ribbons are dependent on carbon nanotubes as starting materials and the nanotubes can be grown as small as 1.5 nanometer in diameter, the method described in this dissertation will have the opportunity to synthesize GNRs with sub-2 nanometer width for novel electronics, photonics, and plasmonics applications. Furthermore, the method proposed in this study is scalable, aligns with a wafer scale synthesis, chemical attachment free, and is tunable with only few parameters such as laser power density (intensity) and pulse parameters. The method has potential of unlocking new physics such as LIPT (laser induced phase transition) and LINM (laser induced nanomachining) to design and discover new quantum materials.

CNTs were grown with well-controlled conditions by a collaborator (Bedewy group at University of Pittsburgh, PA). The CNTs were grown at different growth temperatures and catalyst temperatures. Although we have studied the light-matter interaction with one specific growth temperature and catalyst temperature, in future the study could be conducted for various growth

and catalyst temperatures to examine the nanoscale characteristics of the GNRs. TERS was used to characterize the CNTs. However, the TERS study can be extensively studied for tubes grown at different temperatures and the corresponding GNRs. For the first time it was shown that although individual CNTs, grown under very high precision (by our collaborator), yet show "Raman inhomogeneity" in their Raman mapping images when considering the mapping of the tube with respect to their G, D, and 2D bands. Extensive physics-based nanotube and nanoribbon characterization, including interlayer interactions, can be studied using the quality of CNT growth, ultrafast modification, and TERS measurements. Other methods were also applied to characterize individual CNTs to distinguish between them and the GNRs, before and after UFL treatments, respectively. A method to develop nanomachining of the CNTs and turn them into nanoribbons and new phase transformations leading to carbon nanocrystals with ultrafast lasers was shown to constitute an attractive manufacturing method. The transformation from the MWCNTs to GNRs is found to be more sensitive to the overall laser intensity and less sensitive to laser spot size and radiation time. A heat transfer multiphysics model based on the finite element analysis method was used to understand the thermal response under exposure to intense femtosecond pulses. An approach to achieve aligned CNTs with DEP and their chip-scale integration following a hybrid subtractive (photolithography)-additive (micro-plotter printing) manufacturing was well demonstrated. Such a technique will not only align the CNTs, but it can be exploited to fabricate aligned GNRs (or GNR arrays). The hybrid manufacturing developed is a fast, controllable, and low-cost method. Aligned GNR arrays have a number of potential applications such as plasmonic sensors and electronic sensors, to name a few. The tunable GNR widths in the array could provide possibilities in exploring the optical response for near infrared to visible range. A Multiphysics model was developed to study the plasmonic properties of the individual GNR and GNR arrays

based on the finite element analysis method. With smaller GNR width, the surface plasmon resonant wavelength were shown to be tuned in their resonance frequency from the mid-infrared (5.25 μm) to the near-infrared (2.5 μm) range. Visible range resonance frequency could be achieved by using single-wall carbon nanotubes to get ultranarrow GNRs. Further GNR plasmonic study by engineering the doping level of the nanoribbons will further tune the resonance frequency.

6.2 Future work

6.2.1 Fundamental GNR studies

Much of the work could be extended to fundamentally study the laser-matter interactions by applying advanced simulation of ultrafast light pulses to better understand the GNR synthesis. Currently such a model is not available and extensive efforts are needed to achieve this. Second, the nature of nanotubes is very important to understand the GNR synthesized. Tight correlation between CNT growth conditions, ultrafast laser parameter optimization, and the processed GNRs will be key activities to better understand the synthesis. Although in this dissertation work a continuum model was developed using COMSOL Multiphysics heat transfer module to simulate the temperature increase by the ultrafast laser pulses, there is still a lack of understanding of how the carbon nanocrystals were formed (as seen by both TEM and AFM). To better understand the interaction between the incident high-energy photons and the carbon atoms to form new nanostructures, including their defects and edge, an atomistic model of this 1D nanomaterial is needed. Time-dependent density functional theory will be the best method to model the light-matter interaction process to understand the dynamics of this interaction. Also, appropriate thermal coupling factor of electrons and the atoms (G factor) for CNT is still unclear that is needed for accurate thermal property study upon ultrafast light interaction. A relatively easy way to gain this

parameter is to experimentally gain the damage temperature threshold of CNTs by laser and calculate the G factor using the two-temperature model.

6.2.2 CNT Alignments for GNR array

Extensive optimization of the parameters of the DEP process for CNT alignment is needed, including the distances of printed electrodes, the frequency of applied electric field, the density of the CNT solutions, and the type and the vaporization rate of the CNTs solutions. The type of CNTs (diameter, length, purity etc.) could also be critical for highly aligned CNTs and associated GNR array manufacturing. The goal is to be able to control the spacing of the aligned CNTs while achieving a degree of alignment of more than 90%.

6.2.3 Ultra-narrow GNR arrays with Appreciable Bandgap Energies.

Ultra-narrow GNRs are promising for a number of applications such as the CMOS sensors for information processing due to their appreciable bandgap energies. Two approaches are suggested to be conducted to obtain aligned ultra-narrow GNR arrays. The first approach is to treat the aligned CNTs using the ultrafast laser system. Single-walled carbon nanotubes (SWCNT) with a diameter of 1 nm to 2 nm will be needed to achieve such GNR array after precise placement of the tubes following DEP alignment with optimized DEP parameters corresponding to the SWCNTs. New optimal laser unzipping parameters corresponding to SWCNT is needed. The second approach is to utilize the suspended GNRs obtained from the laser unzipping method (post-processed GNRs suspended in DMF) and utilize the DEP method to align them. All the optimized DEP parameters corresponding to the GNRs to align them need to be explored. Single GNR and GNR array plasmonic modeling explained earlier will provide guidelines for devising the validation.

Successful demonstration of the above GNRs and GNR arrays will enable studying both plasmon and electronic properties. Different methods were used to indirectly characterize the surface plasmons, such as the attenuated total reflection (ATR) method, which requires the grating coupling and prism coupling to measure far-field optical absorption/reflection/transmission spectroscopies and electron energy loss spectroscopy (EELS), which uses an electron beam to excite the surface plasmons. More recently, imaging plasmonics has become a very attractive method as it provides a visual representation of the plasmons and practical applications of plasmonics. Scanning Near-field Optical Microscope (SNOM) based near-field excitation has become a popular way to characterize the surface plasmons. SNOM can be used to "see" the propagating path of GNR plasmonics and tip-enhanced Raman spectroscopy can be used to characterize the quality and the edge status of the GNR. FTIR (Fourier Transform Infrared Spectroscopy) measurements may be conducted to verify the optical absorption of the GNR.

Finally, GNR array-based field effect transistor (FET) devices will provide a great platform for using a wide variety of sensors. Because of near-field physics, field enhancement in plasmonic FET sensors will provide a wide range of applications that conventional FET devices will fail to produce. Since GNR transistors are expected to operate at remarkably high frequencies, meaning they can switch at remarkably high speeds approaching the terahertz range, plasmonic based high frequency sensors are proposed to be developed in future.

References

Anderson, N., Hartschuh, A., & Novotny, L. (2007). Chirality changes in carbon nanotubes studied with near-field Raman spectroscopy. *Nano Letters*, *7*(3), 577-582.

Bai, J., Duan, X., & Huang, Y. (2009). Rational fabrication of graphene nanoribbons using a nanowire etch mask. *Nano Letters*, *9*(5), 2083-2087.

Balarastaghi, M., Ahmadi, V., & Darvish, G. (2016). Electro-optical properties of new structure photodetectors based on graphene nanoribbons: an ab initio study. *Journal of the Optical Society of America B*, *33*(11), 2368-2373. https://doi.org/10.1364/JOSAB.33.002368

Balois, M. V., Hayazawa, N., Yasuda, S., Ikeda, K., Yang, B., Kazuma, E., Yokota, Y., Kim, Y., & Tanaka, T. (2019). Visualization of subnanometric phonon modes in a plasmonic nano-cavity via ambient tip-enhanced Raman spectroscopy. *npj 2D Materials and Applications*, *3*(1), 1-10.

Bandow, S., Chen, G., Sumanasekera, G. U., Gupta, R., Yudasaka, M., Iijima, S., & Eklund, P. C. (2002). Diameter-selective resonant Raman scattering in double-wall carbon nanotubes. *Physical Review B*, *66*(7), 075416. https://doi.org/10.1103/PhysRevB.66.075416

Bao, W., Miao, F., Chen, Z., Zhang, H., Jang, W., Dames, C., & Lau, C. N. (2009). Controlled ripple texturing of suspended graphene and ultrathin graphite membranes. *Nature nanotechnology*, *4*(9), 562.

Begtrup, G. E., Ray, K. G., Kessler, B. M., Yuzvinsky, T. D., Garcia, H., & Zettl, A. (2007). Extreme thermal stability of carbon nanotubes. *physica status solidi (b)*, *244*(11), 3960-3963.

Berahman, M., Asad, M., Sanaee, M., & Sheikhi, M. H. (2015). Optical properties of chiral graphene nanoribbons: a first principle study. *Optical and Quantum Electronics*, *47*(10), 3289-3300. https://doi.org/10.1007/s11082-015-0207-1

Bethune, D. S., Klang, C. H., De Vries, M. S., Gorman, G., Savoy, R., Vazquez, J., & Beyers, R. (1993). Cobalt-catalysed growth of carbon nanotubes with single-atomic-layer walls [Article]. *Nature*, *363*(6430), 605-607. https://doi.org/10.1038/363605a0

Bischoff, D., Güttinger, J., Dröscher, S., Ihn, T., Ensslin, K., & Stampfer, C. (2011). Raman spectroscopy on etched graphene nanoribbons. *Journal of Applied Physics*, *109*(7), 073710.

Bissett, M. A., Izumida, W., Saito, R., & Ago, H. (2012). Effect of Domain Boundaries on the Raman Spectra of Mechanically Strained Graphene. *Acs Nano*, *6*(11), 10229-10238. https://doi.org/10.1021/nn304032f

Bludov, Y. V., Ferreira, A., Peres, N. M., & Vasilevskiy, M. I. (2013). A primer on surface plasmon-polaritons in graphene. *International Journal of Modern Physics B*, *27*(10), 1341001.

Cai, J., Wang, C. Y., Yu, T., & Yu, S. (2009). Wall thickness of single-walled carbon nanotubes and its Young's modulus. *Physica Scripta*, *79*(2), 025702. https://doi.org/10.1088/0031-8949/79/02/025702

Cardoso, C., Ferretti, A., & Prezzi, D. (2018). Termini effects on the optical properties of graphene nanoribbons. *The European Physical Journal B*, *91*(11), 286. https://doi.org/10.1140/epjb/e2018-90179-4

Chaunchaiyakul, S., Yano, T., Khoklang, K., Krukowski, P., Akai-Kasaya, M., Saito, A., & Kuwahara, Y. (2016). Nanoscale analysis of multiwalled carbon nanotube by tip-enhanced

Raman spectroscopy. *Carbon*, *99*, 642-648. https://doi.org/https://doi.org/10.1016/j.carbon.2015.12.090

Chen, C., Hayazawa, N., & Kawata, S. (2014). A 1.7 nm resolution chemical analysis of carbon nanotubes by tip-enhanced Raman imaging in the ambient. *Nature Communications*, *5*(1), 1-5.

Chen, P., Wang, X., Luan, Y., Fei, Z., Lacroix, B., Lei, S., & Das, S. R. (2020). High-field electromagnetic radiation converts carbon nanotubes to nanoribbons embedded with carbon nanocrystals. *Journal of Applied Physics*, *128*(2), 024305. https://doi.org/10.1063/5.0012016

Chen, X., Hu, D., Mescall, R., You, G., Basov, D. N., Dai, Q., & Liu, M. (2019). Modern Scattering‐Type Scanning Near‐Field Optical Microscopy for Advanced Material Research. *Advanced Materials*, 1804774.

Chen, X., Saito, T., Yamada, H., & Matsushige, K. (2001). Aligning single-wall carbon nanotubes with an alternating-current electric field. *Applied physics letters*, *78*(23), 3714-3716.

Chichkov, B. N., Momma, C., Nolte, S., von Alvensleben, F., & Tünnermann, A. (1996). Femtosecond, picosecond and nanosecond laser ablation of solids. *Applied Physics A*, *63*(2), 109-115. https://doi.org/10.1007/BF01567637

Childres, I., Jauregui, L. A., Park, W., Cao, H., & Chen, Y. P. (2013). Raman spectroscopy of graphene and related materials. *New developments in photon and materials research*, *1*, 1-20.

Chung, H.-C., Chang, C.-P., Lin, C.-Y., & Lin, M.-F. (2016). Electronic and optical properties of graphene nanoribbons in external fields. *Physical Chemistry Chemical Physics*, *18*(11), 7573-7616.

De Nicola, F., Pintossi, C., Nanni, F., Cacciotti, I., Scarselli, M., Drera, G., Pagliara, S., Sangaletti, L., De Crescenzi, M., & Castrucci, P. (2015). Controlling the thickness of carbon nanotube random network films by the estimation of the absorption coefficient. *Carbon*, *95*, 28-33.

Delhaes, P., Couzi, M., Trinquecoste, M., Dentzer, J., Hamidou, H., & Vix-Guterl, C. (2006). A comparison between Raman spectroscopy and surface characterizations of multiwall carbon nanotubes. *Carbon*, *44*(14), 3005-3013.

Dennis, M. R., Zheludev, N. I., & De Abajo, F. J. G. (2007). The plasmon Talbot effect. *Optics Express*, *15*(15), 9692-9700.

Dimaki, M., & Bøggild, P. (2004). Dielectrophoresis of carbon nanotubes using microelectrodes: a numerical study. *Nanotechnology*, *15*(8), 1095.

Dresselhaus, M. S., & Eklund, P. C. (2000). Phonons in carbon nanotubes. *Advances in Physics*, *49*(6), 705-814. https://doi.org/Doi 10.1080/000187300413184

Elias, D. C., Nair, R. R., Mohiuddin, T., Morozov, S., Blake, P., Halsall, M., Ferrari, A. C., Boukhvalov, D., Katsnelson, M., & Geim, A. (2009). Control of graphene's properties by reversible hydrogenation: evidence for graphane. *Science*, *323*(5914), 610-613.

Ertekin, E., Winkler, M. T., Recht, D., Said, A. J., Aziz, M. J., Buonassisi, T., & Grossman, J. C. (2012). Insulator-to-metal transition in selenium-hyperdoped silicon: observation and origin. *Physical Review Letters*, *108*(2), 026401.

Faggin, F., Hoff, M., & Mazor, S. (1974). Memory system for a multi chip digital computer. In: Google Patents.

Falkovsky, L., & Varlamov, A. (2007). Space-time dispersion of graphene conductivity. *The European Physical Journal B*, *56*, 281-284.

Falkovsky, L. A. (2008). Optical properties of graphene. Journal of Physics: conference series,

Fang, Z., Wang, Y., Schlather, A. E., Liu, Z., Ajayan, P. M., de Abajo, F. J., Nordlander, P., Zhu, X., & Halas, N. J. (2014). Active tunable absorption enhancement with graphene nanodisk arrays. *Nano Letters*, *14*(1), 299-304. https://doi.org/10.1021/nl404042h

Fei, Z., Andreev, G. O., Bao, W., Zhang, L. M., McLeod, A. S., Wang, C., Stewart, M. K., Zhao, Z., Dominguez, G., & Thiemens, M. (2011). Infrared nanoscopy of Dirac plasmons at the graphene–SiO2 interface. *Nano Letters*, *11*(11), 4701-4705.

Ferrari, A. C. (2007). Raman spectroscopy of graphene and graphite: Disorder, electron–phonon coupling, doping and nonadiabatic effects. *Solid State Communications*, *143*(1-2), 47-57.

Feynman, R. P. (1959). Plenty of Room at the Bottom. APS annual meeting,

Geim, A. K., & Novoselov, K. S. (2007). The rise of graphene. *Nature Materials*, *6*(3), 183-191.

Goh, G. L., Agarwala, S., & Yeong, W. Y. (2019). Directed and on‐demand alignment of carbon nanotube: a review toward 3D printing of electronics. *Advanced Materials Interfaces*, *6*(4), 1801318.

Gomez, C. V., Guevara, M., Tene, T., Lechon, L. S., Merino, B., Brito, H., & Bellucci, S. (2018). Energy gap in graphene and silicene nanoribbons: A semiclassical approach. AIP Conference Proceedings,

Gonçalves, P. A. D., & Peres, N. M. (2016). *An introduction to graphene plasmonics*. World Scientific.

González, M. U., Stepanov, A. L., Weeber, J.-C., Hohenau, A., Dereux, A., Quidant, R., & Krenn, J. R. (2007). Analysis of the angular acceptance of surface plasmon Bragg mirrors. *Optics letters*, *32*(18), 2704-2706.

Govindasamy, M., Mani, V., Chen, S.-M., Chen, T.-W., & Sundramoorthy, A. K. (2017). Methyl parathion detection in vegetables and fruits using silver@ graphene nanoribbons nanocomposite modified screen printed electrode. *Scientific reports*, *7*(1), 1-11.

Graf, D., Molitor, F., Ensslin, K., Stampfer, C., Jungen, A., Hierold, C., & Wirtz, L. (2007). Spatially resolved Raman spectroscopy of single-and few-layer graphene. *Nano Letters*, *7*(2), 238-242.

Guo, Z., Zhang, D., & Gong, X.-G. (2009). Thermal conductivity of graphene nanoribbons. *Applied Physics Letters*, *95*(16), 163103.

Han, C., Wang, R., Pan, A., Wang, W., Huang, H., Zhang, J., & Niu, C. (2019). Morphology-directing transformation of carbon nanotubes under the irradiation of pulsed laser with different pulsed duration. *Optics & Laser Technology*, *109*, 27-32.

Han, M. Y., Özyilmaz, B., Zhang, Y., & Kim, P. (2007). Energy band-gap engineering of graphene nanoribbons. *Physical Review Letters*, *98*(20), 206805.

Heeg, S., Shi, L., Poulikakos, L. V., Pichler, T., & Novotny, L. (2018). Carbon Nanotube Chirality Determines Properties of Encapsulated Linear Carbon Chain. *Nano Letters*, *18*(9), 5426-5431. https://doi.org/10.1021/acs.nanolett.8b01681

Her, T.-H., Finlay, R. J., Wu, C., Deliwala, S., & Mazur, E. (1998). Microstructuring of silicon with femtosecond laser pulses. *Applied Physics Letters*, *73*(12), 1673-1675.

Hirschmann, T. C., Araujo, P. T., Muramatsu, H., Zhang, X., Nielsch, K., Kim, Y. A., & Dresselhaus, M. S. (2013). Characterization of Bundled and Individual Triple-Walled Carbon Nanotubes by Resonant Raman Spectroscopy. *Acs Nano*, *7*(3), 2381-2387. https://doi.org/10.1021/nn3055708

Hone, J., Batlogg, B., Benes, Z., Johnson, A., & Fischer, J. (2000). Quantized phonon spectrum of single-wall carbon nanotubes. *Science*, *289*(5485), 1730-1733.

Hu, F., Luan, Y., Fei, Z., Palubski, I. Z., Goldflam, M. D., Dai, S., Wu, J. S., Post, K. W., Janssen, G., & Fogler, M. M. (2017). Imaging the localized plasmon resonance modes in graphene nanoribbons. *Nano Letters*, *17*(9), 5423-5428.

Iijima, S. (2002). Carbon nanotubes: past, present, and future. *Physica B: Condensed Matter*, *323*(1-4), 1-5.

Jablan, M., Buljan, H., & Soljačić, M. (2009). Plasmonics in graphene at infrared frequencies. *Physical Review B*, *80*(24). https://doi.org/10.1103/PhysRevB.80.245435

Jiao, L., Zhang, L., Ding, L., Liu, J., & Dai, H. (2010). Aligned graphene nanoribbons and crossbars from unzipped carbon nanotubes. *Nano Research*, *3*(6), 387-394. https://doi.org/10.1007/s12274-010-1043-z

Jiao, L., Zhang, L., Wang, X., Diankov, G., & Dai, H. (2009). Narrow graphene nanoribbons from carbon nanotubes. *Nature*, *458*(7240), 877-880.

Jones, R. R., Hooper, D. C., Zhang, L., Wolverson, D., & Valev, V. K. (2019). Raman Techniques: Fundamentals and Frontiers. *Nanoscale Research Letters*, *14*(1), 231. https://doi.org/10.1186/s11671-019-3039-2

Journet, C., & Bernier, P. (1998). Production of carbon nanotubes. *Applied physics A: Materials science & processing*, *67*(1).

Journet, C., Maser, W., Bernier, P., Loiseau, A., de La Chapelle, M. L., Lefrant, d. S., Deniard, P., Lee, R., & Fischer, J. (1997). Large-scale production of single-walled carbon nanotubes by the electric-arc technique. *Nature*, *388*(6644), 756-758.

Ju, L., Geng, B., Horng, J., Girit, C., Martin, M., Hao, Z., Bechtel, H. A., Liang, X., Zettl, A., Shen, Y. R., & Wang, F. (2011). Graphene plasmonics for tunable terahertz metamaterials. *Nat Nanotechnol*, *6*(10), 630-634. https://doi.org/10.1038/nnano.2011.146

Kan, Z. (2013). Electrical properties of carbon structures: carbon nanotubes and graphene nanoribbons.

Kato, R., Igarashi, S., Umakoshi, T., & Verma, P. (2020). Tip-Enhanced Raman Spectroscopy of Multiwalled Carbon Nanotubes through D-Band Imaging: Implications for Nanoscale Analysis of Interwall Interactions. *ACS Applied Nano Materials*, *3*(6), 6001-6008. https://doi.org/10.1021/acsanm.0c01188

Kim, P., Shi, L., Majumdar, A., & McEuen, P. L. (2001). Thermal transport measurements of individual multiwalled nanotubes. *Physical Review Letters*, *87*(21), 215502.

Kimouche, A., Ervasti, M. M., Drost, R., Halonen, S., Harju, A., Joensuu, P. M., Sainio, J., & Liljeroth, P. (2015). Ultra-narrow metallic armchair graphene nanoribbons. *Nature Communications*, *6*, 10177.

Klimenko, O., Schuler, S., Muratov, A., Semenenko, V., Gorbachev, E., Mueller, T., & Perebeinos, V. (2021). Tunable graphene plasmons in nanoribbon arrays: the role of interactions. *Optical Materials Express*, *11*(5). https://doi.org/10.1364/ome.421216

Koppens, F. H., Chang, D. E., & García de Abajo, F. J. (2011). Graphene plasmonics: a platform for strong light–matter interactions. *Nano Letters*, *11*(8), 3370-3377.

Kosynkin, D. V., Higginbotham, A. L., Sinitskii, A., Lomeda, J. R., Dimiev, A., Price, B. K., & Tour, J. M. (2009). Longitudinal unzipping of carbon nanotubes to form graphene nanoribbons. *Nature*, *458*(7240), 872-876.

Kumar, P., Panchakarla, L., & Rao, C. (2011). Laser-induced unzipping of carbon nanotubes to yield graphene nanoribbons. *Nanoscale*, *3*(5), 2127-2129.

Kwon, Y.-K., & Kim, P. (2006). Unusually high thermal conductivity in carbon nanotubes. In *High Thermal Conductivity Materials* (pp. 227-265). Springer.

Lee, J., Abdulhafez, M., & Bedewy, M. (2019). Decoupling Catalyst Dewetting, Gas Decomposition, and Surface Reactions in Carbon Nanotube Forest Growth Reveals Dependence of Density on Nucleation Temperature. *The Journal of Physical Chemistry C*, *123*(47), 28726-28738. https://doi.org/10.1021/acs.jpcc.9b07894

Lehman, J. H., Terrones, M., Mansfield, E., Hurst, K. E., & Meunier, V. (2011). Evaluating the characteristics of multiwall carbon nanotubes. *Carbon*, *49*(8), 2581-2602.

Li, X., Wang, X., Zhang, L., Lee, S., & Dai, H. (2008). Chemically derived, ultrasmooth graphene nanoribbon semiconductors. *science*, *319*(5867), 1229-1232.

Liang, G., Neophytou, N., Nikonov, D. E., & Lundstrom, M. S. (2007). Performance projections for ballistic graphene nanoribbon field-effect transistors. *IEEE Transactions on Electron Devices*, *54*(4), 677-682.

Liao, M., Jiang, S., Hu, C., Zhang, R., Kuang, Y., Zhu, J., Zhang, Y., & Dong, Z. (2016). Tip-enhanced Raman spectroscopic imaging of individual carbon nanotubes with subnanometer resolution. *Nano Letters*, *16*(7), 4040-4046.

Lin, M.-F., & Shyu, F.-L. (2000). Optical Properties of Nanographite Ribbons. *Journal of the Physical Society of Japan*, *69*(11), 3529-3532. https://doi.org/10.1143/JPSJ.69.3529

Liu, X., Oostinga, J. B., Morpurgo, A. F., & Vandersypen, L. M. (2009). Electrostatic confinement of electrons in graphene nanoribbons. *Physical Review B*, *80*(12), 121407.

Low, T., & Avouris, P. (2014). Graphene plasmonics for terahertz to mid-infrared applications. *ACS nano*, *8*(2), 1086-1101.

Lu, Q., Keskar, G., Ciocan, R., Rao, R., Mathur, R. B., Rao, A. M., & Larcom, L. L. (2006). Determination of carbon nanotube density by gradient sedimentation. *The Journal of Physical Chemistry B*, *110*(48), 24371-24376.

Ma, P.-C., Siddiqui, N. A., Marom, G., & Kim, J.-K. (2010). Dispersion and functionalization of carbon nanotubes for polymer-based nanocomposites: A review. *Composites Part A: Applied Science and Manufacturing*, *41*(10), 1345-1367.

Maciel, I. O., Anderson, N., Pimenta, M. A., Hartschuh, A., Qian, H., Terrones, M., Terrones, H., Campos-Delgado, J., Rao, A. M., & Novotny, L. (2008). Electron and phonon renormalization near charged defects in carbon nanotubes. *Nature Materials*, *7*(11), 878-883.

Magda, G. Z., Jin, X., Hagymasi, I., Vancso, P., Osvath, Z., Nemes-Incze, P., Hwang, C., Biro, L. P., & Tapaszto, L. (2014). Room-temperature magnetic order on zigzag edges of narrow graphene nanoribbons. *Nature*, *514*(7524), 608-611. https://doi.org/10.1038/nature13831

Mahapatra, S., Li, L., Schultz, J. F., & Jiang, N. (2020). Tip-enhanced Raman spectroscopy: Chemical analysis with nanoscale to angstrom scale resolution. *The Journal of Chemical Physics*, *153*(1), 010902. https://doi.org/10.1063/5.0009766

Maier, S. A. (2007). *Plasmonics: fundamentals and applications* (Vol. 1). Springer.

Malard, L., Pimenta, M. A., Dresselhaus, G., & Dresselhaus, M. (2009). Raman spectroscopy in graphene. *Physics Reports*, *473*(5-6), 51-87.

Malard, L. M., Pimenta, M. A., Dresselhaus, G., & Dresselhaus, M. S. (2009). Raman spectroscopy in graphene. *Physics reports*, *473*(5-6), 51-87.

Malitson, I. H. (1965). Interspecimen comparison of the refractive index of fused silica. *Josa*, *55*(10), 1205-1209.

Markos, P., & Soukoulis, C. M. (2008). Wave propagation. In *Wave Propagation*. Princeton University Press.

Milnera, M., Kurti, J., Hulman, M., & Kuzmany, H. (2000). Periodic resonance excitation and intertube interaction from quasicontinuous distributed helicities in single-wall carbon nanotubes. *Physical Review Letters*, *84*(6), 1324-1327. https://doi.org/DOI 10.1103/PhysRevLett.84.1324

Moore, G. E. (1965). Cramming more components onto integrated circuits. In: McGraw-Hill New York.

Moreno, C., Paradinas, M., Vilas-Varela, M., Panighel, M., Ceballos, G., Peña, D., & Mugarza, A. (2018). On-surface synthesis of superlattice arrays of ultra-long graphene nanoribbons. *Chemical communications*, *54*(68), 9402-9405.

Mubarak, N., Abdullah, E., Jayakumar, N., & Sahu, J. (2014). An overview on methods for the production of carbon nanotubes. *Journal of Industrial and Engineering Chemistry*, *20*(4), 1186-1197.

Myroshnychenko, V., Carbó‐Argibay, E., Pastoriza‐Santos, I., Pérez‐Juste, J., Liz‐Marzán, L. M., & García de Abajo, F. J. (2008). Modeling the optical response of highly faceted metal nanoparticles with a fully 3D boundary element method. *Advanced Materials*, *20*(22), 4288-4293.

Nair, R. R., Blake, P., Grigorenko, A. N., Novoselov, K. S., Booth, T. J., Stauber, T., Peres, N. M., & Geim, A. K. (2008). Fine structure constant defines visual transparency of graphene. *Science*, *320*(5881), 1308. https://doi.org/10.1126/science.1156965

Nakada, K., Fujita, M., Dresselhaus, G., & Dresselhaus, M. S. (1996). Edge state in graphene ribbons: Nanometer size effect and edge shape dependence. *Physical Review B*, *54*(24), 17954.

Nanot, S., Millot, M., Raquet, B., Broto, J.-M., Magrez, A., & Gonzalez, J. (2010). Doping dependence of the G-band Raman spectra of an individual multiwall carbon nanotube. *Physica E: Low-dimensional Systems and Nanostructures*, *42*(9), 2466-2470. https://doi.org/https://doi.org/10.1016/j.physe.2010.06.006

Nguyen, G. D., Tsai, H.-Z., Omrani, A. A., Marangoni, T., Wu, M., Rizzo, D. J., Rodgers, G. F., Cloke, R. R., Durr, R. A., & Sakai, Y. (2017). Atomically precise graphene nanoribbon heterojunctions from a single molecular precursor. *Nature nanotechnology*, *12*(11), 1077-1082.

Novoselov, K. S., Geim, A. K., Morozov, S., Jiang, D., Katsnelson, M. I., Grigorieva, I., Dubonos, S., & Firsov, a. A. A. (2005). Two-dimensional gas of massless Dirac fermions in graphene. *Nature*, *438*(7065), 197-200.

Novoselov, K. S., Geim, A. K., Morozov, S. V., Jiang, D., Katsnelson, M. I., Grigorieva, I., Dubonos, S., & Firsov, a. (2005). Two-dimensional gas of massless Dirac fermions in graphene. *Nature*, *438*(7065), 197-200.

Novoselov, K. S., Geim, A. K., Morozov, S. V., Jiang, D., Zhang, Y., Dubonos, S. V., Grigorieva, I. V., & Firsov, A. A. (2004). Electric Field Effect in Atomically Thin Carbon Films. *Science*, *306*(5696), 666-669. https://doi.org/doi:10.1126/science.1102896

Okuno, Y., Saito, Y., Kawata, S., & Verma, P. (2013). Tip-Enhanced Raman Investigation of Extremely Localized Semiconductor-to-Metal Transition of a Carbon Nanotube. *Physical Review Letters*, *111*(21), 216101. https://doi.org/10.1103/PhysRevLett.111.216101

Oostinga, J. B., Heersche, H. B., Liu, X., Morpurgo, A. F., & Vandersypen, L. M. (2008). Gate-induced insulating state in bilayer graphene devices. *Nature Materials*, *7*(2), 151-157.

Ozden, S., Autreto, P. A., Tiwary, C. S., Khatiwada, S., Machado, L., Galvao, D. S., Vajtai, R., Barrera, E. V., & M. Ajayan, P. (2014). Unzipping carbon nanotubes at high impact. *Nano Letters*, *14*(7), 4131-4137.

Palser, A. H. R. (1999). Interlayer interactions in graphite and carbon nanotubes. *Physical Chemistry Chemical Physics*, *1*(18), 4459-4464.

Paschotta, R. (2008). *Encyclopedia of laser physics and technology* (Vol. 1). Wiley Online Library.

Peng, H. (2008). Aligned carbon nanotube/polymer composite films with robust flexibility, high transparency, and excellent conductivity. *Journal of the American Chemical Society*, *130*(1), 42-43.

Pop, E., Mann, D., Wang, Q., Goodson, K., & Dai, H. (2006). Thermal conductance of an individual single-wall carbon nanotube above room temperature. *Nano Letters*, *6*(1), 96-100.

Pradhan, N. R., Duan, H., Liang, J., & Iannacchione, G. S. (2009). The specific heat and effective thermal conductivity of composites containing single-wall and multi-wall carbon nanotubes. *Nanotechnology*, *20*(24), 245705.

Rafiee, M. A., Lu, W., Thomas, A. V., Zandiatashbar, A., Rafiee, J., Tour, J. M., & Koratkar, N. A. (2010). Graphene nanoribbon composites. *Acs Nano*, *4*(12), 7415-7420.

Rao, A. M., Richter, E., Bandow, S., Chase, B., Eklund, P. C., Williams, K. A., Fang, S., Subbaswamy, K. R., Menon, M., Thess, A., Smalley, R. E., Dresselhaus, G., & Dresselhaus, M. S. (1997). Diameter-selective Raman scattering from vibrational modes in carbon nanotubes. *Science*, *275*(5297), 187-191. https://doi.org/DOI 10.1126/science.275.5297.187

Rao, R., Liptak, D., Cherukuri, T., Yakobson, B. I., & Maruyama, B. (2012). In situ evidence for chirality-dependent growth rates of individual carbon nanotubes. *Nature Materials*, *11*(3), 213-216. https://doi.org/10.1038/nmat3231

Raychaudhuri, S., Dayeh, S. A., Wang, D., & Yu, E. T. (2009). Precise semiconductor nanowire placement through dielectrophoresis. *Nano letters*, *9*(6), 2260-2266.

Ren, W., Saito, R., Gao, L., Zheng, F., Wu, Z., Liu, B., Furukawa, M., Zhao, J., Chen, Z., & Cheng, H.-M. (2010). Edge phonon state of mono-and few-layer graphene nanoribbons observed by surface and interference co-enhanced Raman spectroscopy. *Physical Review B*, *81*(3), 035412.

Rizzo, D. J., Veber, G., Cao, T., Bronner, C., Chen, T., Zhao, F., Rodriguez, H., Louie, S. G., Crommie, M. F., & Fischer, F. R. (2018). Topological band engineering of graphene nanoribbons. *Nature*, *560*(7717), 204.

Rodriguez, R. D., Ma, B., & Sheremet, E. (2019). Raman Spectroscopy Investigation of Laser‐Irradiated Single‐Walled Carbon Nanotube Films. *physica status solidi (b)*, *256*(2), 1800412.

Rousse, A., Rischel, C., Fourmaux, S., Uschmann, I., Sebban, S., Grillon, G., Balcou, P., Förster, E., Geindre, J. P., Audebert, P., Gauthier, J. C., & Hulin, D. (2001). Non-thermal melting in semiconductors measured at femtosecond resolution. *Nature*, *410*(6824), 65-68. https://doi.org/10.1038/35065045

Ruska, E. (1987). The development of the electron microscope and of electron microscopy. *Reviews of Modern Physics*, *59*(3), 627-638. https://doi.org/10.1103/RevModPhys.59.627

Saito, R., Hofmann, M., Dresselhaus, G., Jorio, A., & Dresselhaus, M. S. (2011). Raman spectroscopy of graphene and carbon nanotubes. *Advances in Physics*, *60*(3), 413-550. https://doi.org/10.1080/00018732.2011.582251

Schultz, J. F., Mahapatra, S., Li, L. F., & Jiang, N. (2020). The Expanding Frontiers of Tip-Enhanced Raman Spectroscopy. *Applied Spectroscopy*, *74*(11), 1313-1340. https://doi.org/Artn 0003702820932229

10.1177/0003702820932229

Shinde, D. B., Debgupta, J., Kushwaha, A., Aslam, M., & Pillai, V. K. (2011). Electrochemical unzipping of multi-walled carbon nanotubes for facile synthesis of high-quality graphene nanoribbons. *Journal of the American Chemical Society*, *133*(12), 4168-4171.

Shugaev, M. V., Wu, C., Armbruster, O., Naghilou, A., Brouwer, N., Ivanov, D. S., Derrien, T. J.-Y., Bulgakova, N. M., Kautek, W., & Rethfeld, B. (2016). Fundamentals of ultrafast laser–material interaction. *Mrs Bulletin*, *41*(12), 960-968.

Smith, B., Benes, Z., Luzzi, D., Fischer, J., Walters, D., Casavant, M., Schmidt, J., & Smalley, R. (2000). Structural anisotropy of magnetically aligned single wall carbon nanotube films. *Applied Physics Letters*, *77*(5), 663-665.

Son, Y.-W., Cohen, M. L., & Louie, S. G. (2006). Energy gaps in graphene nanoribbons. *Physical review letters*, *97*(21), 216803.

Stauber, T., Peres, N., & Geim, A. (2008). Optical conductivity of graphene in the visible region of the spectrum. *Physical Review B*, *78*(8), 085432.

Stöckle, R. M., Suh, Y. D., Deckert, V., & Zenobi, R. (2000). Nanoscale chemical analysis by tip-enhanced Raman spectroscopy. *Chemical Physics Letters*, *318*(1), 131-136. https://doi.org/https://doi.org/10.1016/S0009-2614(99)01451-7

Streltsov, A. M., & Borrelli, N. F. (2002). Study of femtosecond-laser-written waveguides in glasses. *Journal of the Optical Society of America B*, *19*(10), 2496-2504. https://doi.org/10.1364/JOSAB.19.002496

Sun, L., Gong, J., Zhu, D., Zhu, Z., & He, S. (2004). Diamond nanorods from carbon nanotubes. *Advanced Materials*, *16*(20), 1849-1853.

Talirz, L., Söde, H., Cai, J., Ruffieux, P., Blankenburg, S., Jafaar, R., Berger, R., Feng, X., Müllen, K., & Passerone, D. (2013). Termini of bottom-up fabricated graphene nanoribbons. *Journal of the American Chemical Society*, *135*(6), 2060-2063.

Thongrattanasiri, S., Koppens, F. H., & Garcia de Abajo, F. J. (2012). Complete optical absorption in periodically patterned graphene. *Physical Review Letters*, *108*(4), 047401. https://doi.org/10.1103/PhysRevLett.108.047401

Thornton, J. (2000). Scanning Probe Microscopy Training Notebook. *Santa Barbra, Ca: Veeco Metrology Group*, 1-56.

Toropov, A. A., & Shubina, T. V. (2015). *Plasmonic effects in metal-semiconductor nanostructures* (Vol. 19). OUP Oxford.

Villalpando-Paez, F., Son, H., Nezich, D., Hsieh, Y. P., Kong, J., Kim, Y., Shimamoto, D., Muramatsu, H., Hayashi, T., & Endo, M. (2008). Raman spectroscopy study of isolated double-walled carbon nanotubes with different metallic and semiconducting configurations. *Nano Letters*, *8*(11), 3879-3886.

Vorobyev, A. Y., & Guo, C. (2013). Direct femtosecond laser surface nano/microstructuring and its applications. *Laser & Photonics Reviews*, *7*(3), 385-407.

Wakabayashi, K., Fujita, M., Ajiki, H., & Sigrist, M. (1999). Electronic and magnetic properties of nanographite ribbons. *Physical Review B*, *59*(12), 8271.

Wang, D., Song, P., Liu, C., Wu, W., & Fan, S. (2008). Highly oriented carbon nanotube papers made of aligned carbon nanotubes. *Nanotechnology*, *19*(7), 075609.

Wang, X., & Dai, H. (2010). Etching and narrowing of graphene from the edges. *Nature chemistry*, *2*(8), 661-665.
Wang, X., Yu, X., Berg, M., DePaola, B., Shi, H., Chen, P., Xue, L., Chang, X., & Lei, S. (2020). Nanosecond laser writing of straight and curved waveguides in silicon with shaped beams. *Journal of Laser Applications*, *32*(2), 022002. https://doi.org/10.2351/1.5139973
Wei, B., Zhang, J., Liang, J., & Wu, D. (1998). The mechanism of phase transformation from carbon nanotube to diamond. *Carbon*, *36*(7-8), 997-1001.
Wu, C., Crouch, C., Zhao, L., Carey, J., Younkin, R., Levinson, J., Mazur, E., Farrell, R., Gothoskar, P., & Karger, A. (2001). Near-unity below-band-gap absorption by microstructured silicon. *Applied Physics Letters*, *78*(13), 1850-1852.
Wu, Z.-S., Ren, W., Gao, L., Liu, B., Zhao, J., & Cheng, H.-M. (2010). Efficient synthesis of graphene nanoribbons sonochemically cut from graphene sheets. *Nano Research*, *3*(1), 16-22.
Xiao, J., Ouyang, G., Liu, P., Wang, C., & Yang, G. (2014). Reversible nanodiamond-carbon onion phase transformations. *Nano Letters*, *14*(6), 3645-3652.
Xiao, L., Zhang, Y., Wang, Y., Liu, K., Wang, Z., Li, T., Jiang, Z., Shi, J., Liu, L., & Li, Q. (2010). A polarized infrared thermal detector made from super-aligned multiwalled carbon nanotube films. *Nanotechnology*, *22*(2), 025502.
Xu, W., & Lee, T.-W. (2016). Recent progress in fabrication techniques of graphene nanoribbons. *Materials Horizons*, *3*(3), 186-207.
Yan, H., Low, T., Zhu, W., Wu, Y., Freitag, M., Li, X., Guinea, F., Avouris, P., & Xia, F. (2013). Damping pathways of mid-infrared plasmons in graphene nanostructures. *Nature Photonics*, *7*(5), 394-399. https://doi.org/10.1038/nphoton.2013.57
Yan, H., Xia, F., Li, Z., & Avouris, P. (2012). Plasmonics of coupled graphene micro-structures. *New Journal of Physics*, *14*(12), 125001.
Yano, T.-a., Ichimura, T., Kuwahara, S., H'Dhili, F., Uetsuki, K., Okuno, Y., Verma, P., & Kawata, S. (2013). Tip-enhanced nano-Raman analytical imaging of locally induced strain distribution in carbon nanotubes. *Nature Communications*, *4*(1), 2592. https://doi.org/10.1038/ncomms3592
Yano, T.-a., Verma, P., Saito, Y., Ichimura, T., & Kawata, S. (2009). Pressure-assisted tip-enhanced Raman imaging at a resolution of a few nanometres. *Nature Photonics*, *3*(8), 473-477. https://doi.org/10.1038/nphoton.2009.74
Zdrojek, M., Judek, J., & Wasik, M. (2012). Laser heating control with polarized light in isolated multiwalled carbon nanotubes. *Physical Review Letters*, *108*(22), 225501.
Zhang, G., Qi, P., Wang, X., Lu, Y., Li, X., Tu, R., Bangsaruntip, S., Mann, D., Zhang, L., & Dai, H. (2006). Selective etching of metallic carbon nanotubes by gas-phase reaction. *Science*, *314*(5801), 974-977.
Zhang, K., Stocks, G. M., & Zhong, J. (2007). Melting and premelting of carbon nanotubes. *Nanotechnology*, *18*(28), 285703.
Zhang, Y., Tan, Y.-W., Stormer, H. L., & Kim, P. (2005). Experimental observation of the quantum Hall effect and Berry's phase in graphene. *Nature*, *438*(7065), 201-204.
Zhang, Y., Tang, T.-T., Girit, C., Hao, Z., Martin, M. C., Zettl, A., Crommie, M. F., Shen, Y. R., & Wang, F. (2009). Direct observation of a widely tunable bandgap in bilayer graphene. *Nature*, *459*(7248), 820-823.
Zhang, Y., Yang, B., Ghafoor, A., Zhang, Y., Zhang, Y.-F., Wang, R.-P., Yang, J.-L., Luo, Y., Dong, Z.-C., & Hou, J. G. (2019). Visually constructing the chemical structure of a single

molecule by scanning Raman picoscopy. *National Science Review*, *6*(6), 1169-1175. https://doi.org/10.1093/nsr/nwz180

Zhu, G., Yi, Y., Liu, Z., Lee, H. J., & Chen, J. (2016). Highly sensitive electrochemical sensing based on 2-hydroxypropyl-β-cyclodextrin-functionalized graphene nanoribbons. *Electrochemistry Communications*, *66*, 10-15.

Appendix A - Publications

Publications

1. Pingping Chen, et al. High-field electromagnetic radiation converts carbon nanotubes to nanoribbons embedded with carbon nanocrystals Journal of Applied Physics, 128, 024305 (2020)
2. Xinya Wang, Pingping Chen, et al. Curved waveguides in silicon written by a shaped laser beam. Optics Express, 29.10, 14201-14207 (2021)
3. Anand P S Gaur, Pingping Chen, et al. Graphene Aerosol Gel Ink for Printing Micro-Supercapacitors. ACS Applied Energy Materialsˇa, 4, 8, 76327641 (2021)
4. Xue, Lianjie, Song Liu, Yang Hang, Adam M. Summers, Derrek J.Wilson, XinyaWang, Pingping Chen, Thomas G. Folland et al. "Unraveling Ultrafast Photoionization in Hexagonal Boron Nitride." arXiv:2101.10429 (2021).
5. Xinya Wang, Pingping Chen, et al. Nanosecond laser writing of straight and curved waveguides in silicon with shaped beams. Journal of Laser Application, 32, 022002 (2020)
6. Pingping Chen, Ju Liu, Li Wang, Kuijuan Jin, Yan Yin, and Zhiyuan Li. Optimization and maximum potential of optical antennae in near-field enhancement. Appl. Opt, 54, 5822-5828 (2015).
7. Tong Ye, Pingping Chen, Ju Liu, Lin Gan, Yan Yin. Gold nanorods based surface-enhanced Raman scattering substrates prepared by polycarbonate membranes, in Proceedings of 17th National Conference on Light Scattering, Xi'an, China, October 2013.

Conference and presentations

Tip-enhanced Raman spectroscopy of chemical vapor deposited multi-wall carbon nanotubes, 7th Nano Today, Online and on-demand, November 2021.

Nanoscale Manipulation of Carbon Nanotube Structure with Light-Matter Interaction. Oral presentation. Materials Research Society Fall Conference, Boston, USA, December 2019.

NANOSCALE MANIPULATION OF CARBON NANOTUBE STRUCTURE WITH ULTRAFAST LIGHT-MATTER INTERACTION. Poster presentation. Research and State, Kansas State University, Oct 2019